

Deliverable 3 (D3): Report on the development of three traceable channel sounding testbeds for wide-bandwidth radio propagation channel measurements up to 750 GHz in complex real-world scenarios



Organisation name of the lead participant for the deliverable:

Queen Mary University London

Authors:

Qamar Muhammad, Lawrence Carslake, Ivan Bonev, Ben Chen, Fengchun Zhang, Ke Guan, Tian Hong Loh, Akram Alomainy

Due date of the deliverable: 30 June 2025

Actual submission date of the deliverable: 25 June 2025

Confidentiality Status: PU - Public, fully open (remember to deposit public deliverables in a trusted repository).

Funded by the European Union. Views and opinions expressed are however those of the author(s) only and do not necessarily reflect those of the European Union or EURAMET. Neither the European Union nor the granting authority can be held responsible for them.

Deliverable Cover Sheet

The project has received funding from the European Partnership on Metrology, co-financed from the European Union's Horizon Europe Research and Innovation Programme and by the Participating States.

Metrology for Emerging Wireless Standards (MEWS)

Deliverable D3

Abbreviations (Part 1)

Acronym	Description
AB	Alpha-Beta model
ABG	Alpha-Beta-Gamma model
AiP	Antenna-in-Package
AoA	Angles of Arrival
AoD	Angles of Departure
ADC	Analog-to-Digital Converter
BS	Base Station
BW	BandWidth
B5G	Beyond 5G
CATR	Compact Antenna Test Range
CDF	Cumulative Distribution Function
CE	Channel Emulator
CFR	Channel Frequency Response
CIR	Channel Impulse Response
DAC	Digital-to-Analog Converter
DFT	Discrete Fourier Transform
DDSS	Double-Directional Scanning Sounding scheme
Dir-VAA	Directional Antenna-Based VAA
DP	Digital Pre-distortion process
DSS	Directional Scanning Sounding
E/O	Electrical-to-Optical unit
EVM	Error Vector Magnitude
FIBF	Frequency-Invariant Beam-Forming
FIR	Finite Impulse Response
FSPL	Free-Space Path Loss
HF	High Frequency
HPBW	Half Power Beamwidth
IF	Intermediate Frequency
IFBW	Intermediate Frequency Bandwidth
LNA	Low Noise Amplifier
LO	Local Oscillator
LoS	Line of Sight
LTE	Long Term Evolution

Abbreviations (Part 2)

Acronym	Description
MIMO	Multiple-input-multiple-output
mmWave	Millimeter Wave frequency band
MCBF	Modified Classical Beamforming Algorithm
MMSE	Minimum Mean Square Error
MPC	Multi-Path Components
NF	Near-Field
NLOS	Non-Line of Sight
NR	New Radio
NRMSE	Normalized Root-Mean-Square Error
Omni-VAA	Omnidirectional Antenna-Based VAA
O/E	Optical-to-Electrical unit
OTA	Over the Air Testing
PADP	Power Angle Delay Profile
PAS	Power Angular Spectrum
PDP	Power Delay Profile
PDSCH	Physical Downlink Shared Channel
PL	Path Loss
RT	Ray Tracing
RF	Radio Frequency
RF1	Radio Frequency 1 band covers (410-7125) MHz
RF2	Radio Frequency 2 band covers (24.25-52.6) GHz
RF3	Radio Frequency 3 band covers (7.125-24.25) GHz
RoF	Radio-over-Fiber
Rx	Receiver
SIC	Successive Interference Cancellation
SISO	Single-Input Single-Output
SNR	Signal to Noise Ratio
SGH	Standard Gain Horn
Sub-THz	Sub-Terahertz band
Tx	Transmitter
UCA	Uniform Circular Array
UWB	Ultra-WideBand

Abbreviations (Part 3)

Acronym	Description
VAA	Virtual Antenna Array
VDT	Virtual Drive Test
VSA	Vector Signal Analyzers
VNA	Vector Network Analyzer
WP	Work Package
3GPP	Third Generation Partnership Project
4G	4th Generation Wireless Systems
5G	5th Generation Wireless Systems
6G	6th Generation Wireless Systems

Contents

Metrology for Emerging Wireless Standards (MEWS)	1
Deliverable D3	1
Abbreviations (Part 1)	1
Executive summary	4
1. Introduction	5
2. Novel channel sounder design at sub-THz band. Channel measurement in various scenarios	6
2.1 Novel channel sounder designs at sub-THz band	6
2.2 Channel measurements with Omni-VAA, Dir-VAA and DSS schemes at 100 GHz and at 300 GHz in various deployment scenarios	21
2.3 Double DSS measurements for channel characterization in a large hall scenario at 300 GHz	51
2.4 Channel measurements between 330 and 500 GHz for indoor and corridor scenerios	57
2.5 Channel measurements between 500 and 750 GHz for indoor, corridor and outdoor scenarios	61
3. Development of band-stitching algorithm. mmWave 8 × 8 Antenna-in-Package (AiP) Array Platform - experimental validation and applications	73
3.1 Development of band-stitching algorithm	73
3.2 Experimental Validation and Applications of mmWave 8 × 8 AiP Array Platform	91
4. Terahertz (THz) Channel Modeling in 6G Deployment Scenarios via Ray Tracing (RT)	100
4.1 Introduction	100
4.2 Channel characteristics of THz communications systems	100
4.3 Measurement-calibrated ray tracing	101
4.3.1 Ray tracing validation for 330 to 500 GHz	106
4.5 Ray tracing validation for 500 to 750 GHz	107
4.6 Conclusion	110
5. Conclusion	113
6. Appendix	116

Executive summary

This report is the second deliverable D3 of the Metrology for Emerging Wireless Standards (MEWS) project, covering topics included in Work Package 2 (WP2) and it merges the knowledge of the newly developed channel sounder designs at Sub-Terahertz (sub-THz), conducted sub-THz channel measurements (by using a virtual antenna array made up by Omnidirectional antennas (Omni-VAA), a virtual antenna array composed of Directional antennas (Dir-VAA) schemes and Directional Scanning Sounding (DSS) scheme) in various scenarios (entrance, corridor, big hall), double DSS (DDSS) sub-THz measurements in a hall scenario, antenna in package (AiP) based channel sounder for dynamic scenarios, development of a band-stitching algorithm and performed ray-tracing (RT) simulations at sub-THz band.

The deliverable is organized as follows: Chapter I is the introduction part, while Chapter II contains three main topics from WP2, i.e. an improved channel sounder designs developed for 100 GHz and 300 GHz, channel measurements with Omni-VAA, Dir-VAA and DSS schemes at 100 GHz and at 300 GHz in different scenarios and DSSS channel measurements at 300 GHz. Chapter III describes a development of a band-stitching algorithm and an AiP based channel sounder for dynamic scenarios. RT simulation results at sub-THz are presented and discussed in Chapter IV. Conclusions are drawn in Section V. Finally, the most common equations related to estimation of channel parameters and characteristics are included in an Appendix.

1. Introduction

This deliverable document aims to present the achievements and contributions obtained within the channel sounder design, channel measurements and RT modeling for sub-THz band. It encompasses detailed measurements and modeling efforts across various relevant propagation scenarios, offering insights into the channel parameters and characteristics.

The main objectives of the deliverable can be summarized as follows:

- Development of time-domain channel sounder design for 100 and 300 GHz. A Radio over Fiber (RoF) scheme is proposed to extend the measurement distance. A phase compensation scheme is further implemented to support the Virtual Antenna Array (VAA) channel measurements.
- Extension of the phase compensated radio over fiber technique for channel sounding systems operating between 300-500 GHz and 500-750 GHz. Additionally their implementation on different Vector Network Analyzer (VNA), RoF, and extender head manufacturers has been considered.
- Channel measurements (by using Omni-VAA, Dir-VAA and DSS schemes) have been conducted at 100 GHz and at 300 GHz in various scenario (entrance, corridor, big hall). The results have been presented and discussed.
- Channel measurements have been conducted between 300-500 GHz and 500-750 GHz for various scenarios (indoor, corridor, outdoor) for distances up to 100 meters. The results have been presented and discussed.
- Channel measurements by using DDSS scheme have been conducted at 300 GHz and the results have been presented and discussed.
- Development of band-stitching algorithm
- Development of an AiP based channel sounder for dynamic scenarios.
- RT simulations results at sub-THz have been presented and discussed.

2. Novel channel sounder design at sub-THz band. Channel measurement in various scenarios

2.1 Novel channel sounder designs at sub-THz band

2.1.1 Channel sounder structure, link budget and system calibration The presented work in this subchapter is based on [1] and [2]. Two channel sounder systems based on VNA, operating respectively at frequencies between 75 and 110 GHz and 220-330 GHz, are proposed and discussed. For both designs, the channel sounder structure, link budget and system calibration are studied. In the case of the channel sounder at 220-330 GHz, RoF technique and a novel phase compensation scheme to stabilize the phase variations have been implemented, enabling long-range phase-coherent measurements. The schematic diagrams of the the VNA based channel sounders are shown in Figure 1.

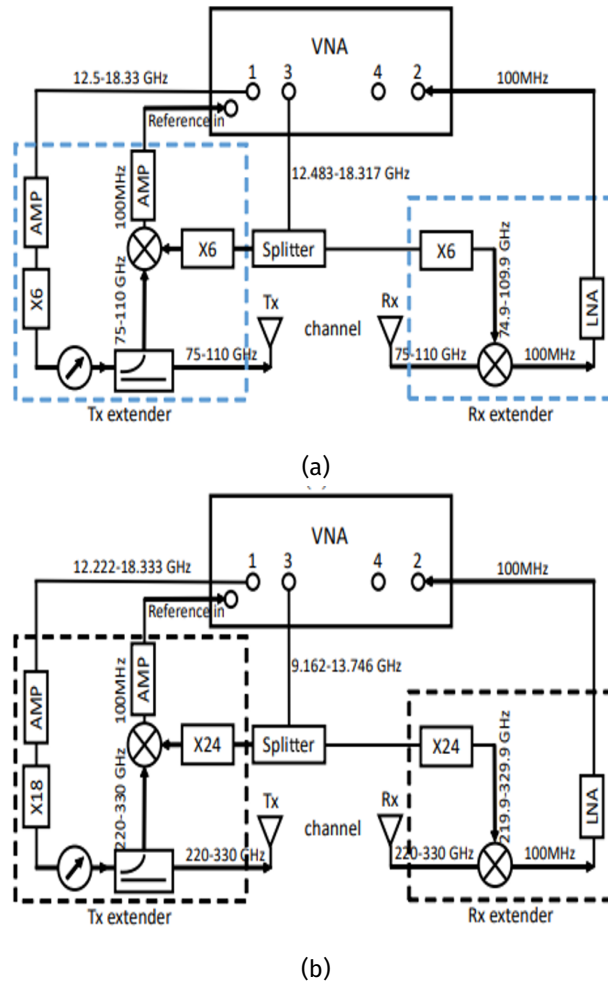


Figure 1: The schematic diagram the VNA based channel sounder. (a) 75-110 GHz; (b) 220-330 GHz

As illustrated in Figure 1a, the transmitter (Tx) side of the 100 GHz channel sounder sends signals from 12.50 to 18.33 GHz from port 1, which, after going through a six-times multiplier, produce sub-THz signals from 75 to 110 GHz. A coupler splits the signals into two signals, one of which is used to provide 100 MHz reference signals and the other to transmit through a horn antenna. Keep in mind that LO signals from 12.48 to 18.32 GHz are sent by port 3. After passing via a signal splitter, the LO signals are multiplied six times to reach the frequency range of 74.9 to 109.9

GHz. The received signal is demodulated to 100 MHz, amplified by an low noise amplifier (LNA), and transmitted to port 2 at the receiver (Rx) end. The result of dividing the received signal at 100 MHz by the reference signal is used to estimate the S_{21} parameter. The sounding structure of a channel sounder operating in the 220-330 GHz frequency range is comparable to that of a sounder operating in the 75-110 GHz frequency range. The primary distinction is that the multiplier coefficients are 24 for the LO side and 18 for the Radio Frequency (RF) side. The link budget analysis at 92.5 GHz and 275 GHz is presented in Figure 2.

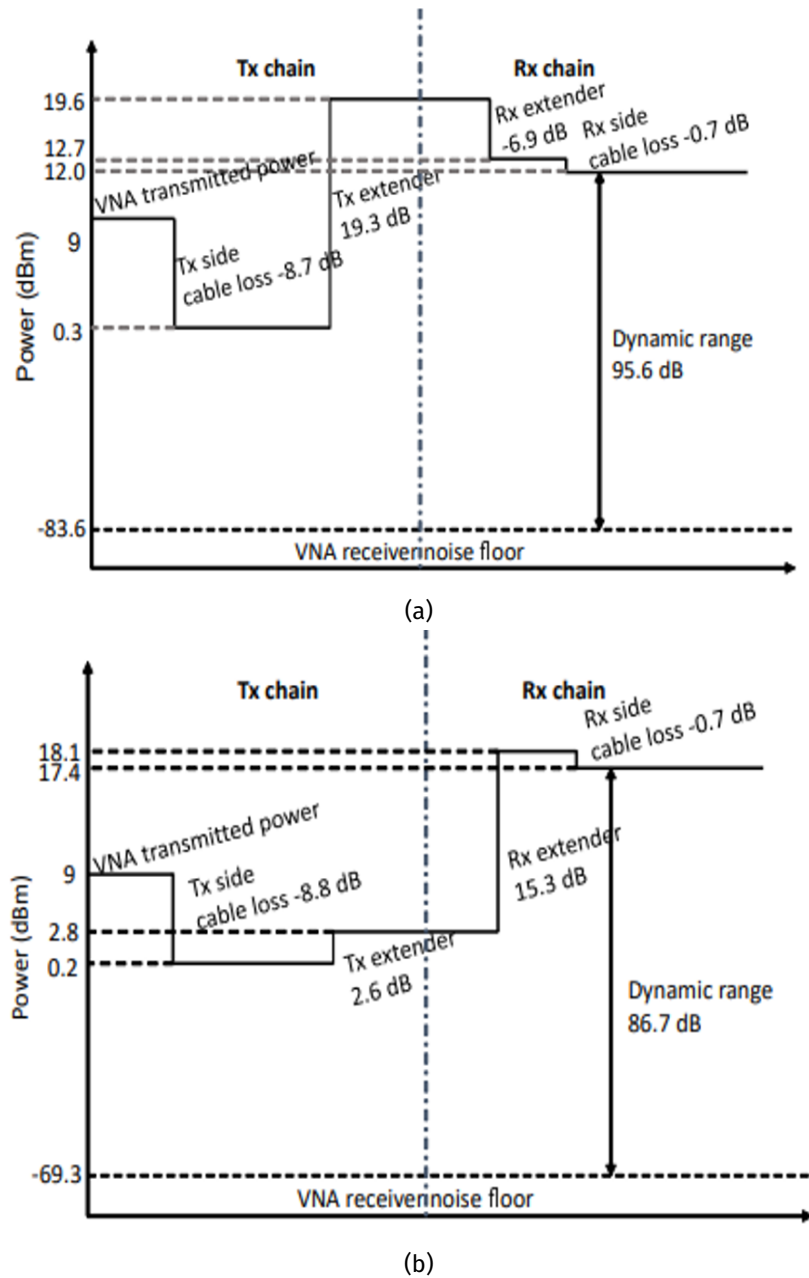


Figure 2: The link budget of the VNA based channel sounder a) 100 GHz channel sounder at 92.5 GHz b) 300 GHz channel sounder at 275 GHz

The VNA was connected to the extenders at the Tx and Rx sides by using 5 m RF cables. The antennas are not

accounted for in the provided link budget study. To make sure the Tx extender functions properly and to prevent damage, the transmitted power from port 1 for both channel sounders is 9 dBm. The 100 GHz channel sounder has a dynamic range of 95.6 dB, which is 8.9 dB greater than the 300 GHz channel sounder's. Because of the 100 MHz received signal, the RF cable loss is incredibly low at the Rx side as opposed to the high loss at the Tx side. Due to cable limitations, these two channel sounders can provide channel measurements at distances less than 10 meters. By lengthening the RF cable at the Rx side, the measurement range can be expanded.

Channel measurements require calibration. In order to de-embed the system response in the back-to-back measurement, a normalization procedure is typically performed prior to the channel measurement. Verifying the efficiency of the absorbers positioned around the antennas is the aim of our measurement. To calibrate the system response, a normalization procedure and a back-to-back measurement (without the antennas) were carried out first. Then, using antennas, comparative channel measurements were made at a distance of 0.4 m with and without absorbers, as indicated in Figure 3. More information about the measurement setup is presented in Table I.



Figure 3: The photos of the channel measurement setup: a) Without absorber; b) With absorber

The use of the absorbers can significantly reduce the spurious peaks, as shown in Figure 4a of the comparison of the channel impulse response (CIR) at 100 GHz. However, the red area showed a few weak unexpected spurious peaks.

The large bandwidth and the non-optimal absorbers for the 300 GHz band may be the reason why the calibration result with absorbers of the 300 GHz channel sounder is worse than that of the 100 GHz channel sounder. By selecting the proper bandwidth for the measurements and the calibration progress method in the post-processing, those small spurious peaks can be removed.

TABLE I
THE CONFIGURATION OF CALIBRATION INVESTIGATION AND DIRECTIONAL CHANNEL MEASUREMENTS

	Value	Value
Parameter	100 GHz system	300 GHz system
VNA Transmitted power [dBm]	9	9
Antenna type	Horn	Horn
Antenna gain [dBi]	21	25
Half-power beamwidth [°]	19	8
Calibration investigation		
Start frequency [GHz]	75	220
End frequency [GHz]	110	330
Bandwidth [GHz]	35	110
Frequency point	10001	10001
Tx-Rx distance [m]	0.4	0.4
Antenna height [m]	0.9	0.9
Directional measurement		
Start frequency [GHz]	90	250
End frequency [GHz]	110	300
Bandwidth [GHz]	20	50
Frequency point	6001	15001
Tx-Rx distance [m]	2.25	
Antenna height [m]	0.9	
Rx azimuth range [°]	[-180, 179]	
Rx rotating step [°]	1	

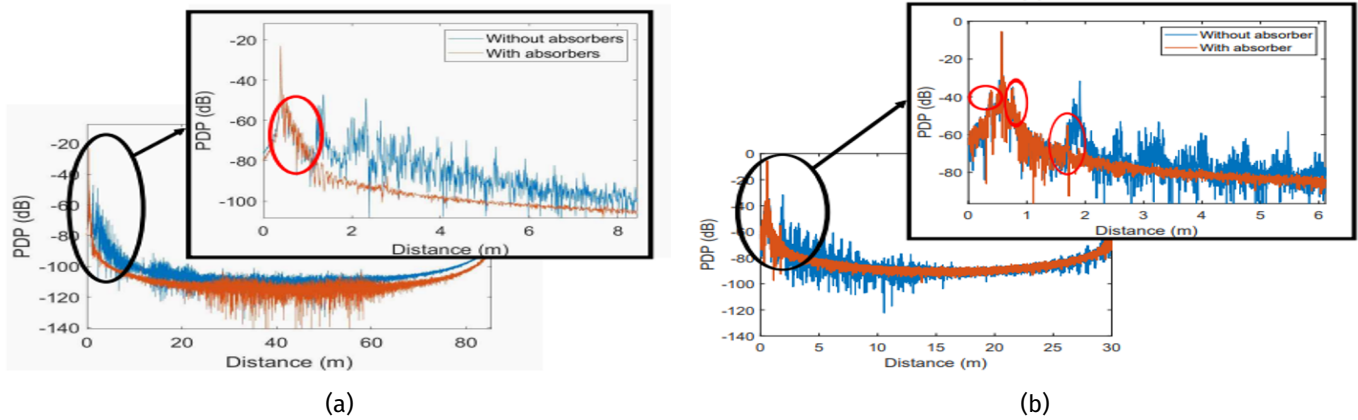


Figure 4: The comparison of the CIRs with and without absorbers at the distance of 0.4 m: a) 100 GHz channel sounder b) 300 GHz channel sounder

2.1.2 Radio-over-fiber technique and a novel phase compensation scheme This subsection is based on the work in [2] and propose the first implementation of 220-330 GHz phase-compensated long-range VNA-based channel sounder. In the suggested channel sounder, two three-port optical circulators are used to create bidirectional signal transfer (i.e. forward and feedback link) on the same optical fiber cable. Thus, the information from the feedback link is used to correct the impairments introduced by the thermal changes or the mechanical stress of the cable.

2.1.2.1 Channel sounder structure Figure 5 shows the block diagram of the proposed sub-THz channel sounder.

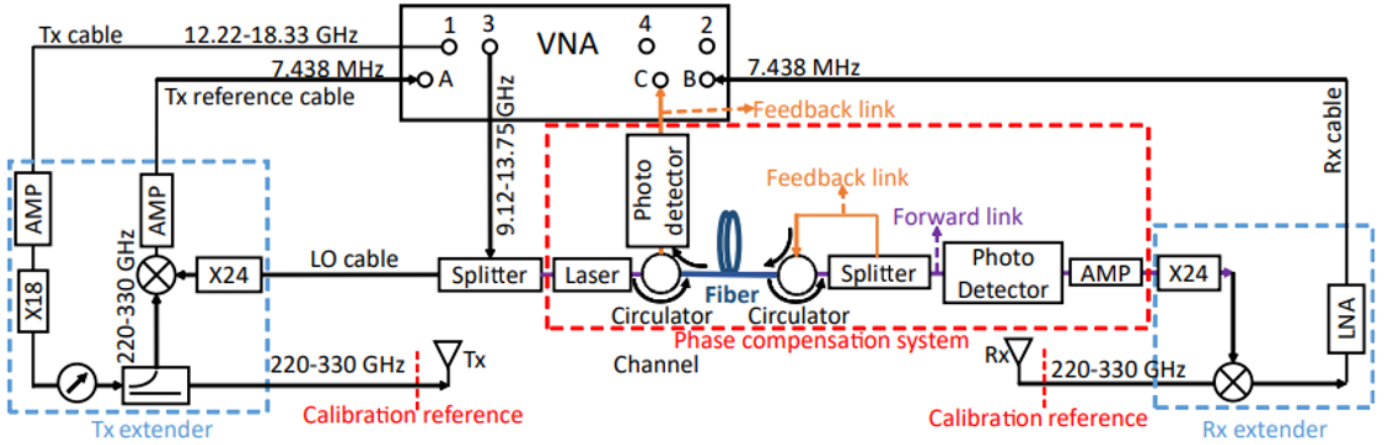


Figure 5: Block diagram of the proposed RoF VNA-based sub-THz channel sounder

The components of the channel sounder components are presented in Table II.

TABLE II
COMPONENTS OF THE CHANNEL SOUNDER

Part	Name	Frequency/Wavelength
VNA	Keysight PNA N5227B	10MHz – 67GHz
Extender	VDI WR 3.4	220GHz – 330GHz
Laser	QMOD XMTQ-C-A-24	1550 nm
Photo detector	QMOD XMRQ-C-A-24	1550 nm
Optical splitter	JDS FFC-CKH12B105-003	1550 nm
Optical circulator	OZ FOC-12N-111-9/125-SSS	1550 nm
RF amplifier	Picosecond 5828-108	9GHz – 14GHz

As outlined in Figure 5, the channel sounder can be divided into two main parts, i.e., sub- THz channel sounder and phase compensation system.

1) Sub-THz channel sounder: Signals with a frequency band 12.22-18.33 GHz are sent from Port 1, multiplied by 18 times to a signal with a frequency band of 220-330 GHz, and then divided into two signals. One of the split signals is transmitted via a directional antenna and the other one is used to generate a reference signal with a frequency of 7.438 MHz. The local oscillator (LO) signal with a frequency band of 9.12-13.75 GHz is sent by Port 3 and split into two signals. The split LO signal is then multiplied by a 24 times multiplier. At the Rx side, the received signal is demodulated to a signal with frequency of 7.438 MHz, then it is amplified by a LNA and sent to Port B.

By bending the cable in a circle of a 30 cm diameter, the effect of the mechanical stress on the phase of the sounder was tested by conducting measurements. Prior to each cable bending, calibration was performed. The objective was to examine the phase change introduced by the cable effect in the entire system. It was found that the main phase change is caused by the mechanical stress on the LO cable (up to 70.5° phase change introduced by the cable bending), while an insignificant phase change on the Rx cable (up to 0.5°) was observed. Therefore, the main purpose

of our proposed channel sounder was to compensate the phase change on the LO cable at the Rx side. Note that the phase stability of these Tx and Rx frequency extenders are $\pm 6^\circ$.

2) Phase compensation scheme: The purpose of the phase compensation scheme is to remote the Rx antenna and stabilize the system phase while the Rx antenna rotates. Previous phase compensation schemes for sub-6 GHz and Millimeter Wave (mmWave) [3], [4] are implemented directly on the cable connected to the VNA receiving port. At sub-6 GHz bands, microwave circulators and RF cables are directly used. At mmWave bands, Electrical-to-Optical (E/O) and Optical-to-Electrical (O/E) units up to 50 GHz are used. However, the latter can not be applied directly for sub-THz system, because of lack of such cost-effective conversion units at sub-THz bands. Therefore, due to the introduction of frequency extenders in the sub-THz system and non-stable phase performance in the LO cable, the phase compensation scheme is implemented in the LO cable at the Rx side (as presented in Figure 5). Thus, the same E/O and O/E conversion units at 9.12-13.75 GHz can be used.

2.1.2.2 Principle of operation The forward and feedback links are recorded in the VNA as the $S_{BA}(f_1)$ and $S_{C3}(f_2)$, respectively, where $f_1 = 7.438\text{MHz}$ and $f_2 = 9.12 - 13.75\text{GHz}$. The number of the frequency points N_{f_1} of the received signal is the same as N_{f_2} of the transmitted and that of the LO signals. After using normalization procedure to eliminate the system response in the back-to-back setup, the response of the forward $S_{BA}(f_1)$ and feedback $S_{C3}(f_2)$ links are normalized to 1. In the actual measurement setup, after replacing the back-to-back connection with suitable antennas, the Channel Frequency Response (CFR) $H(f_1)$ can be recorded in $S_{BA}(f_1)$ as:

$$S_{BA}(f_1) = 1 \cdot H_{fw}(f_1) \cdot H(f_1) \quad (2.1)$$

where $H_{fw}(f_1)$ is the frequency response caused by the mechanical stress and thermal changes on the optical fiber.

Similarly, the frequency response in the feedback link, containing the cable effects, $H_{fb}(f_2)$ is incorporated in $S_{C3}(f_2)$ as:

$$S_{C3}(f_2) = 1 \cdot H_{fb}(f_2) = \alpha_{C3}(f_2) \exp(j\phi_{C3}(f_2)) \quad (2.2)$$

where $\alpha_{C3}(f_2)$ and $\phi_{C3}(f_2)$ are respectively the amplitude and the phase of $S_{C3}(f_2)$.

The realized bidirectional signal transfer on the same cable assumes that the signal in the feedback link undergoes twice the phase change in the forward link due to mechanical stress and thermal changes on the optical fiber cable. Therefore, the relation between the response amplitude $\alpha_{LO3}(f_2)$ and phase $\phi_{LO3}(f_2)$ from the LO signal input port to Port 3 and those of $S_{C3}(f_2)$ are:

$$\alpha_{LO3}(f_2) = \sqrt{\alpha_{C3}(f_2)} = \sqrt{|S_{C3}(f_2)|}, \quad (2.3)$$

$$\phi_{LO3}(f_2) = \frac{\phi_{C3}(f_2)}{2}, \quad (2.4)$$

After considering that the signal passes through the multiplier ($24\times$) and the mixer, the amplitude $\alpha_{\text{error}}(f_1)$ and phase $\phi_{\text{error}}(f_1)$ of the error term $H_{fw}(f_1)$ can be represented as:

$$\alpha_{\text{error}}(f_1) \approx \alpha_{\text{LO3}}(f_2) = \sqrt{|S_{C3}(f_2)|} \quad (2.5)$$

$$\phi_{\text{error}}(f_1) = 24 \cdot \phi_{\text{LO3}}(f_2) = 12 \cdot \phi_{C3}(f_2) \quad (2.6)$$

Therefore, the error term $H_{fw}(f_1)$ can be estimated considering (1) and knowing that the CFR $H(f_1)$ can be written as:

$$H(f_1) = \frac{S_{BA}(f_1)}{\sqrt{|S_{C3}(f_2)|} \exp(j \cdot 12 \cdot \phi_{C3}(f_2))} \quad (2.7)$$

2.1.2.3 Link budget analysis Figure 6 shows an example of the link budget of the developed long-range phase-coherent channel sounder.

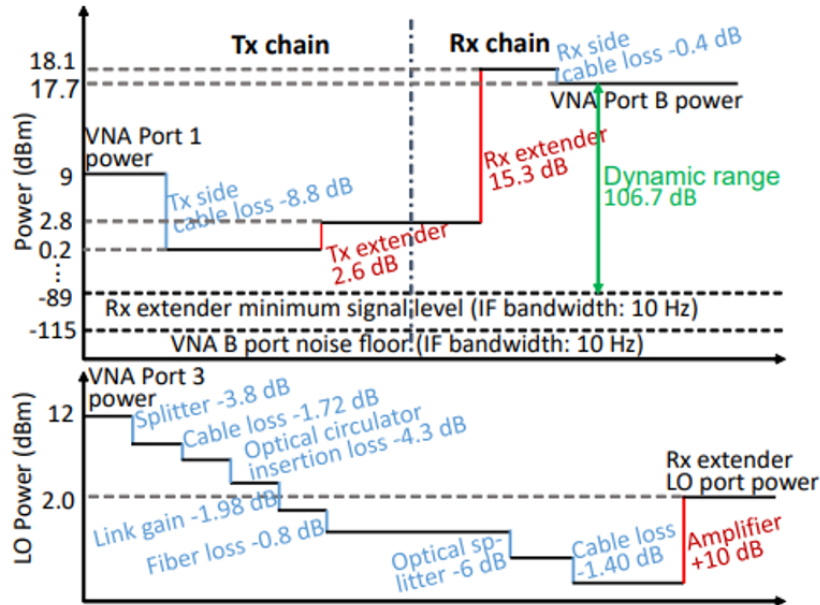


Figure 6: Link budget of the proposed channel sounder and the phase compensation system at 275 GHz and at 11.5 GHz

At the Tx side, 5 m RF cables are utilized to connect the VNA with the Tx extender. At the Rx side, 10 m RF cable and 300 m optical fiber cable are used to remote the Rx antenna. In order to ensure that the Tx extender works safely and prevent potential damage, the transmitted powers from Port 1 and Port 3 are respectively 9 dBm and 12 dBm. Furthermore, the LO signal power is set at 2 dBm by using a RF amplifier operating at 9 – 14GHz with a 10 dB gain and a 1 – dB compression of 11 dBm, thus ensuring also the normal work of the Rx extender. The gains of the Tx extender and Rx extender are 2.6 and 15.3 dB, respectively. The loss of the waveguide is included in the gains of the extenders.

For the back-to-back connection, the obtained dynamic range is 106.7 dB. For the conventional sounding system without RoF techniques, the measurement is limited to several tens of meters, because of the high signal loss in the LO cable at 9.12-13.75 GHz, i.e. 1.5-1.8 dB/m [5].

However, in the proposed sounder, the signal loss in the optical fiber cable could be significantly reduced (i.e. 0.8 dB/km [3]). Therefore, depending on the optical cable length in the sounding system and the free space propagation loss (FSPL) in the practical scenario, the measurement range could be increased up to 300 m.

2.1.2.4 Amplitude and phase stability of the proposed channel sounder Stability of the amplitude and the phase is fundamental for an accurately recording of the characteristics of the channel by the channel sounder [3]. The proposed channel sounder is validated using back-to-back measurements. The amplitude and phase stability are evaluated under the following two conditions - signal drifting over time (thermal change) and cable bending (mechanical stress).

Usually, directional scanning measurements can take several hours. Therefore, it is important to ensure that there is insignificant signal drift in the measurement system during the entire measurement period. However, according to the work in [6], the changes in the ambient temperature leads to a significant phase change to the signal in the optical fiber cable. Figure 7 shows photo of the back-to-back and the cable bending measurements.

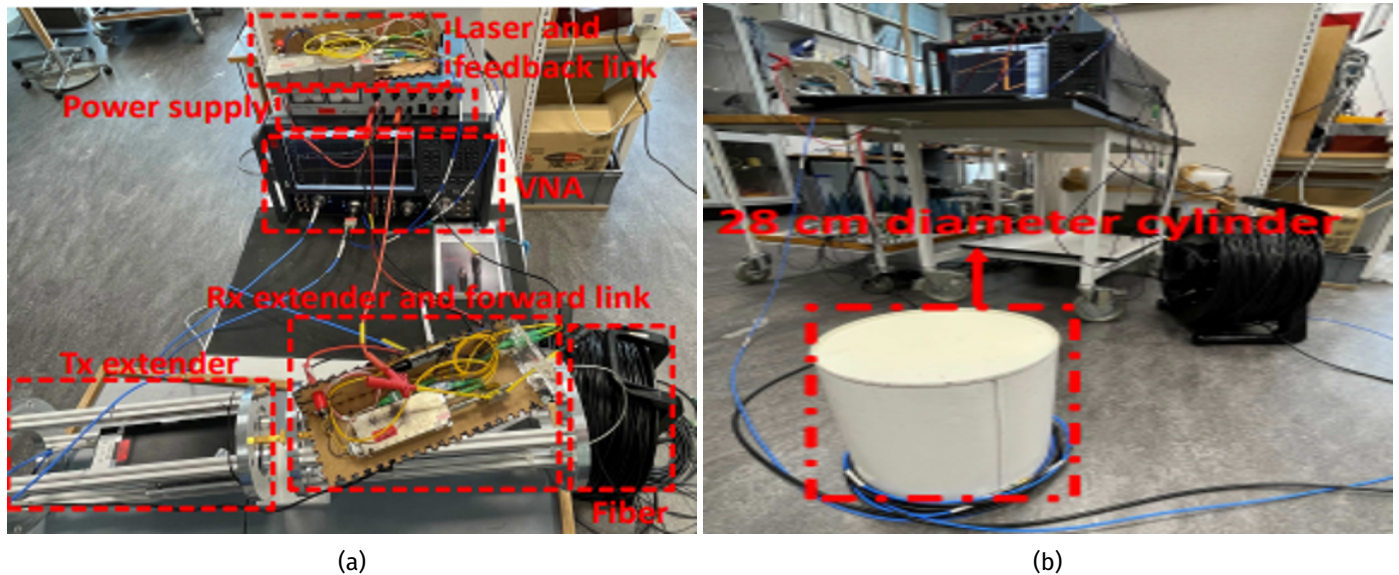
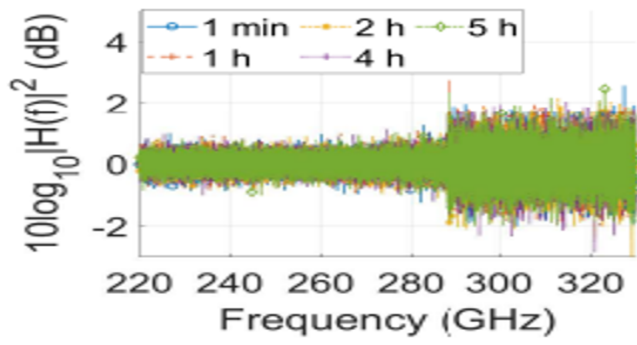


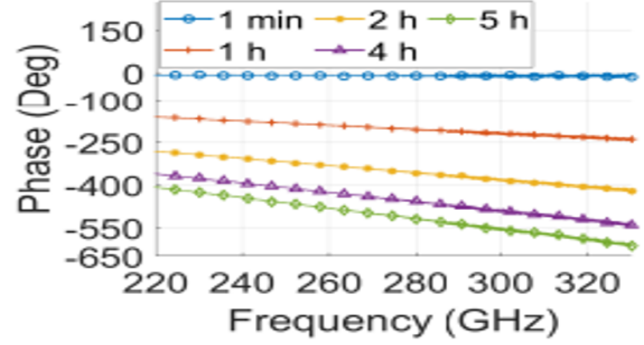
Figure 7: Photo of the back-to-back and the cable bending measurements a) Back-to-back measurement b) Mechanical bending of the optical fiber and Rx coaxial cables

In order to validate the robustness of the proposed channel sounder, a back-to-back measurement is performed, as shown in Figure 7a. The VNA and the RF amplifier are turned on to warm up 30 minutes prior to the measurements. The system response is deemed before the measurements by performing a normalization procedure, resulting in an effective shift of the phase reference from the VNA ports to the calibration reference plane, as shown in Figure 5. During the measurements, a frequency sweep from 220 to 330 GHz with frequency points of 20001 is done continuously for a period of 5 hours with an interval of 1 minute.

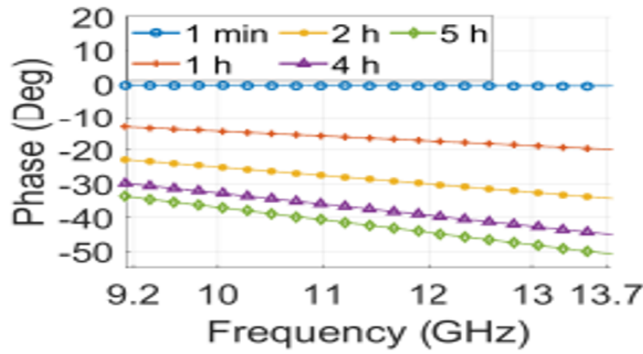
The amplitude and phase results with the RF amplifier included over a period of 5 hours are shown in Figure 8.



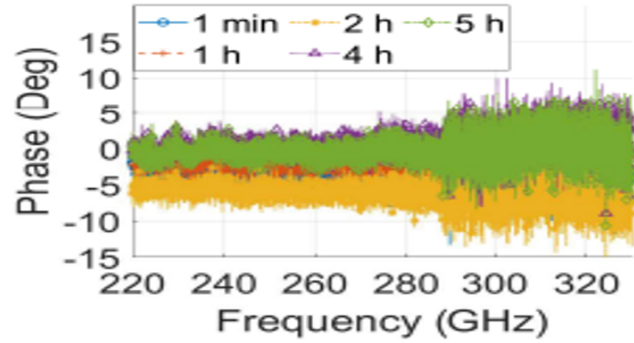
(a)



(b)



(c)

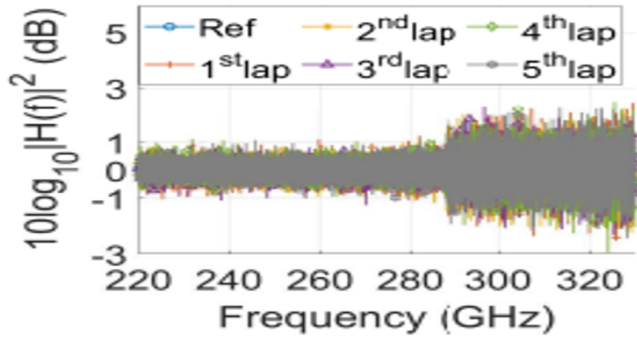


(d)

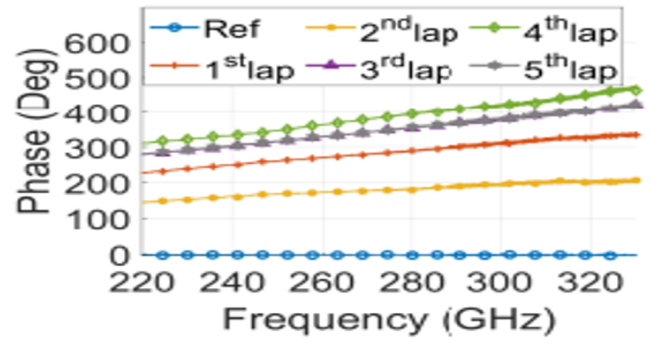
Figure 8: Amplitude and phase of the proposed channel sounder over a period of 5 hours a) Compensated amplitude b) Phase of the forward link c) Phase of the feedback link d) Compensated phase

For the frequency range of 220-288 GHz, the amplitude varies within 1 dB. However, the amplitude for the frequency range 288-330 GHz changes in the range of $[-2.8, 2.4]$ [dB]. It is observed that the phase of the forward link varies over 500° and is approximately twelve times higher than the phase of the feedback link, as demonstrated in Figure 8b and Figure 8c. The compensated phase deviation for the period of 5 hours is maintained within 12° at 220-288 GHz and 37° at 288-330 GHz, respectively (as it is shown in Figure 8c). Moreover, the phase noise at 288-330 GHz is found to be much higher than that at 220-288 GHz, which is due to the multiplier and mixer inside the Rx extender. Unfortunately, the latter is a subject to manufacturer designs. It is worth it to note that even a small phase error variation will become 24 times larger due to the effect of the multiplier. The real error of the phase compensation system is much lower (e.g., 1.5° phase error before the multiplier, which corresponds to 36° after it). These results indicate the robustness of this proposed phase-compensated channel sounder under the condition of conducting measurements in 5 hours.

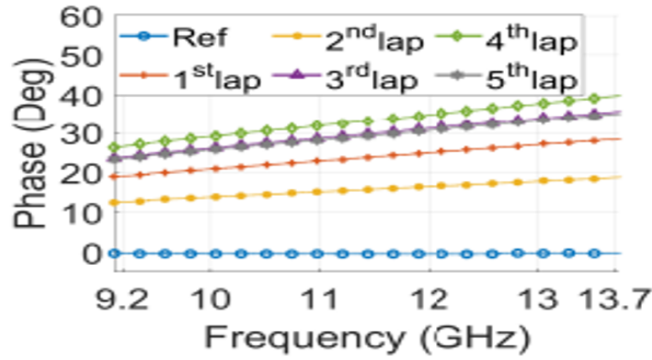
Figure 9 shows the amplitude and phase results when performing mechanical stress by bending the cable.



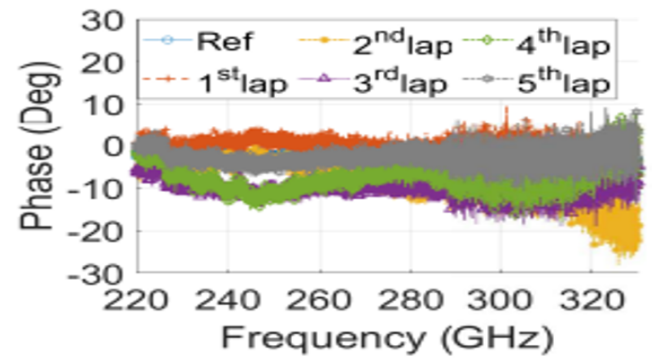
(a)



(b)



(c)



(d)

Figure 9: Amplitude and phase of the proposed channel sounder with cable bending a) Compensated amplitude b) Phase of the forward link c) Phase of the feedback link d) Compensated phase

In practical directional scanning measurements, at the R_x side, the mechanical stresses on the optical fiber and Rx coaxial cables are unavoidable owing to the movement of the antenna positioning stages. In order to characterize the cable bending, a 28 cm cylinder is used to bend the cables, as it was illustrated in Figure 7b. The channel responses are measured for a total of 5 twists around the cylinder. As shown in Figure 9b, the phase of the forward link is observed to be unstable and varying over 400°. Compared with Figure 9b and Figure 9c, the phase of the forward link is approximately twelve times higher than the phase of the feedback link. After the phase compensation procedure, the phase due to mechanical stress is observed to be maintained within 15° at the frequency range of 220-288 GHz and within 30° at the frequency range of 288-330 GHz, respectively, as shown in Figure 9d.

2.1.2.5 Conclusion In this subsection, a novel sub-THz VNA-based long-range phase compensated channel sounder at 220-330 GHz is proposed. The dynamic range of this channel sounder could be improved to 106.7 dB for the back-to-back connection at 275 GHz to support the long-range channel measurements. By using the RoF technique and phase compensation scheme, the long-range phase-coherent channel measurement could be conducted. The robustness of this novel channel sounder is validated and specified for the frequency range from 220 to 330 GHz by back-to-back measurements. The phases after compensation at 220-288 GHz and 288-330 GHz are within 15° and 37°, respectively, compared to over 400 ° phase change introduced by cable effect at 220 – 330GHz.

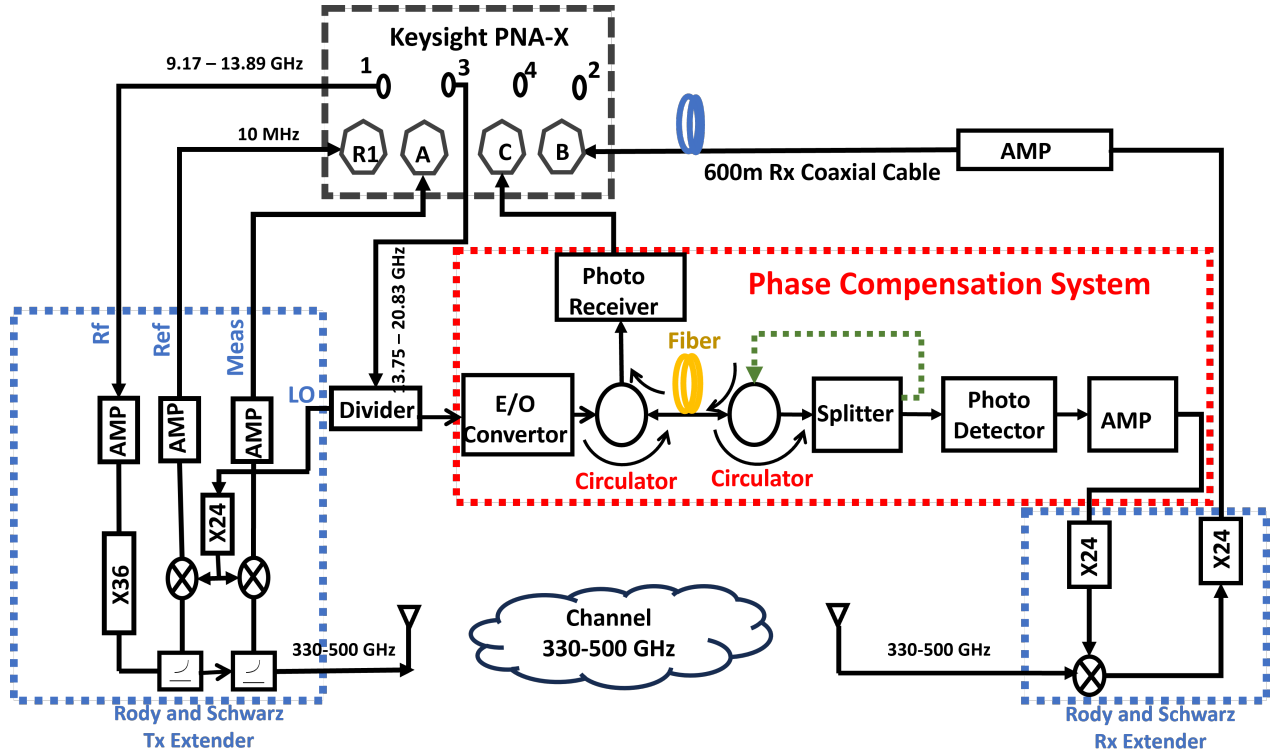


Figure 10: Block diagram of the proposed RoF VNA-based sub-THz channel sounder(330-500 GHz)

2.1.3 Application of a phase compensated RoF system to 500 GHz channel sounding This subsection extends the previous work by applying the phase-compensated RoF technique to channel sounding across the 330–500 GHz frequency range. It introduces a novel, dynamic-range-adjustable design for a long-range sub-THz channel sounder based on a VNA. The system integrates power-adjustable RoF technologies with a phase compensation mechanism, both of which are analyzed in detail. Furthermore, link budget performance has been evaluated for optical fiber lengths of up to 600 meters.

2.1.3.1 Channel sounder structure Figure 10 presents the block diagram of the proposed sub-THz channel sounder. The short-range VNA-based sounder, designed for measurements up to 0.23 meters and operates between 330 GHz and 500 GHz. This system features a Keysight Technologies four-port PNA-X VNA (operating natively up to 67 GHz) paired with Virginia Diodes Inc. R&S®ZC500 VNA Extenders, expanding the frequency range to 330-500 GHz, and includes Standard Gain Horn (SGH)-26-WR2.2 horn antennas. The VNAX units perform frequency conversion to sub-THz bands via integrated multipliers, mixers, and filters, but the measurement range is constrained by signal losses in the coaxial cables connecting the VNA to the extenders. A dynamic range adjustable optical-power phase-compensated electro-optical setup is employed at the receiver to address phase drift in long-range sub-THz frequency-domain RoF systems. This includes power-adjustable electro-optical (EO) and optoelectrical (OE) converters, with 600 m fiber optic cable acting as the transmission medium for the LO signal. The phase compensation mechanism uses two three-port optical circulators based on bidirectional signal transfer (forward and feedback) through the same optical fiber. This feedback link helps de-embed impairments caused by the cable's thermal variations or mechanical stress. The output amplitude from the OE converter in the LO forward path requires amplification to match the input power requirements of the frequency extender's LO input. To achieve this, a Minicircuits ZX60-06183LN+ amplifier, which operates between

6 GHz and 18 GHz with a typical gain of 20 dB, has been selected. Additionally, the IF measurement signal must be transmitted over a 600-meter distance. At its frequency of 10 MHz, this signal can be transmitted over coaxial cable with manageable signal loss. An RG58U cable, introducing about 25 dB of attenuation over 600 m, was chosen for this purpose. To further compensate for the signal loss and maintain the system's dynamic range, a second amplifier, the Mini-Circuits ZFL-500LN+ (operating from 0.1 MHz to 500 MHz with a typical gain of 28 dB), is employed.

2.1.3.2 Channel Sounder Link Budget Assessment A link budget analysis is required for two key links in the system to validate the performance of the proposed long-range sub-THz channel-sounding setup. The first key link starts at VNA Port 1, runs through the transmitting extender head, passes into the receiving extender head, and loops back to the VNA through a measurement RF amplifier and 600 meters of coaxial cable. The transmit power at VNA Port 1 is set to 7.2 dBm, ensuring it falls within the VNAX drive range of 10 ± 3 dBm. After factoring in the amplification and losses from the cable, the power received at the VNA input port is measured to be -18 dBm. A 10 MHz intermediate frequency (IF) was selected as a compromise between reducing signal loss over the 600 m coaxial link and maintaining the optimal performance of the PNA-X and extender heads, which are optimized for 279 MHz operation. However, using frequencies below 50 MHz can lead to a lower dynamic range in the PNA-X VNA due to increased trace noise, which can affect the precision of the measurements.

The other link LO signal path to the remote Rx extender head over the RoF system. At the 425 GHz test frequency, the LO signal is 11.71 GHz. VNA Port 3 is set to 10 dBm, ensuring sufficient power after the frequency divider connects the LO of Tx frequency extender. The optical system, with a link loss of 12.8 dB, includes EO and OE converters. The photo-receiver gain has been adjusted to work with the amplifier to meet extender head specifications, resulting in a higher-than-minimum link loss. An RF amplifier with 20 dB gain and a 6 GHz–18 GHz bandwidth has been chosen. Despite the long-range link, the system meets the LO drive power requirements and provides an additional 3 dB gain for the measurement IF signal, demonstrating successful operation over the 600 m Link.

2.1.4 Application of a phase compensated RoF system to 750 GHz channel sounding This sub-section builds on the work in the previous section by applying the phase compensated RoF technique to channel sounding in the 500 - 750 GHz frequency range. This comprises of a novel dynamic range adjustable design of a long-range sub-THz VNA-based channel sounder system using both power adjustable RoF technologies [7] and a phase compensation mechanism which will be analysed. Additionally, the operating link budget with up to 600 m of optical fibre has been assessed.

2.1.4.1 Channel sounder structure Using the RoF technologies, the implemented design for a dynamic range adjustable long-range sub-THz frequency-domain phased-compensated VNA-based channel sounder system operating between 500 GHz and 750 GHz is shown in figure 11.

This consists of a power-adjustable electro-optical (EO) converter, opto-electrical (OE) converter and fibre optic cables as the transmission path for the LO signal. The targeted channel sounding range is up to 600 m, hence an optical fibre length of 600 m is employed. For the frequency upconverter unit at the Tx end, four connections are required, namely, the radio frequency (RF, 9.26 – 13.89 GHz), local oscillator (LO, 9.26 GHz – 13.89 GHz), IF measure (7.438 MHz) and IF reference (7.438 MHz). For the frequency downconverter unit at the Rx end, this is reduced to two connections, LO (9.26 GHz – 13.89 GHz) and IF measure (7.438 MHz).

These connections must be routed back to the VNA to form the measurement system. For the Tx side, the fre-

Sub-THz Channel Sounder - Rear Panel Configuration - 12/04/2024

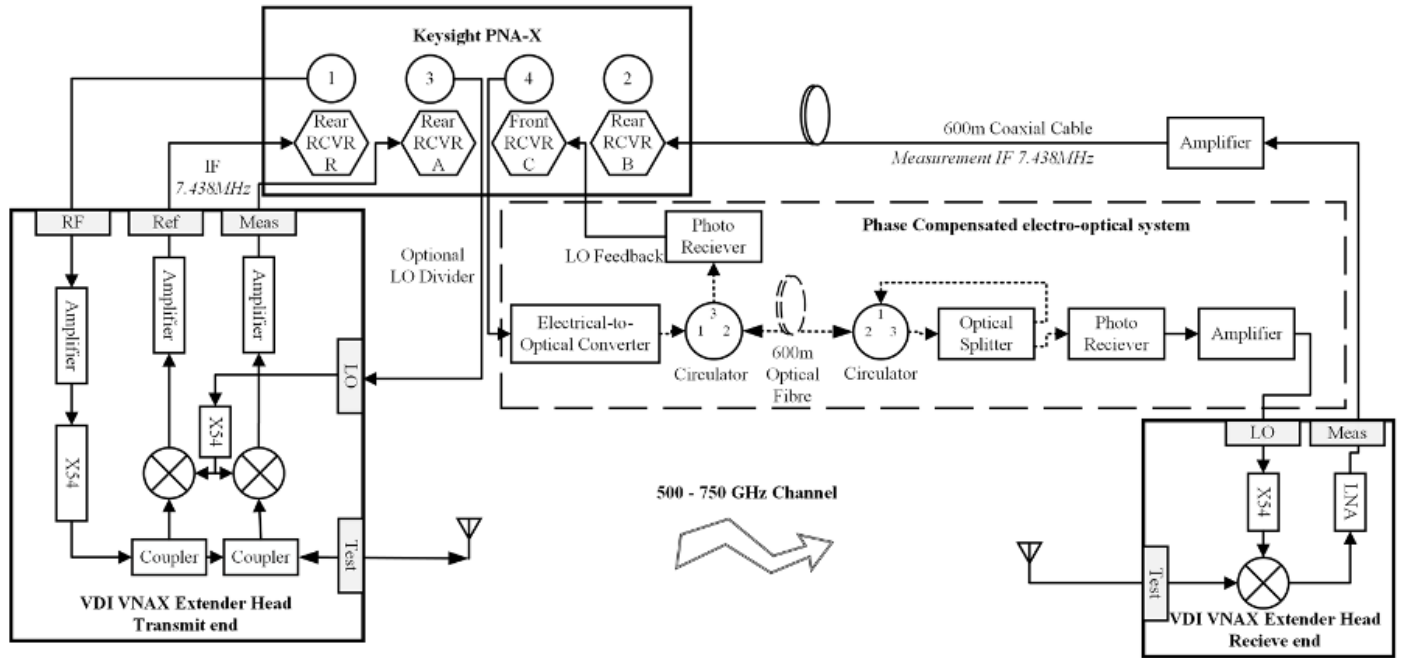


Figure 11: Block diagram of the NPL long-range 750 GHz sub-THz VNA-based channel sounder

quency extender head is located nearby to the VNA allowing for short coaxial RF cables to be used for the connections. As the Rx frequency extender head could be located up to 600 meters away from the VNA, a RoF solution is used as the loss in coaxial RF cables would be too great to allow for measurements to be performed. However due to the phase-stability issues with the RoF solution, phase compensation must be performed to correct for this effect.

Phase compensation techniques have been included in the system using two, three-port optical circulators. From the EO unit, the 1550 nm optical signal is passed forward through an optical circulator and then into the extended 600 m fibre optic cable towards the remote Rx antenna. With the optical signal at the Rx end of the measurement, it is again passed through an optical circulator and then equally divided into two signals by an optical splitter. The first to an OE converter to provide the LO signal to the remote Rx frequency extender unit. The second signal from the splitter is fed to the optical circulator closest to the Rx end where it is used to feedback the signal through the 600 m of fibre optic cable. The feedback signal is isolated from the forward signal by the initial optical circulator and through the feedback OE converter the phase of the feedback signal can be monitored on the VNA. Such a setup enables bidirectional signal transfer through the same 600 m optical fibre cable to allow monitoring at the VNA of the phase drift along the fibre's length. Assuming the phase shift imparted by each propagation along the cable is equal regardless of the direction, the feedback signal will exhibit twice the phase change exhibited at the end of the forward path. This can then be used to de-embed the phase change of the cable over time in post-processing, maintaining a sufficiently accurate calibration over the measurement duration.

The output amplitude of the LO receiver end OE converter requires an amplifier to meet the input power level specifications of the frequency extender LO input. A Minicircuits ZX60-06183LN+ amplifier operating between 6 GHz – 18

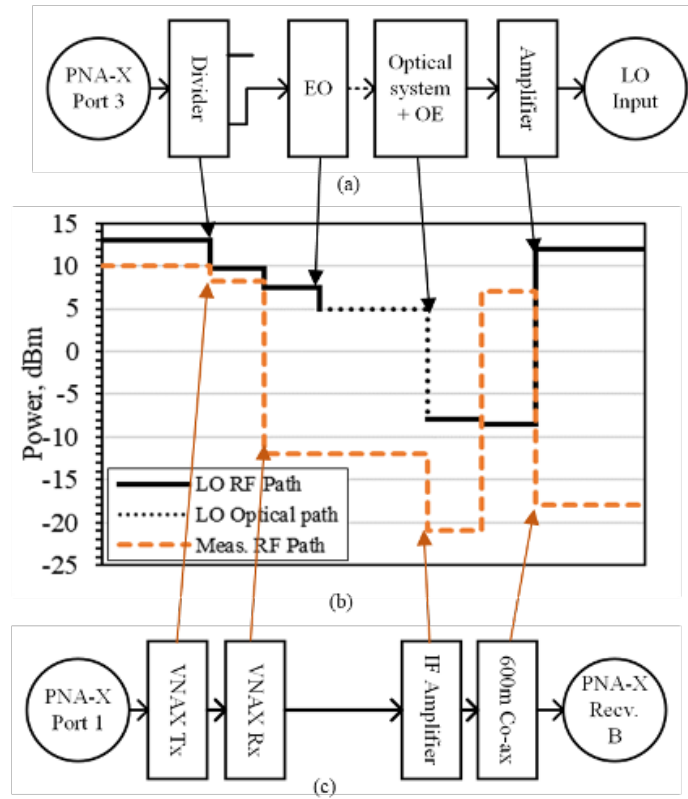


Figure 12: Link budget and power measurements (b) with a simplified system diagram from the Long-Range sub-THz VNA-Based Channel Sounder for the (a) LO signal paths and (c) measurement signal path correlated vertically

GHz with a typical gain of 20 dB has been selected. The measurement IF signal is also required to be routed over 600 m. The 7.438 MHz frequency of this signal allows transmission over an appropriate length of coaxial cable with manageable attenuation. An RG58U cable, providing approximately 25 dB of attenuation over 600 m, has been selected. A second amplifier, a Mini-Circuits ZFL-500LN+ (0.1 MHz – 500 MHz with typical 28 dB gain) is connected to reduce the effect of the cable losses on the system measurement dynamic range.

2.1.4.2 Channel Sounder Link Budget Assessment To validate the proposed long-range sub-THz channel-sounding system, a link budget analysis is required for two primary signal paths. The analysis is based on an operating frequency of 625 GHz (mid-band), with the frequency extender heads configured in a through connection - their waveguide test ports are directly connected.

The first signal path of interest is the measurement signal path, illustrated in Figure 12 (c). This path is established from VNA Port 1, passing through the transmitting frequency extender head and into the receiving extender head. The signal then returns to the VNA via a measurement RF amplifier and a 600-meter coaxial cable.

The transmit power from the VNA Port 1 is configured at 10 dBm to remain within the VNAX system's drive specifications, of 7 dBm to 13 dBm. After amplification and accounting for losses incurred through the coaxial cable, the received power at the VNA is measured at -18 dBm. A 7.438 MHz IF signal is selected for the measurement, representing a compromise between attenuation over the 600-meter coaxial link and the operational characteristics of the PNA VNA and extender heads, which are optimized for operation at 279 MHz. Additionally, the selection of 7.438 MHz avoids the reduced dynamic range associated with IF signals below 50 MHz of the Keysight PNA, as these can be directly connected

to the PNA IF inputs.

The second signal path under consideration, shown in Figure 12 corresponds to the LO signal for the remote receiving frequency extender via the RoF system. At the 625 GHz operating frequency, the corresponding LO signal is 11.57 GHz. The power at VNA Ports 3 and 4 are set to 13 dBm to ensure adequate signal strength after the coaxial cables. The first port connects to the local transmitting extender via a one-meter coaxial cable. The second port supplies the remote receiving extender via the RoF system, which comprises an electro-optical (EO) converter, 600 meters of optical fibre, additional optical components, and a photo-receiver.

The cumulative link loss through the optical path, including the effects of EO and optical-to-electrical (OE) conversion, amounts to 12.8 dB. To comply with the input power requirements of the extender head, the gain of the photo-receiver has been intentionally reduced to function effectively in combination with a following RF amplifier. This results in an optical link loss that is greater than the minimum achievable. The RF amplifier used in this configuration typically provides 20 dB of gain, with a 1 dB compression point of 16 dBm and a bandwidth spanning 6 GHz to 18 GHz.

When compared to a conventional short-range configuration in which the LO signal is supplied directly from the VNA, the RoF setup meets the required LO drive power specifications for the frequency extender heads. Moreover, the IF signal experiences an additional 3 dB of gain across the measurement link, resulting in equivalent operating conditions between the non-RoF and RoF configurations.

2.2 Channel measurements with Omni-VAA, Dir-VAA and DSS schemes at 100 GHz and at 300 GHz in various deployment scenarios

2.2.1 Short-range channel measurements at 100 and 300 GHz The presented work in [1] serves as a basis for this section. The sub-THz channel sounders presented in section 2.1.1 were used in the measurements. As illustrated in Figure 13, directional measurements were carried out in a rich scatterers laboratory scenario.

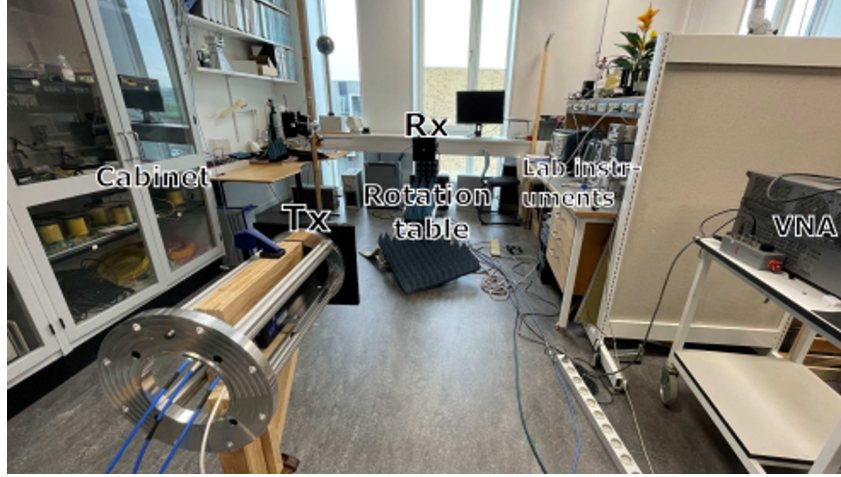


Figure 13: Photo of the laboratory scenario

Details about the measurement setup are presented in Table I. Two sub-THz frequency bands 90 to 110 GHz and 250 to 300 GHz were used for the tests. Two identical horn antennas, one for the Tx side and one for the Rx side, were used in a directional measurement scheme at the Rx side during the measurements at each frequency band. The Tx antenna was stationary, while the bore-sight of the Rx was configured to rotate in azimuth in steps of 1 degree, or 360 steps, within the range of $[-180, 179]^\circ$.

Figure 14 presents the Power Angle Delay Profile (PADP)s from the measured data.

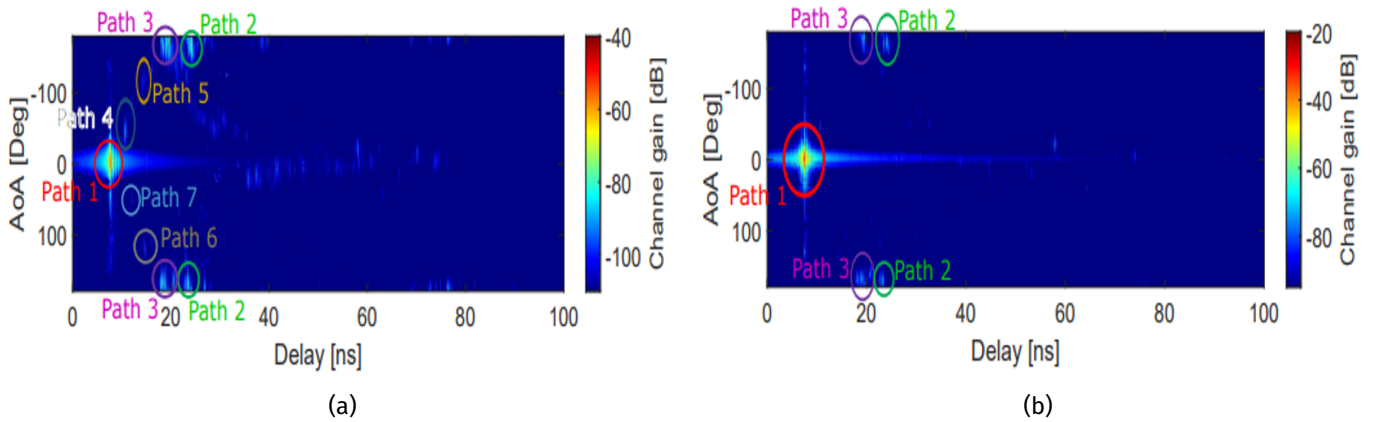


Figure 14: PADPs of the directional measurements at a) 90-110 GHz b) 220-330 GHz

Figure 15 illustrates the identified multi-path component (MPC)s and the scenario.

array (ELAA). A modified classical beamforming (BF) algorithm is used to acquire extremely high angular resolution. The measured narrowband power-angle-spectra (PAS) at 300 GHz from the DSS and VAA schemes are compared to confirm the high angular resolution obtained by the VAA scheme. The wideband PADPs for the DSS and VAA schemes are presented and analyzed. Finally, the the extracted from the PADPs MPCs are then compared with the room geometry. It was found that the parameters of the MPCs, i.e., delay and angles of arrival (AoA), are consistent with the room geometry.

Initially, the phase fluctuation caused by the movement of the turntable is investigated by conducting a simple field measurement in a chamber at 300 GHz. The phase is recorded for a period of time 8 s after one turntable movement. After normalization of the system and the channel responses, the phase fluctuation results were directly obtained (see Figure 16).

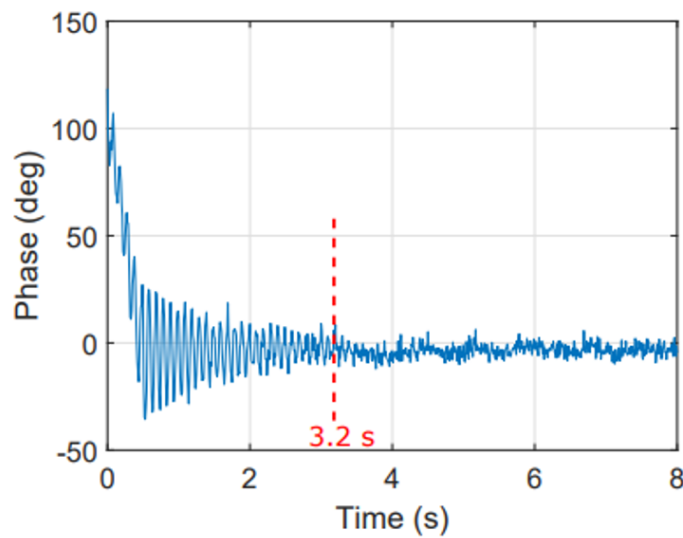
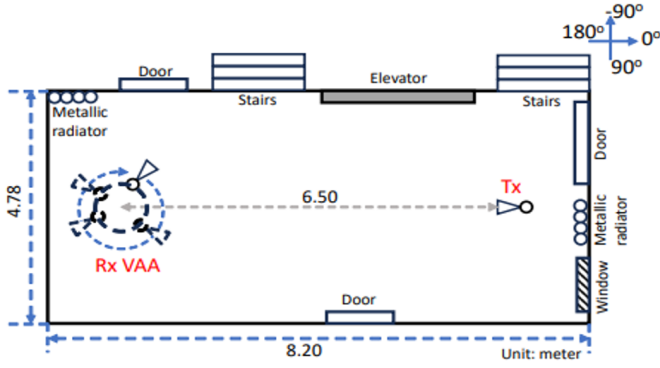
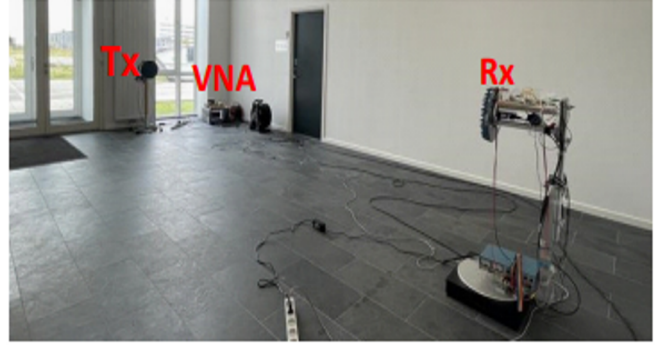


Figure 16: The phase fluctuation results

The results show that the phase fluctuates within a range with a span over 135° . However, the phase becomes stable after 3.2 s. Therefore, 3.5 s has been used as a waiting time (in the VAA measurements) after the turntable rotates. For the field measurements, the measured frequency band is 295-305 GHz with the number of frequency points of 5001. The Intermediate Frequency Bandwidth (IFBW) is set to 500 Hz to obtain good dynamic range. The maximum detectable delay is 500 ns and the maximum detectable path length is 150 m. The simplified diagram and photos of the measurement scenario are depicted in Figure 17.



(a)



(b)

Figure 17: The diagram and photo of the measurement scenario a) Diagram of the scenario and Tx and Rx deployment b) Photo of the scenario

The measurements are conducted at an entrance hall with the size of 8.20 m x 4.78 m x 8 m. The distance between the Tx and the Rx is 6.5 m. The height of the Tx and Rx is 1.25 m. The position of the Tx is fixed, while the Rx is mounted on a turntable to form a virtual UCA with a radius r of 9.5 cm and a rotation step of 0.3° , which corresponds to 1200 antenna array elements. The Fraunhofer distance equation (see eq. (5.15 in Appendix)) defines the distance for the Far-Field (FF) case of this VAA d_{far} and it is equal to 72.2 m.

The distance between the adjacent array elements is 0.497 mm, which is close enough to the half-wavelength of the highest measured frequency 305 GHz, i.e., 0.491 mm. The antenna used on the Tx side is a SGH antenna with a wide azimuth HPBW of 36° and antenna gain of 15 dBi. Two types of SGH antenna are used to form the virtual UCA, i.e., wide-HPBW case and narrow-HPBW case. In the wide-HPBW case, the same antenna used at the Tx is utilized as the array element, while in the narrow-HPBW case, the used antenna has gain of 25.5 dBi and azimuth HPBW of 8° . The measurement time for a virtual UCA is approximately 8 hours. The VAA setup and measurement configurations are listed in Table III.

TABLE III
VAA AND SCENARIO CONFIGURATIONS

Parameter	Value	Parameter	Value
Frequency	295 – 305GHz	Frequency bandwidth	10 GHz
Number of points	5001	IF bandwidth	500 Hz
Transmitted power	10 dBm	Tx & Rx height	1.25 m
VAA Radius	9.5 cm	Rotation step	0.3°
Number of elements	1200	Tx-Rx distance	6.50 m
Typ. Tx antenna gain	15 dBi	Typ. Tx HPBW	36°
Wide-HPBW case			
Typ. Rx antenna gain	15 dBi	Typ. Rx HPBW	36°
Narrow-HPBW case			
Typ. Rx antenna gain	25.5 dBi	Typ. Rx HPBW	8°

From the VAA measurements, CFR for each VAA element can be directly obtained, and the measured CIRs can be estimated by using the inverse discrete Fourier transform (IDFT). In the current work, the CFRs are processed further

by applying the modified classical beamforming (MCBF) algorithm [9] to obtain spatial channel profiles with a higher angular resolution for Dir-VAA scheme. In the algorithm, a window function is applied to select the effective antenna array elements to form a synthesized beam. The size of the window for the wide-HPBW is 200 elements and for the narrow-HPBW case is 120-elements, which corresponds respectively to 60° and 36° . Figure 18 illustrates the comparison between the measured and beamformed PASs at 300 GHz in both wide-HPBW and narrow-HPBW cases.

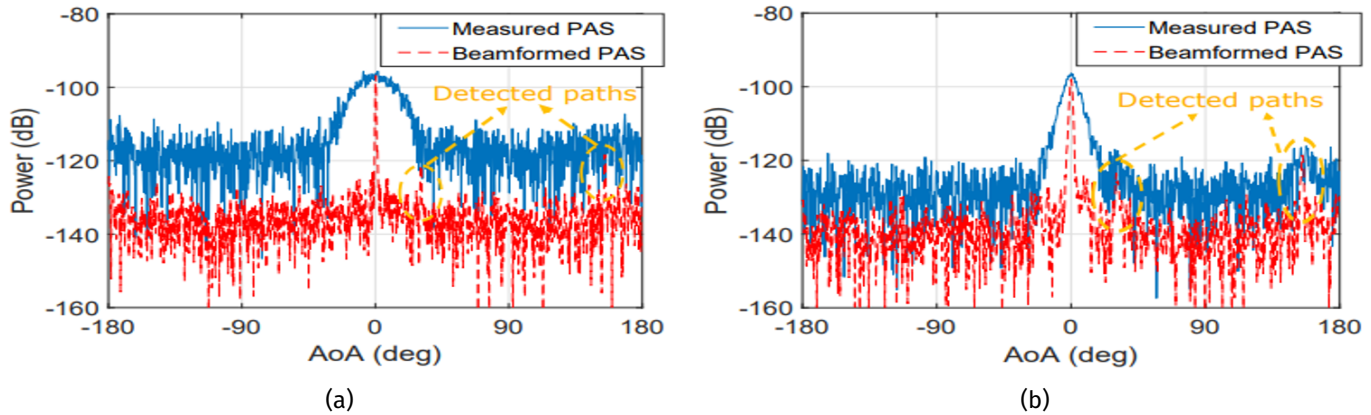


Figure 18: Comparison of the measured PAS and beamformed PAS at 300 GHz (narrowband) in both cases a) Wide-HPBW case b) Narrow-HPBW case

The measured PAS is the power measured per orientation angle of the measurement antenna, which is obtained directly by considering the measured CFR at the single frequency, i.e., 300 GHz, while the beamformed PAS is obtained by applying the abovementioned beamforming algorithm to the measured PAS. As one would expect, the measured PAS in the wide-HPBW case has a low angular resolution, i.e., with a measured HPBW of 33° at 300 GHz, while the measured PAS in the narrow-HPBW case has a slightly higher angular resolution (a measured HPBW of 7.2°) at 300 GHz. Moreover, due to the low antenna gain of the employed antenna in the wide-HPBW case, MPCs can not be detected, because the dynamic range is too limited. The beam achieved by the VAA scheme can be synthesized and a higher angular resolution can be obtained after applying the modified BF algorithm. The HPBWs of the synthesized beam in the wide-HPBW case is 0.6° and in the narrow-HPBW case 1.5° . Furthermore, with the help of the BF array gain, the dynamic range can be further improved with the help of the BF array gain. The effectiveness of the VAA scheme can be validated by the increased number of MPCs detected after BF (three) compared to only one dominant path in the measured PAS. Moreover, the VAA scheme is highly effective both for the wide HPBW and narrow HPBW cases. Both beamformed patterns provide excellent spatial resolution and improved significantly dynamic range. The wide-HPBW case provide slightly better spatial resolution results, possibly due to the more effective VAA elements that are selected, which can be seen as an optimal balance between the array gain and angular resolution compared to the Omni-VAA and narrow-HPBW case. Figure 19 shows the comparison between the PADPs for the DSS and VAA schemes in the wide-HPBW case. The comparison between the PADPs for the DSS and VAA schemes in the narrow-HPBW case is presented in Figure 20.

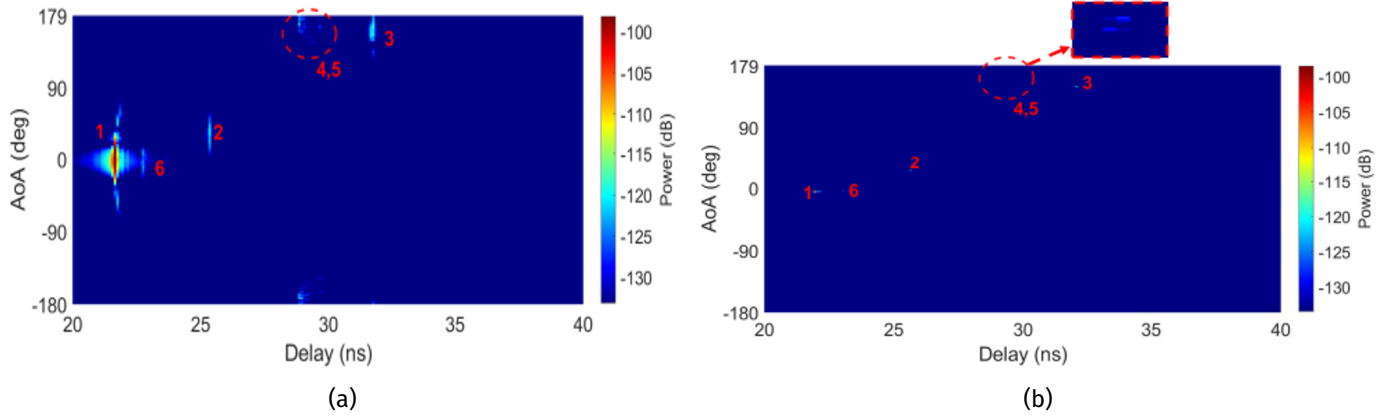


Figure 19: PADPs for the DSS and VAA schemes in the wide-HPBW case a) DSS scheme b) VAA scheme

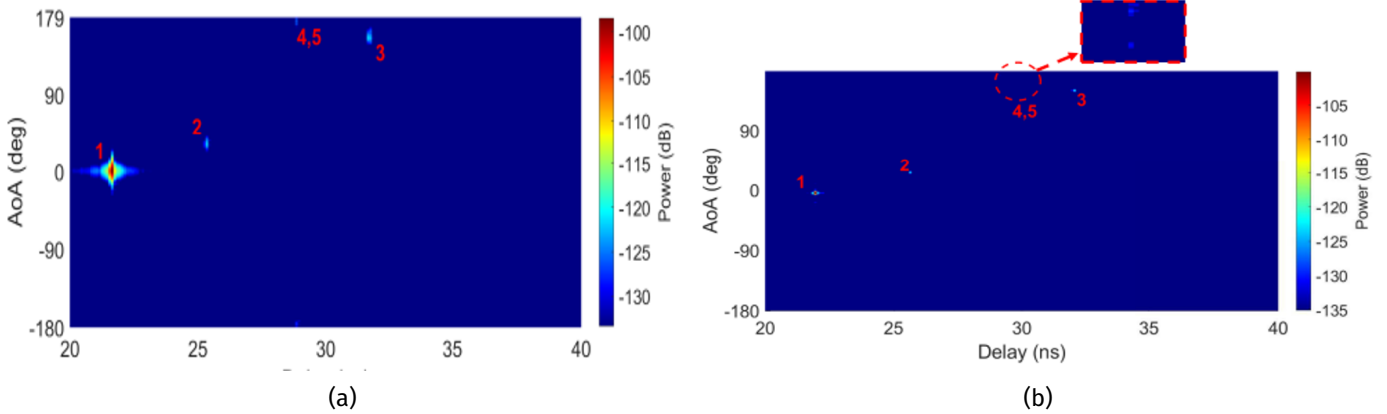


Figure 20: PADPs for the DSS and VAA schemes in the narrow-HPBW case a) DSS scheme b) VAA scheme

In order to distinguish the MPCs, the dynamic range is set to 35 dB. The wide bandwidth 10 GHz used in the measurements also contribute to the identification of the MPCs in the delay domain. The comparison of the PADPs demonstrates that the high angular resolution can be achieved by the use of the phase-coherent VAA scheme. Moreover, as expected, the measured 300 GHz channels in this scenario are found to be sparse and specular. Six MPCs are detected in the wide-HPBW case. The measured power level of the LoS path is -97.17 dB, while the delay and the angle of the LoS path are respectively 21.6 ns and 0°. The measured delay corresponds to the distance of 6.48 m, which is close to the realistic Tx to Rx distance in the measurements, while the measured LoS power level matches well to the FSPL, i.e. 98.22 dB. Paths 2-5 are found to be the reflections from different walls. The power of the LoS path after applying the BF algorithm is -98.24 dB, which is also close to the measured LoS power and the FSPL. Furthermore, the delay and angle of the LoS path are observed to be the same as those of the measured LoS. Paths 2-6 for the VAA scheme are observed to match well those in the PADP for the DSS scheme.

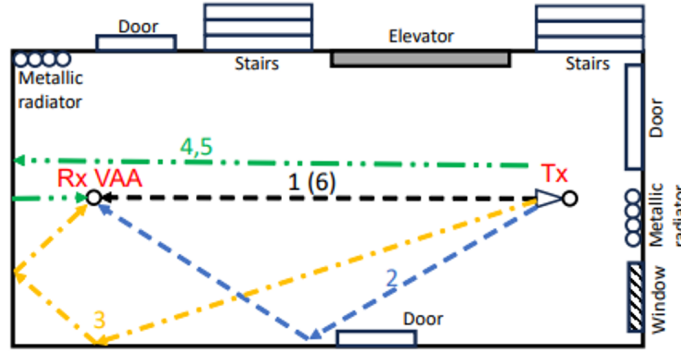


Figure 21: The relationship between the MPC parameters and the entrance geometry

Five MPCs are found in the narrow-HPBW case. The power of the measured LoS is observed to be -98.43 dB. The LoS delay and angle are respectively 21.6 ns and 0° . After applying the BF, the LoS power, delay, and angle are -100.06 dB, 21.6 ns, and 0° , respectively. The parameters (i.e., power, delay, and angle) of paths 2-5 are found to be close to those in the wide-HPBW case. Path 6 in the wide-HPBW case is formed by reflection from the ground due to the wide HPBW of the array element in the elevation plane (i.e., 29.71°) compared to only 6° HPBW in the elevation of the antenna in the narrow-HPBW case. The height of the ceiling is 3.8 m. By using the geometry, the elevation angle of the reflection from the ceiling is found to be 38° . However, it is difficult to observe the reflection from the ceiling in the results. Based on the estimated multipath parameters and the room geometry, the path trajectory presented in Figure 21, are in good agreement with the room geometry. Reflection from the elevator is not observed due to the narrow azimuth HPBW of the Tx antenna.

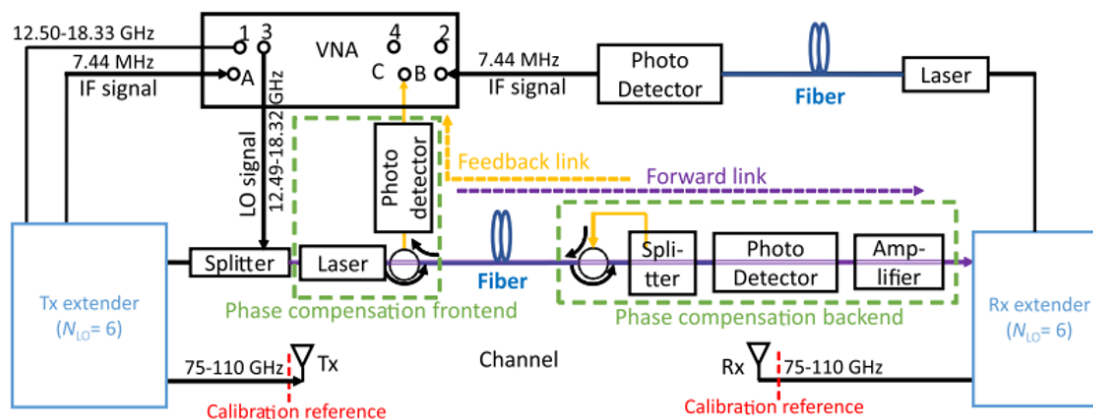
In this section, the first field measurements (up to the date of the publication of [8]) using the VAA scheme at 300 GHz in a empty entrance room scenario at 295 - 305 GHz is presented. The VAA was designed to be in a form of a virtual UCA with a radius of 9.5 cm and 1200 array elements. The PAS and PADP with DSS and VAA schemes were shown and compared for two types of directional antennas with different HPBW. The measured results demonstrated the effectiveness of the VAA scheme, by the provided from the VAA scheme significantly improved dynamic range and spatial resolution.

2.2.3 Virtual Antenna Array for W-Band Channel Sounding: Design, Implementation, and Experimental Validation

2.2.3.1 Introduction A phase-compensated RoF-enabled VNA-based channel sounder at the W-band, i.e., 75 - 110 GHz is proposed in [10]. The content of the subchapter is based on the abovementioned work. Firstly, the phase issue in the channel sounding system at sub-THz bands is described and measured in the back-to-back connection. The simulated beamforming results without phase compensation are evaluated and compared with the reference results based on the empirical phase changes. After the estimation of the impact of the phase change, a phase-compensated VNA-based channel sounder is proposed at W-bands and it is validated in the back-to-back connection. Additionally, VAA-based channel measurement campaign is carried out in a hall scenario at 100 GHz for two distances - 7.3 m and 84.5 m. A high-resolution channel parameter estimator, i.e., frequency-invariant beam-forming (FIBF) with successive interference cancellation (SIC) is used to extract the parameters of the paths. The FIBF algorithm is also generalized for a UCA composed of the omnidirectional antenna (it has been reported in the literature) and directive antenna (it

is proposed here). The estimation results obtained with both Omni-VAA and Dir-VAA are then validated by comparing the estimated multi-path parameters with the reference DSS results. For detailed descriptions of the channel spatial profile measurement method, i.e., Omni-VAA, Dir-VAA, and DSS, readers can refer to [11].

2.2.3.2 Proposed channel sounder architecture Figure 22 shows the proposed long-range phase-compensated VNA-based channel sounder at the W-band.



The VNA transmits the input signal in the frequency range of 12.50–18.33 GHz from port 1 and the LO signal in the

frequency range of 12.49–18.32 GHz from port 3, respectively. Then, the input signal is up-converted to the frequency range of 75–110 GHz and transmitted via the Tx antenna. A splitter is used to split the LO signal and multiplied by a factor of $N_{LO} = 6$ to down-convert the RF signal to the IF signal at 7.44 MHz. Then, the down-converted IF signals at both Tx and Rx sides are recorded in port A and port B, respectively. Both the RoF scheme and phase-compensation scheme are included in the LO cable at the Rx side to extend the Rx for long-range measurements and to make the phase stable during the measurements. The main principle of the phase compensation scheme is that a feedback connection to record the phase change of the signal is created via the optical circulators and splitter. As it was discussed in previous subchapters, the phase change (instability) is caused mainly by the thermal change and mechanical stress in the fibers, which deteriorates the properties and the physical structure of the fibers [12], [13]. The principle of the phase compensation concept is supported by equations (1)-(6) in [10]. For more details, the reader can refer to it.

2.2.3.3 Channel parameter estimator. Numerical simulation. The FIBF algorithm presented at mmWave frequency band in [14] is used to obtain the spatial channel profiles. However, due to the lack of available VAA measurement data in sub-THz bands, the application of the FIBF algorithm at sub-THz does not exist. For compensation of the high PL at mmWave and sub-THz bands, it is important to use high-gain directive antennas in order to increase the dynamic range. Therefore, the FIBF algorithm is generalized to function for UCA composed by any type of antenna element. The algorithm is applicable for a wide range of propagation scenarios - FF and NF, wideband and narrowband scenarios and for both omni-VAA and Dir-VAA configurations. The reader can obtain detailed information about the generalization of the FIBF algorithm by following equations (7)-(22) in [10].

Analysis of the FIBF algorithm applied for a UCA composed of different antennas is performed via simulation. The antennas used in the simulation are an omnidirectional antenna with 0 dBi gain, a corrugated horn antenna with a gain of 9.5 dBi and a HPBW of 54°, and a SGH antenna with a gain of 20.5 dBi and 16° HPBW. The three antennas are compared by using the extended FIBF algorithm and the results are presented in Figure 23.

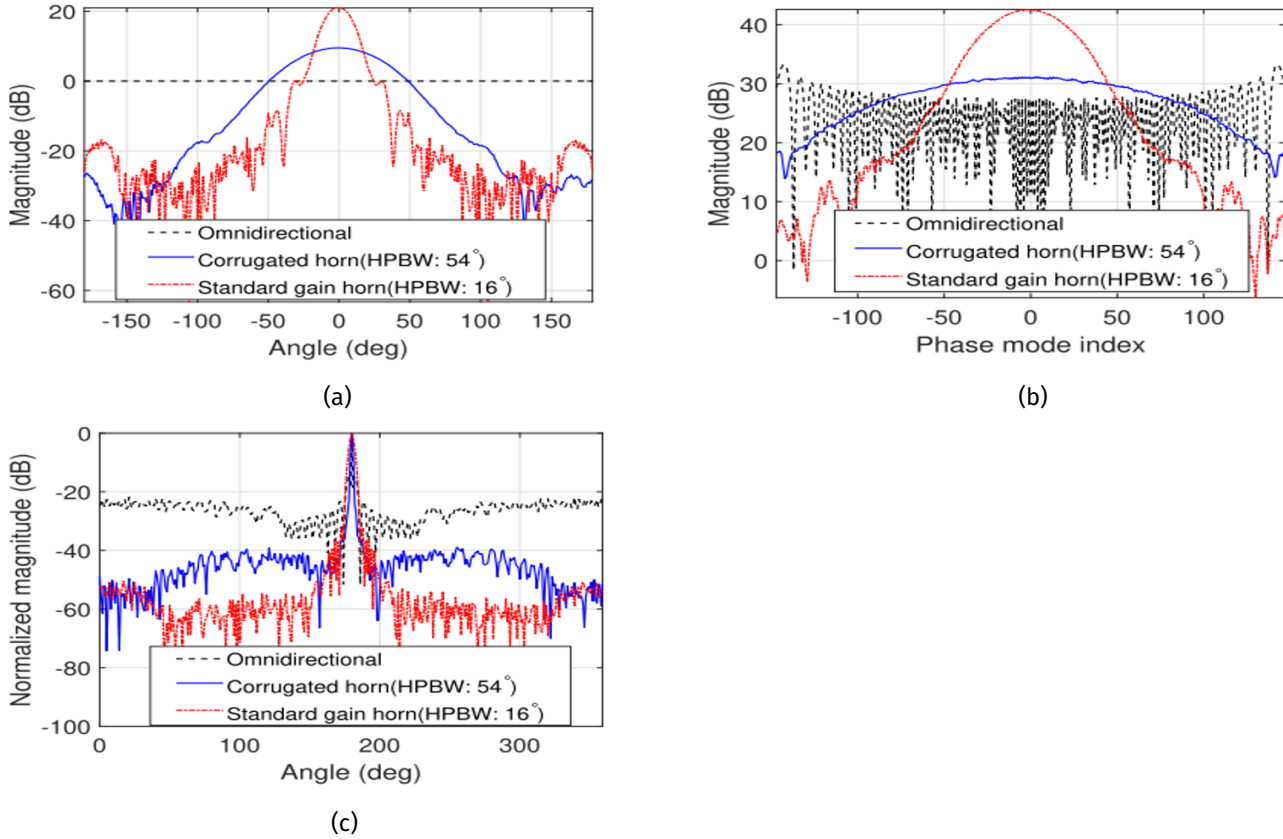


Figure 23: Comparison of the array manifold in the phase mode domain for the UCAs composed of elements with different directivity a) The element patterns b) The array manifolds in the phase mode domain c) The array beam patterns

It is found that a UCA composed of more directional elements (as illustrated in Figure 23a) leads to a narrower window in the phase mode (as presented in Figure 23b). When performing the extended FIBF algorithm, the window introduces an amplitude tapering effect in the phase domain. Similar to the amplitude tapering effect in the spatial domain, sidelobe suppression, and main beam broadening is introduced to the array beam pattern as it is shown in Figure 23c. Selection of the phase modes with dominant magnitudes (as shown in Figure 23b) is justifiably due to the windowing effect in the phase mode domain, resulting in a limited number of phase modes. Therefore, for a UCA consisted of more directional elements, a smaller mode number is selected owing to the fewer dominant phase modes. The numerical results have confirmed that the proposed generalized FIBF algorithm functions well for UCA made of both omnidirectional and directive antennas.

2.2.3.4 Back-to-back measurement validation. Impact of the phase instability on the VAA performance. The instability of the phase in the VNA-based channel sounder with an employed RoF scheme is a key problem for the VAA scheme at the sub-THz band. A back-to-back measurement of the phase-compensated channel sounder is presented, as the phase instability and its impact on the VAA scheme are illustrated. A photo of the back-to-back measurements is presented in Figure 24.

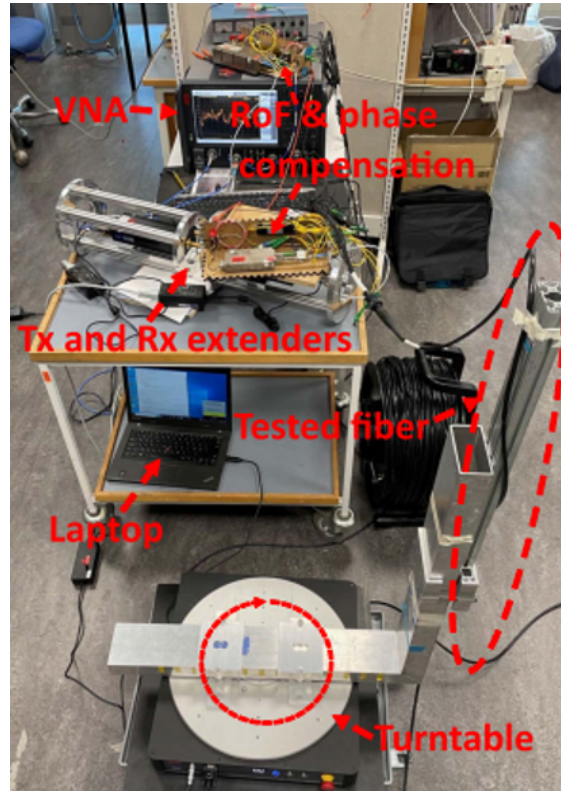
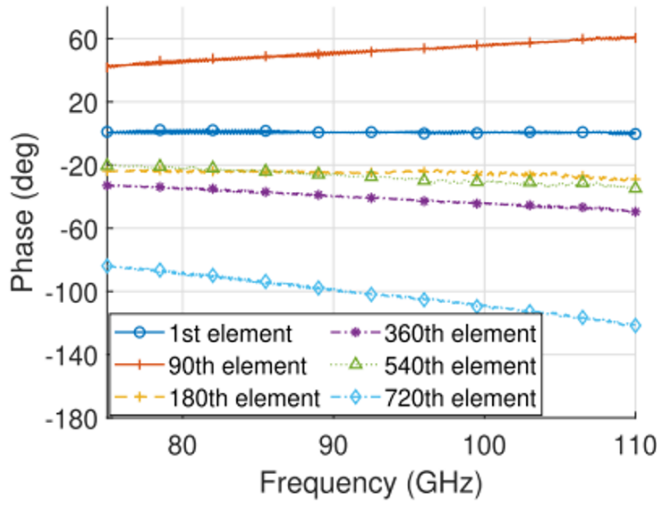
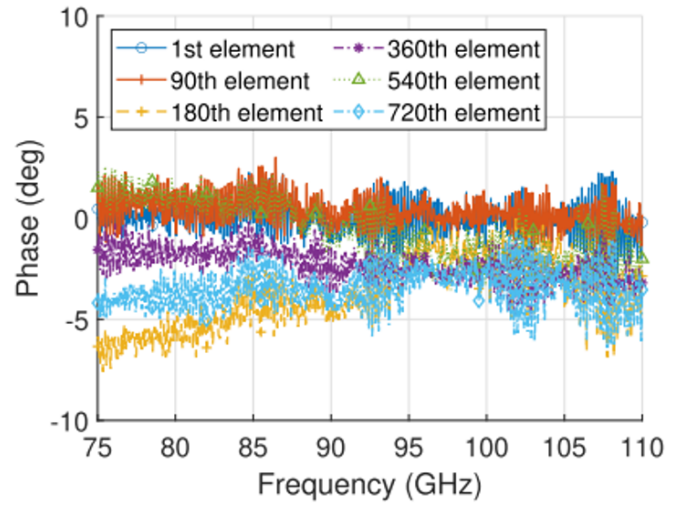


Figure 24: Photo of the back-to-back measurements using the turntable to mimic the mechanical bending of the fiber

The forward link of this channel sounder is similar to the one in the RoF structure in the conventional RoF-enabled VNA-based channel sounders [15], [16], [17], [18], [19]. The VNA sweeps the frequency range 75–110 GHz with 1001 frequency points and 500 Hz IFBW. The Tx and Rx antennas are not available. Therefore, the Tx and Rx frequency extenders are connected directly in the back-to-back measurements. To mimic the bending of the fiber during the channel measurement using the VAA or DSS scheme, the fiber is mounted on the turntable. The turntable rotates in an azimuth range of $[0^\circ, 359.5^\circ]$ with a step of 0.5° , which corresponds to 720 virtual array elements. The duration of the back-to back measurement was 2 hours, which was close to the time of the actual channel measurements. Before the measurements, for the forward and feedback links, a calibration procedure performing the normalization in the VNA setting the system response to 1 for all swept frequency points is performed. Therefore, the amplitude and the phase change in the channel sounding system can be measured directly.



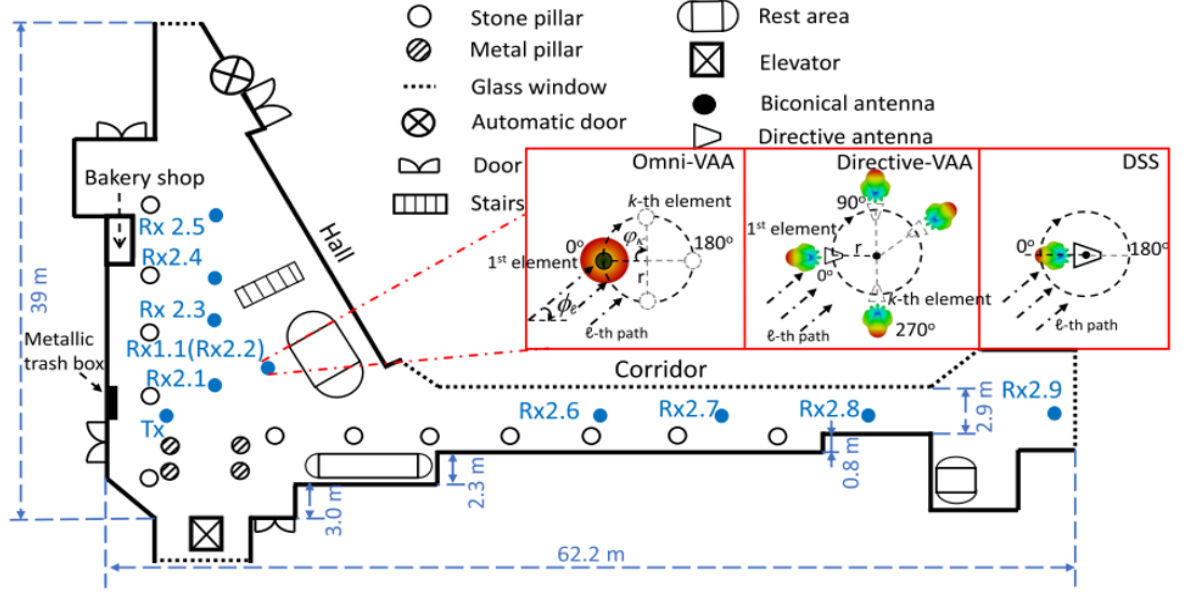
(a)



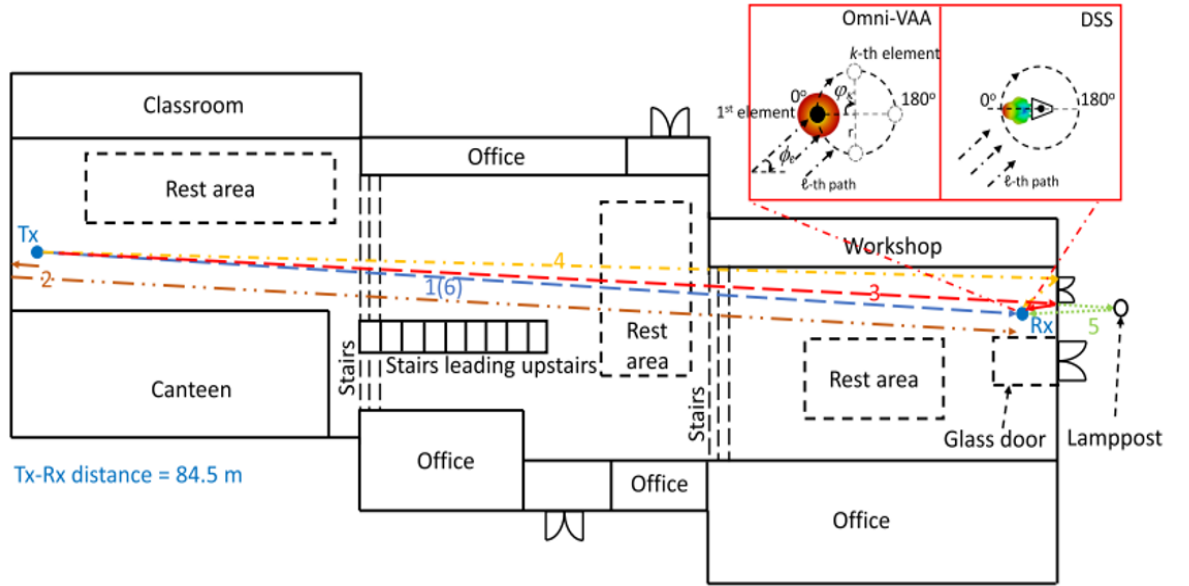
(b)

Figure 25: Phase performance of the phase-compensated channel sounder in back-to-back connection a) Forward link b) Compensated phase

The phase measurements of the channel sounder for a few spatial locations are presented in Figure 25a. The cable bending during the rotation causes variation in the phase from -121.6° to 60.9° . The feedback response has also been measured in the back-to-back measurements. Therefore, the compensated phase can be calculated in the post-processing step by using (6) in [10]. After the compensation is applied, the phase variation is maintained within $\pm 5^\circ$, as it is observed in Figure 25b, which demonstrates clearly that the proposed phase compensation scheme works effectively.



(a)



(b)

Figure 26: Measurement scenario of the VAA at 100 GHz a) NF and UWB validation b) Long-range validation

2.2.3.5 Channel measurement validation Omni-VAA-based channel measurements are carried out to validate the proposed channel sounder and algorithm at sub-THz bands. The scenario for the NF measurements is illustrated in Figure 26a. It contains a large hall and a long corridor. The photo of the scenario is presented in Figure 27. Detailed information about the measurement configuration is presented in Table IV.

TABLE IV
MEASUREMENT CONFIGURATION

Meas.	Near-field			Long-range		UWB
type	Omni-VAA	Dir-VAA	DSS	Omni-VAA	DSS	Omni-VAA
VNA settings						
Frequency range [GHz]	99-101			99-110		
Bandwidth [GHz]	2			11		
Frequency point	1001			7701		
IFBW [Hz]	500					
Transmitted power [dBm]	10					
Antenna settings						
Tx antenna type	Omnidirectional					
Tx antenna gain [dBi]	4.5					
Rx antenna type	Omnidirectional	SGH		Omnidirectional	SGH	Omnidirectional
Rx antenna gain [dBi]	4.5	20		4.5	20	4.5
Rx antenna HPBW [°]	360	16		360	16	360
Virtual UCA settings						
Radius of the UCA [cm]	6.7	6.7	0	6.7	0	6.7
Rotation step [°]	1					
Number of elements	360					
Scenario settings						
Antenna height [m]	1.3			2.1		1.3
Tx-Rx distance [m]	7.3			84.5		3-58

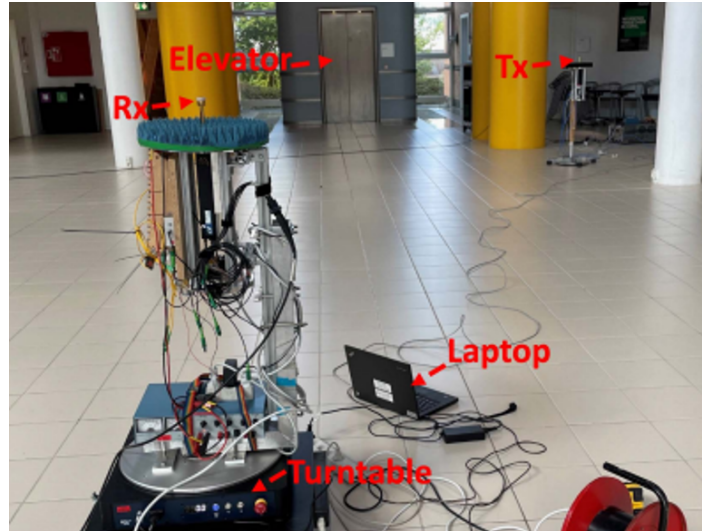


Figure 27: Photo of the measurement scenario in the NF case (i.e., Tx-Rx 1.1)

The size of the area is 62.2 m × 42 m. On one side of the corridor there is a window with a metallic structure, while on the other side there are seven stone pillars. In the NF case (i.e., Tx-Rx1.1), the Tx-Rx distance is chosen to be 7.3 m, which is much smaller than the FF distance (see eq. (5.15) in Appendix). The VNA sweeps in the frequency range from 99 to 101 GHz with 1001 frequency points, and the IFBW is set to 500 Hz.

The delay resolution is 0.5 ns (corresponding to the distance resolution of 0.15 m) and the maximum detectable distance is 150 m. An omnidirectional antenna with a gain of 4.5 dBi [20] is used as the Tx and Rx antenna to validate the Omni-VAA. The height of the Tx and Rx antennas is 1.25 m. The turntable is rotated in the horizontal plane within a range of $[0^\circ, 359^\circ]$ with a step of 1° , which forms a virtual UCA with a radius of $R = 6.7$ cm. Additionally, the DSS-based measurements conducted in the same Tx and Rx locations are performed to serve as reference. In the DSS measurements, a SGH antenna with an antenna gain of 20 dBi and an HPBW of 16° [21] is located at the center of the turntable as the Rx antenna, while the position of the Tx antenna is kept unchanged. Prior to the measurements, the antennas are removed and the Tx and Rx waveguides are connected to perform the back-to-back calibration, i.e., normalization procedure to calibrate the system response. The measurement configurations for the NF measurements are listed in Table IV.

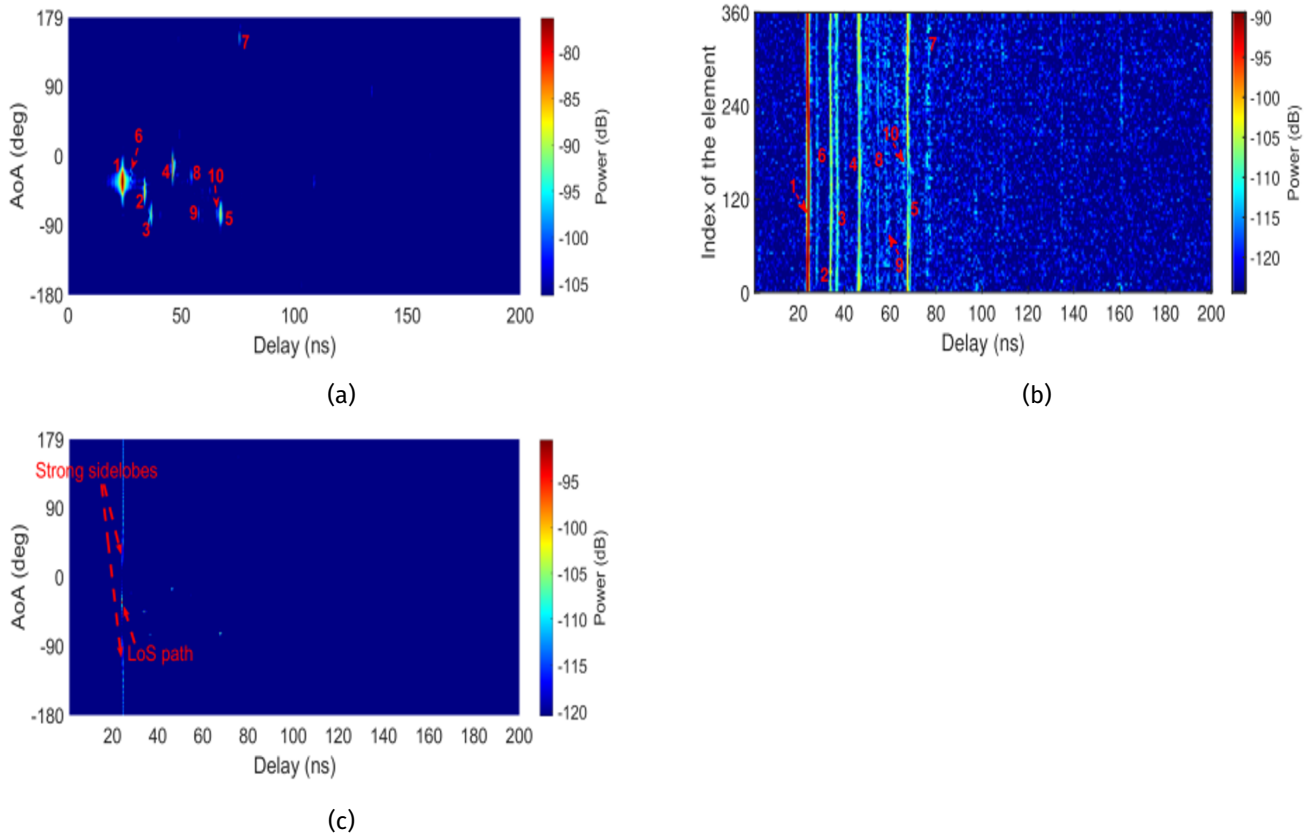


Figure 28: The measurement results in the NF case a) PADP with the DSS b) Recorded CIR with Omni-VAA over array elements c) PADP with Omni-VAA with the FIBF method

Figure 28a shows the PADP for the DSS scheme in the NF case. Ten distinct paths can be identified. Although the antenna pattern is embedded in the DSS results, the paths can be identified clearly when looking at angle and delay domain. Figure 28b and Figure 28c show the recorded CIR with Omni-VAA and the PADP result with Omni-VAA using the FIBF algorithm, respectively. From the recorded CIR it was also found 10 paths. However, the use of the omnidirectional antenna at the Rx led to a lower dynamic range compared to the PADP with the DSS (as seen in Figure 28b). After the FIBF algorithm is applied, a high angular resolution is obtained, though strong sidelobes can also be observed, as one would expect. The LoS path with an AoA of -33° and a delay of 24 ns (which corresponds to the LoS propagation

distance of 7.2 m) is estimated in the Tx-Rx 1 case, which matches the physical distance between the Tx and Rx. The calculated power of the LoS path is -90.5 dB, which is close to the calculated FSPL (89.7 dB) (see eq. (5.13) in Appendix) for distance $d_{LoS} = 7.3$ m. Furthermore, an improvement in the Signal to Noise Ratio (SNR) of the PADP after the FIBF compared to the raw CIR (presented in Figure 28b and in Figure 28c) of 20.5 dB can be observed. The theoretical value for the array gain is $10\log_{10}(K) = 25.6$ dB. The measured array gain is a bit lower than the theoretical one owing to the different non-idealities in the measurement system.

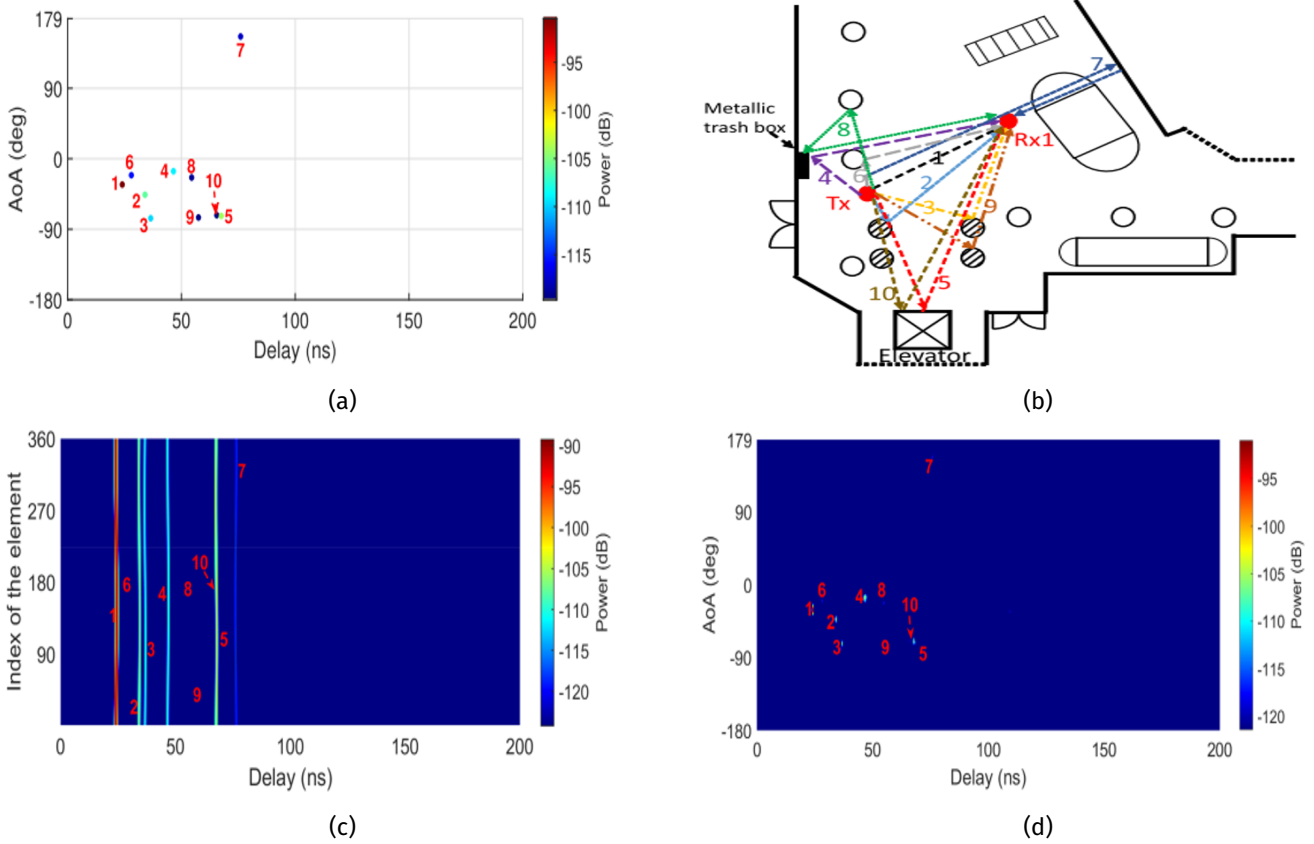


Figure 29: The estimated results in the NF case (i.e., Tx-Rx 1.1) a) Estimated path results b) The relation of the detected MPC trajectory to the room geometry c) Synthesized CIR using estimated results d) The PADP results with Dir-VAA after the FIBF

The FIBF with the SIC procedure is applied to the measured data. A signal threshold is set to be 10 dB higher than the noise floor. Note that for the long-range and UWB channel validation, the signal thresholds are the same as that in this NF case. Figure 29a shows the estimation results using the FIBF algorithm with the SIC. The detected ten dominant paths are mainly concentrated in the AoA range of $[-90^\circ, 0^\circ]$. Figure 29b illustrates the paths trajectory. Path 2, 3, 6, and 9 are found to be the reflections from the pillars. Paths 5 and 10 are due to the reflections from the elevator. Path 7 is observed to be the reflection from the back wall of the Rx, while paths 4 and 8 are respectively the first-order and second-order reflections from the metallic trash box. Both the propagation distance and angle of the estimated paths match the geometry of the hall. The estimation results in Figure 29a are compared with the DSS results in Figure 28a. A good agreement between the estimation results and the DSS results is found. Figure 29c presents the synthesized CIR on the virtual UCA elements using the estimated paths. It is compared with the recorded CIR on the virtual UCA

elements in Figure 28b and it can be concluded that most specular paths are detected accurately.

Dir-VAA-based channel measurements are also carried out in the NF case (i.e., Tx-Rx1.1) using the same Tx-Rx deployment and measurement configurations. Comparing the DSS with Dir-VAA schemes, the measurement system and antenna configurations are the same with only one difference that the employed directive antenna is centered on the turntable for the DSS case (according to the definition of the DSS scheme), while for the Dir-VAA case an off-set with a radius of 6.7 cm (with respect to the center of the turntable) is used. Comparing the Dir-VAA and the Omni-VAA, the only difference is the used antenna, i.e., the omnidirectional antenna is used as the array element in the Omni-VAA, while the directive antenna is utilized as the array element in Dir-VAA. Figure 29d presents the PADP with the Dir-VAA after the FIBF. The LoS power after the FIBF is found to be -90.9 dB, which is close enough to the calculated FSPL value. Compared with the DSS PADP presented in Figure 28a, the MPCs are distributed in the same locations. Moreover, the angular resolution is significantly improved by the FIBF algorithm (the main beamwidths of the PADP with Dir-VAA after the FIBF and with the DSS are respectively 3° and 16°). The improvement in the SNR of the Dir-VAA is 15.0 dB, which is less than that of the Omni-VAA. The reason is that less effective array elements in Dir-VAA are used compared to those in Omni-VAA. The Dir-VAA has a high element gain (20 dBi at 100 GHz) compared to 4.5 dBi at 100 GHz for Omni-VAA. The latter can be used to increase the dynamic range of the channel sounder to support long-range channel measurements.

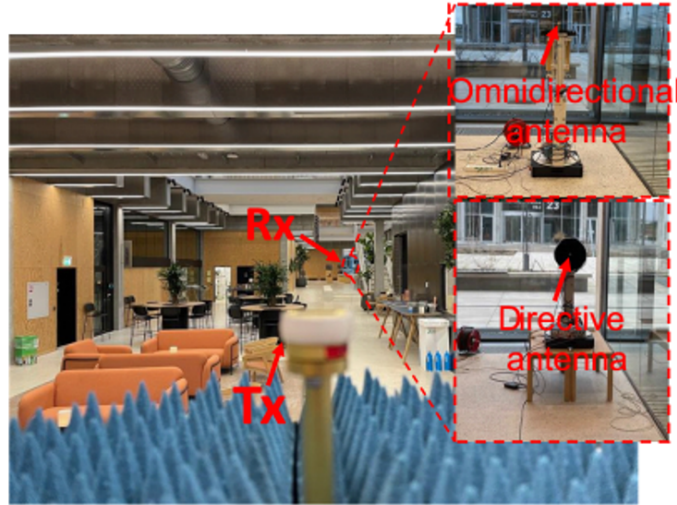


Figure 30: Photo of the measurement scenario in the long-range case)

Channel measurements are also performed to confirm that the proposed sounder can be used for long-range channel measurement. Although in the state-of-the-art long-range measurements directive antennas to improve the system dynamic range are generally used [15], [22], in the current measurements, omnidirectional antennas are intentionally utilized to demonstrate the capability of the developed channel sounder. The long-range validation measurements are performed on the ground floor at the Innovation Building at Aalborg University, as shown in Figure 31c. The measurement scenario is a typical hall scenario with a size of $94 \text{ m} \times 30 \text{ m}$. The frequency range is set to be 99–110 GHz with a bandwidth of 11 GHz and the number of frequency points of 7701 resulting in a delay (distance) resolution of 0.09 ns (0.03 m) and a maximum measurable distance of 210 m, respectively. The IFBW is 500 Hz and transmitted power is 10 dBm. Two identical omnidirectional antennas [20] are used for the Tx and Rx antennas. The distance between Tx and Rx is 84.5 m. Because of the available stairs, there is a height difference of 0.72 m between the Tx and the Rx.

Therefore, to align the antennas, the heights of the Tx and Rx antennas are respectively 2.05 m and 1.32 m. As it was for the NF case, DSS measurements are also carried out for a reference. Figure 30 and Table IV present respectively the photo of the long-range measurement scenario and the list with measurement configurations.

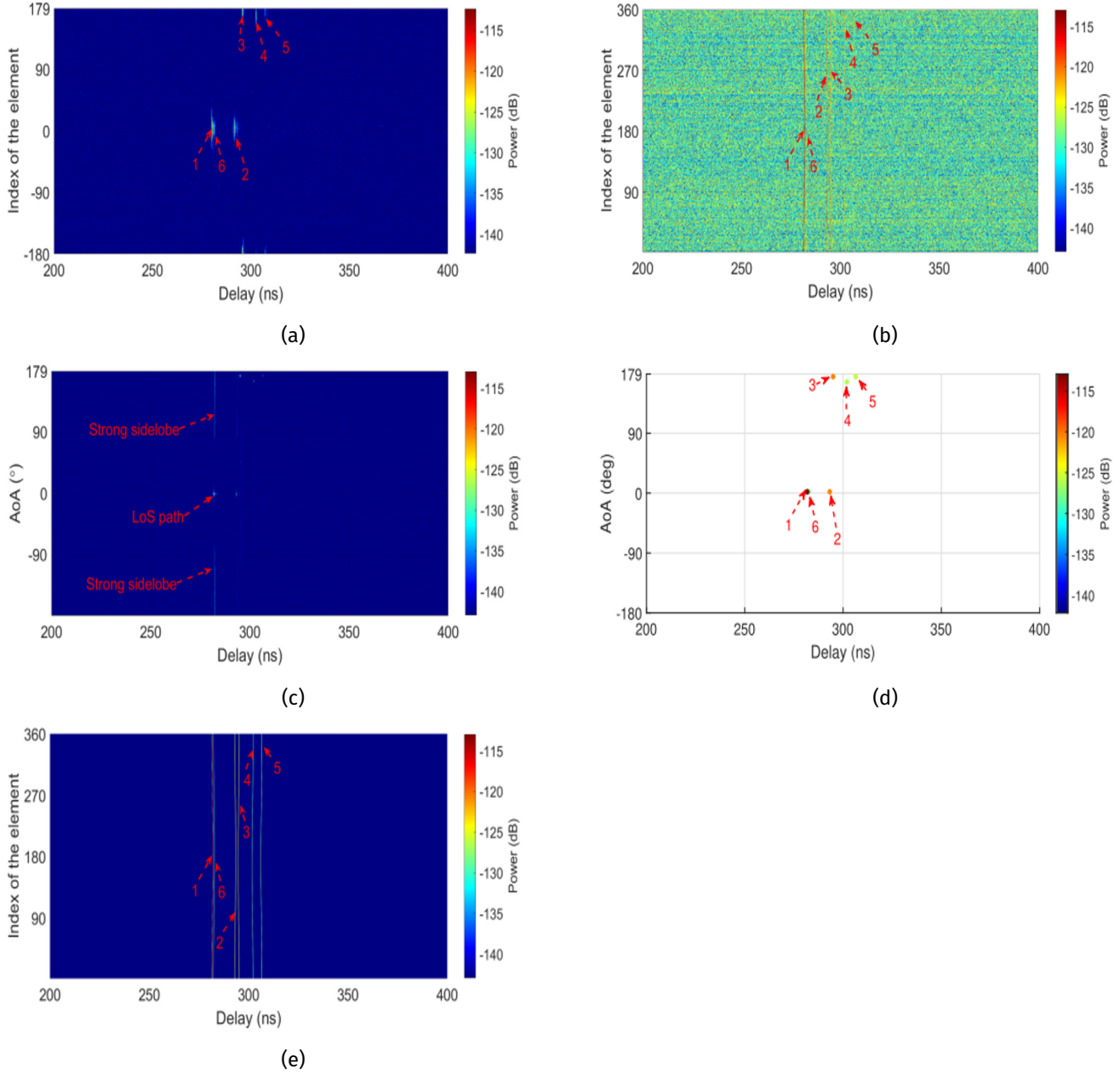


Figure 31: The measurement results in the long-range case a) PADP with the DSS b) Recorded CIR with Omni-VAA c) PADP with Omni-VAA after the FIBF d) Estimated path results e) Synthesized CIR using estimated results

Figure 31a shows the PADP result with the DSS in the long-range case. Six paths can be identified from the PADP plot. However, it is difficult to detect the paths from the recorded CIRs over array elements (presented in Figure 31b) owing to the low dynamic range of the Omni-VAA scheme in the long-range case. A high angular resolution can be observed after the FIBF algorithm is applied, as visible in the PADP after the FIBF in Figure 31c. The LoS path has an

AoA of 2° and a delay of 281.7 ns (which corresponds to the LoS propagation distance of 84.5 m), which is equal to the deployment distance between the Tx and Rx. The LoS power is -112.9 dB, while the theoretically calculated FSPL value is 111.4 dB. The small difference may be dictated by error in the alignment between the Tx and Rx antennas for such a long distance. Moreover, a strong sidelobe can be observed in Figure 31c, as it could be expected for the FIBF algorithm. A SNR improvement of the PADP after the FIBF in Figure 31c compared to the raw CIRs in Figure 31b of 16.0 dB is found. Figure 31d and Figure 31e show respectively the estimated paths and the synthesized CIR on the virtual UCA elements after using the FIBF with the SIC. Owing to the high PL and the low antenna gain of the used omnidirectional antennas, only 6 paths are detected in the measurement results using the FIBF with the SIC. The trajectory of the dominant paths is shown in Figure 31c. Path 2 is found to be the reflection from the back wall of the Tx, while paths 3 and 4 are reflections from the metallic structure of the back wall at the Rx side. Path 5 is the reflection from the outdoor lamppost, while path 6 is found to be the reflection from the wooden furniture in the middle rest area. Moreover, when comparing the reconstructed CIR in Figure 31e with the recorded CIRs over virtual array elements, a good agreement can be observed, which is a proof that the dominant paths in these two measurements fit well, validating the measurement results using the VAA concept.

In the subsection, only few explanations will be given about the performed UWB channel measurements and characterization. However, the reader can refer to Fig. 15 - Fig. 17 in [10]. The measurement scenario and the Tx and Rx deployments are the same as in the NF case and is shown in Figure 31b. The Tx is situated close to the wall to simulate a base station (BS). Nine Rx locations (i.e., Rx 2.1-Rx 2.9) with the link distance ranging from 4–58 m are used. The antenna heights of the Tx and Rx are 1.25 m. The measurement settings are the same as those in the long-range measurements. Therefore, $360 \times 9 = 3240$ CFRs were obtained in total (number of UCA elements \times number of measurement locations). Each measurement took approximately 4 hours and the entire measurement took around 40 hours. The detailed measurement specifications are listed in Table IV. The FIBF with the SIC is used to extract the parameters (amplitude, delay, and AoA) of the MPCs for each measurement location, and then the channel characteristics are estimated using those estimated channel parameters. The PL is calculated by using (5.14) in Appendix. Fig. 15 in [10] presents the measured PL compared with the fitted model. A good agreement between the fitted PL model and the FSPL model is observed. The delay spread is shown in Fig. 16(a) in [10]. The delay spreads is in the range of [5.67, 47.61] ns. Fig. 16(b) in [10] presents the AoA spread result. The angular spreads vary from 15.63° to 72.11° in this scenario. The PASSs with the estimated results compared with the mean AoA $\hat{\phi}_\ell$ in the Tx-Rx2.2 and Tx-Rx2.9 are shown in Fig. 17 in [10]. It was found that the MPCs in Tx-Rx2.2 are concentrated on the mean angle leading to a low AoA spread. In the Tx-Rx2.9 case, the AoAs of the MPCs are in the range $[-123, 180]^\circ$ defining a high angular spread. The k-factor is found to decrease with the increase of the distance. These findings are expected and can be explained by the fact that with increasing of the distance, the LoS power decreases and the power levels of the MPCs becomes comparable to the LoS power (it can be also observed from the comparison of the power of the MPCs between the Tx-Rx2.2 and Tx-Rx2.9 in Fig. 17 in [10]).

2.2.3.6 Conclusion This section presented the design, implementation, and validation of a phase-compensated channel sounder, which is able to support the VAA scheme and long-range measurements at W bands (75–110 GHz). The phase instability is a critical problem at sub-THz bands making the existing channel sounder solutions inappropriate for applying advanced array signal processing algorithms to extract the channel path parameters. It was proved by simulation that the VAA scheme cannot be directly used in the conventional sub-THz channel sounder, because the

unstable phase performance may cause BF loss up to 3.1 dB. Therefore, a phase compensation scheme is proposed to address effectively this issue and a phase variation up to $\pm 5^\circ$ is achieved in the back-to-back connection in the W-band. Virtual UCA-based channel measurements in the NF (with an LoS distance of 7.3 m) and long-range (with an LoS distance of 84.5 m) cases were carried out at 100 GHz to validate the proposed channel sounder. Moreover, a high-resolution channel parameter estimator (i.e. FIBF with the SIC) was applied to extract the MPC parameters. The purpose of the NF measurements was to validate the generalized high-resolution channel parameter estimator, while in the long-range case, it was aimed to illustrate the capability of the proposed channel sounder with a large dynamic range via intentionally employed omnidirectional antennas on both the Tx and Rx sides. In the long-range cases, six specular paths were found including only the LoS path and only the first-order reflections, while in the NF case, ten paths were identified including the LoS path, the first-order and second-order reflections.

Both measurement results demonstrated the sparse property of the W-band channel. The measurements using the conventional DSS scheme were used as a reference to validate the estimated path parameters. Compared to the DSS results, consistent path parameters in terms of path power, angle, and delay were obtained by using the FIBF with the SIC for both cases. These extracted path parameters were utilized to reconstruct the CIRs over the UCA elements. The comparison between the reconstructed CIR and the recorded CIR demonstrates a good level of agreement. Moreover, the FIBF algorithm was also extended to a generic algorithm, which is able to function for NF/FF, narrowband/wideband propagation scenarios using Omni-VAA and Dir-VAA schemes. Omni-VAA-based UWB measurements in the frequency range from 99 to 110 GHz were carried out in a hall scenario at 9 Rx locations covering the link distances from 3 to 58 m. By applying the FIBF with the SIC algorithm, the power, delay, and AoA of the MPCs were extracted from the obtained measurement results. Additionally, the basic channel characteristics, such as PL, delay spread, angular spread, and k-factor, were presented and analyzed.

2.2.4 Large virtual antenna array-based empirical channel characterization for sub-THz indoor hall scenarios Despite significant efforts have been dedicated to sub-THz channel measurements and modeling, important aspects remain insufficiently investigated in the literature. One crucial aspect is that the existing channel measurements and models have not covered the entire sub-THz bands for different scenarios. Another important point is that the recent measurements are mainly using the DSS scheme, which provide low spatial resolution and high sidelobes. Therefore, the multipath parameters estimated from the PADPs derived using the DSS method will be impacted, leading to unprecise modeling and characterization results. Third crucial aspect is that many previous studies have not explored the channel spatial consistency regarding MPC trajectories at sub-THz frequencies. The latter is of an significant importance for evaluation the performance of 6th Generation (6G) systems, particularly in the aspect of the beam management.

This section, based on the work [23], presents the channel measurements and characterization of the sub-THz channel measurement campaign conducted in an indoor hall scenario at sub-THz bands. The channel measurement campaign was carried out with 55 Tx-Rx deployment locations. The Tx-Rx distance was in range [3, 58] m and the measured bandwidth (99-101) GHz. The used long-range channel sounder includes a phase-compensated scheme. The MPCs parameters are extracted by using a channel parameter estimation algorithm. Furthermore, the MPCs trajectories in two of the routes are traced by the use of a MPCs trajectory tracking algorithm. The proposed 100 GHz channel model for the indoor scenario was also compared with the existing channel models.

A RoF-enabled phase-compensated VNA-based channel sounder (see Figure 22 in section 2.3.3.1), which can sup-

port long-range measurements, is used in these measurements. The operation frequency range in these measurements is (99, 101) GHz with a centered frequency of 100 GHz and a bandwidth of 2 GHz. The transmitted power is set to 10 dBm and the IFBW is 500 Hz, securing a high dynamic range. The number of frequency points is 1001, which corresponds to a maximum detectable distance of 150 m. An identical vertically polarized omnidirectional antennas are used at the Tx and Rx. The measurements were carried out in an indoor scenario, as illustrated in Figure 32.

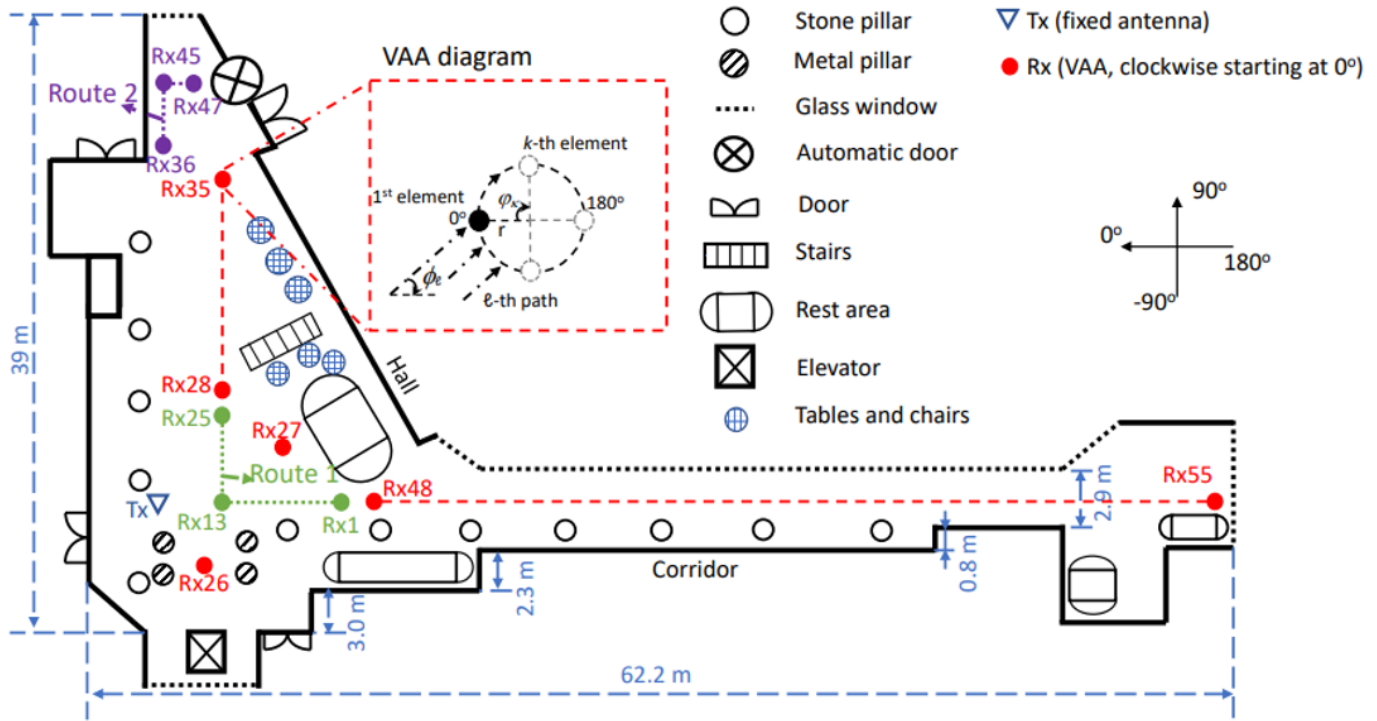
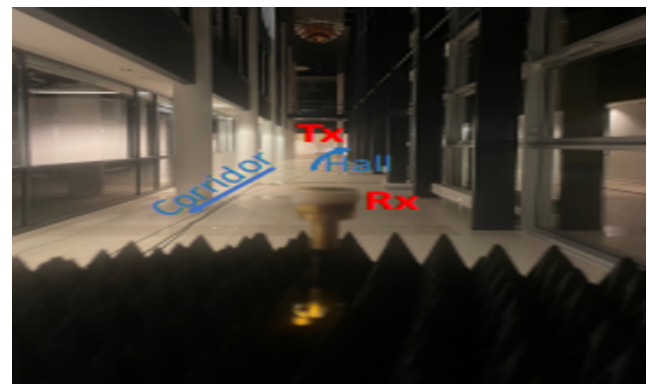


Figure 32: Illustration of the measurement setup and the placement of the Tx and Rx

The measurement scenario is composed of an irregularly shaped hall and a corridor with a size of 62.2 m × 39 m. As presented in the scenario pictures in Figure 33, there are many metallic and stone pillars.



(a)



(b)

Figure 33: Photos of the measurement scenario at 100 GHz a) Rx 36 b) Rx 51

Several sofas, metallic tables, a metal-structured stair and an automatic door exist also in the hall. The long

and narrow corridor (33 m × 2.9 m in size) is connected to the hall. The Tx was position in vicinity to the wall to mimic a BS, while the Rx was situated in 55 locations with the Tx-Rx distance in the range [3, 58] m. Two specific "L"-shape routes, i.e. Route 1 and Route 2, were created by Rx 1-Rx 25 (i.e. 25 Rx locations) and Rx 36-Rx 47 (i.e. 12 Rx locations), respectively. In Route 1 and 2, the distance between the neighboring Rx VAA centers is 0.6 m. Moreover, positions Rx 26 – 35 and 48 – 55 were introduced to complement the profound channel characterization. The height of Tx and Rx was 1.3 m. The Tx was at a fixed location, while the Rx formed a UCA. Therefore, it was mounted on a turntable and was rotated in the azimuth in the range $[0, 359]^\circ$ with a radius of 6.7 cm and a rotation step of 1° . The measurement time for each Rx location was approximately 1.5 hours. Totally, $55 \times 360 = 19800$ CFRs are obtained in the measurements. Prior to the measurements, a back-to-back calibration procedure was executed in order to eliminate the influence of the system response. The measurement configurations parameters are listed in Table V.

TABLE V
MEASUREMENT CONFIGURATION

Parameter	Value
Frequency range	99 – 101GHz
Bandwidth	2 GHz
Frequency point	1001
IFBW	500 Hz
Transmitted power	10 dBm
Tx & Rx antenna type	Omnidirectional
Tx antenna gain	4.5 dBi
UCA radius	6.7 cm(22.3λ)
Rotation step	1°
Number of elements	360
Antenna height	1.3 m
Tx-Rx distance	3 – 58 m

In the current work, a BF-based channel parameter estimation algorithm, i.e., FIBF algorithm [14] with added SIC procedure is used to obtain the spatial channel profiles from the measurement data. The need for using the SIC procedure is that the FIBF algorithm can produce significant sidelobes, which will be identified as paths (i.e. fake paths) and leading to a degradation in the channel estimation performance. The combination FIBF with the SIC is a generic algorithm solution useful for various propagation scenarios, including both FF and NF scenarios, wideband and narrowband conditions as well. It is also applicable for Omni-VAA or Dir-VAA. Figure 34 shows the exemplary results for position Rx 14.

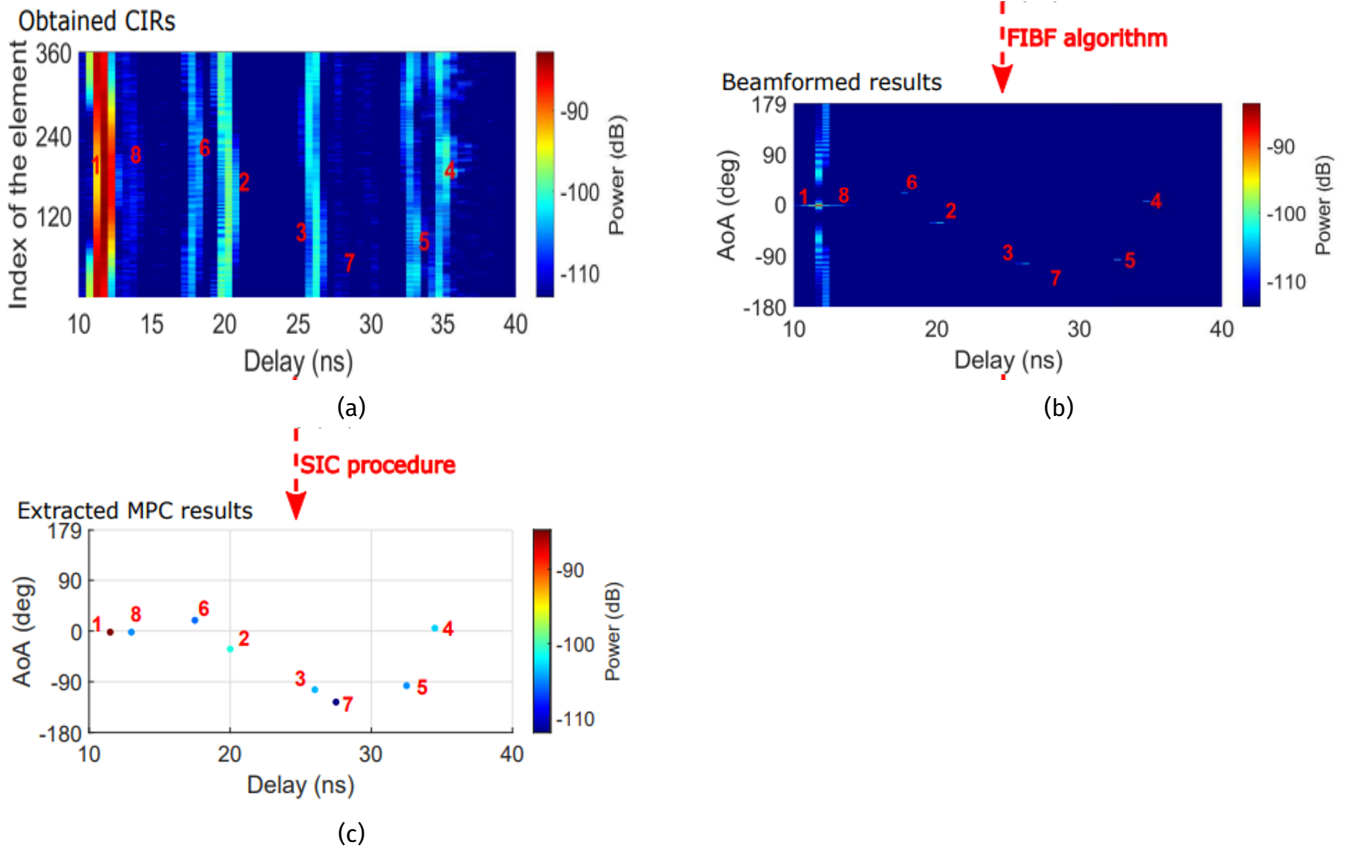
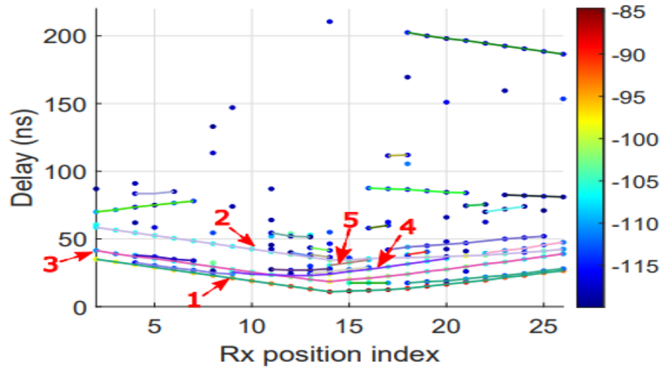


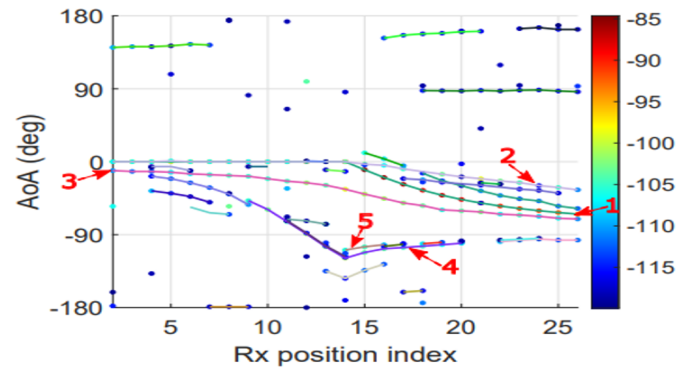
Figure 34: Exemplary results from the measurements and channel parameter estimation (Rx 14) a) CIR b) Beamformed results with FIBF algorithm and c) Extracted MPC results after applied SIC procedure

The CIRs for all VAA elements (Figure 34a) are directly estimated from the measurement results by using the Discrete Fourier transform (DFT). Afterwards, the FIBF algorithm is applied to obtain the beamformed results (Figure 34b). Then, the SIC procedure is used to extract the MPC parameter results (Figure 34c). A dynamic range of 30 dB is used to estimate the MPCs. As it is visible from the figure, eight MPCs were detected.

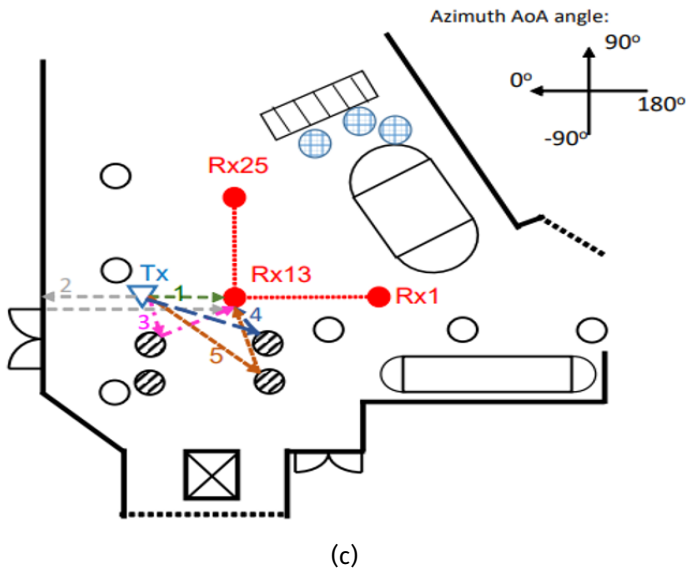
The MPC trajectory tracking algorithm is based on estimation of the multipath component distance MCD [24]. MCD is a measure for scaling the separation of the detected MPCs, including the estimated MPCs parameters (e.g. path gain, delay and angles). The reader can refer to equations (5)-(11) in [23]. The estimated MCD between the MPCs is compared to a predefined threshold Z . If the specific MCD is less than Z , those two MPCs are considered to belong to the same trajectory. The tracking results for both routes are presented for the delay domain in Figure 35a and Figure 36a and for the azimuth AoA domain in Figure 35b and Figure 36b, respectively.



(a)



(b)



(c)

Figure 35: Tracked MPC trajectories compared with estimated MPC results in Route 1 a) Delay domain b) Azimuth AoA domain c) Main MPC trajectories compared with the hall geometry (for location Rx 13)

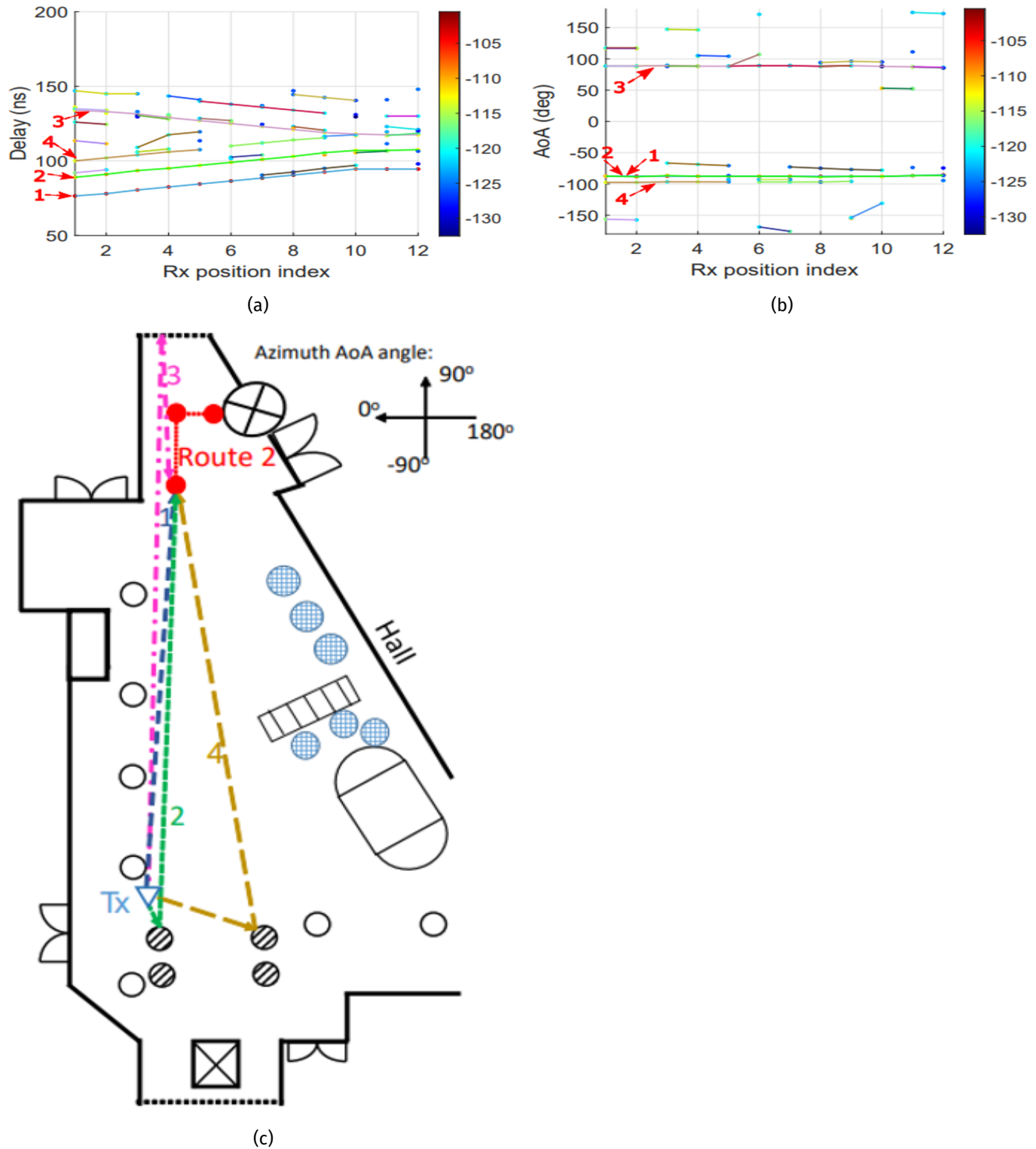


Figure 36: Tracked MPC trajectories compared with estimated MPC results in Route 2 a) Delay domain b) Azimuth AoA domain c) Main MPC trajectories compared with the hall geometry (for location Rx 36).

The total number of the detected MPC trajectories for Route 1 and 2 are respectively 30 and 26. For simplicity, the number of the MPCs presented in the figures is limited to 12. For Route 1, the dominant MPC trajectories were

identified, and the relation of the trajectories to the geometric attributes of the hall is presented in Figure 35c (Rx 13 is shown as an example). The dominant MPC trajectories are chosen based on the power level of the trajectory. The LoS is Trajectory 1 and Trajectory 2 is the reflection from the back (for the Tx) wall. Trajectories 3, 4, and 5 are the reflections from the metal pillars. Owing to the blockage of the front pillar, only 3 Rx locations received the power of the MPCs in Trajectory 5. For Route 2, four dominant MPC trajectories were distinguished, and the relationship between the trajectories and the hall geometry is presented in Figure 35c (Rx 36 is illustrated as an example). Trajectory 1 is the LoS path, and Trajectory 2 and 4 are the reflections from the metal pillar. Trajectory 3 is found to be the reflection from the metallic structure at the rear window of the Rx. It can be also observed that the azimuth AoA of the trajectory is mainly concentrated in the azimuth AoA region facing Tx, that is $[-100, -80]^\circ$, and the azimuth AoA region facing away from Tx, that is $[80, 120]^\circ$. Comparing the propagation delay and azimuth AoA of the estimated paths with the geometric characteristics of the hall, it is concluded that the MPC trajectories matched good with the geometry.

Equation (5.16) in Appendix is used to estimate the alpha-beta (AB) PL model. The PL estimated from the measurement data and the calculated from the fitted model are presented in Figure 37.

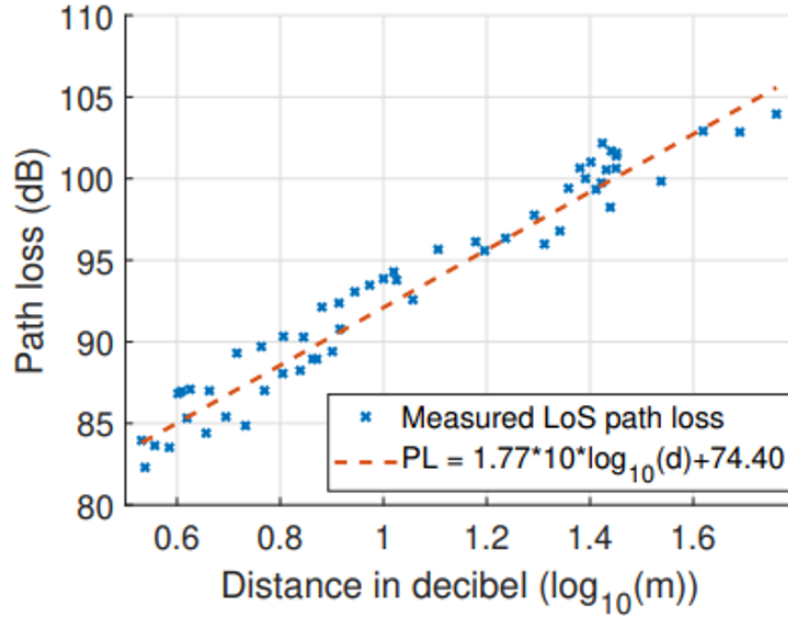


Figure 37: Path loss (PL) as observed in the measurements and the fitted PL model

It is worth it to note that the estimated results had the antenna gain not included in PL calculation. The measured PL matches good with the PL model of $PL = 1.7710\log_{10}(d) + 74.40\text{dB}$ with the determination factor $R^{abc} = 0.95$. The root-mean-square (RMS) delay spread is channel parameter, which is used to describe the delay dispersion in the channel. Eq. 5.10 in Appendix defines the relation for estimation of the delay spread. The azimuth AoA spread is a parameter used to characterize the azimuth AoA span in the channel (defined in eq. (5.11) in [23]). Figure 38 shows the estimated results for the delay spread and for the angular spread.

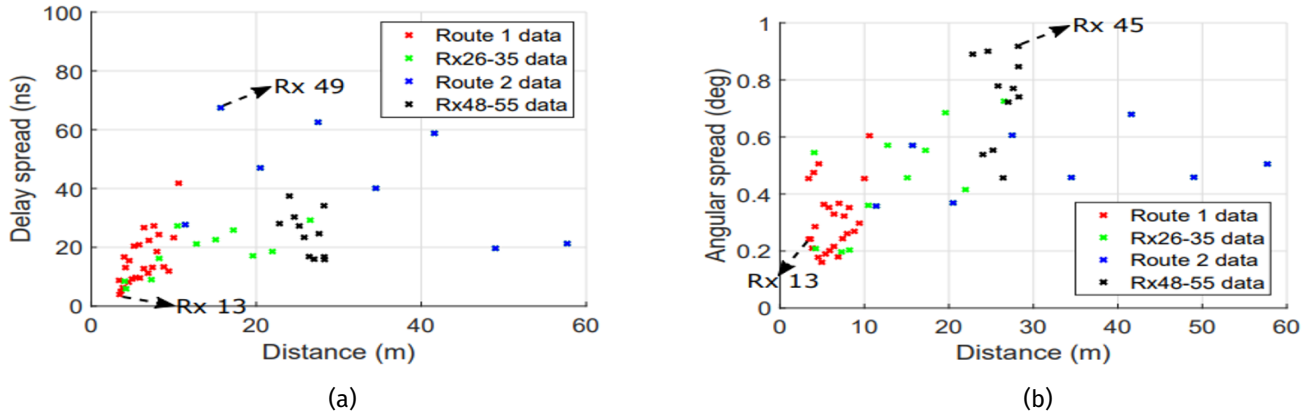


Figure 38: Results for a) delay spread versus Tx-Rx distance b) angular spread versus Tx-Rx distance

The delay spread changes in the delay range of [5.9, 67.5] ns. It is worth it to note that in Figure 38a, the delay spread data is divided into four groups, i.e., Route 1, Route 2, Rx 26-35 data (in the hall) and Rx 48-55 data (in the corridor). Obviously, the delay spreads increases in both Route 1 (represented by red color) and Rx 26-35 (in green) as the Tx-Rx distance increases. The latter can be explained by the decrease in the LoS power with increasing the Tx-Rx distance, while the variation in the Non-Light of Sight (NLoS) power remain comparatively small. For Route 2 (in black) and Rx 48-55 (shown in blue), the delay spreads decrease with an increase of the Tx-Rx distance. This reduction may be related to the diminishing relative difference between the LoS and the NLoS path lengths as the Rx moves closer to the scatterers, such as walls and windows, and further away from the Tx. Figure 38b presents the relation between the azimuth AoA spread and the Tx-Rx distance. The azimuth AoA spread is in the range [9.2, 52.58]°. Similar to the delay spread, the AoA spreads is also divided into four groups. It can be seen that the azimuth AoA spreads in all groups show an increasing trend as the Tx-Rx distance increases. The same reason as for the delay spread, in our understanding applies for the azimuth AoA spreads, i. e. it is also due to the decrease of the LoS power and the significance of the power of the NLoS paths with the increase of the distance.

The reader is advised to refer to Fig.7 (b), Fig.7 (c), Fig.8 (b) and Fig.8 (c) in [23], where the cumulative distribution function (CDF) of the calculated delay spread (in a logarithmic scale), an exemplary Power Delay Profile (PDP) comparison for two Rx locations, the CDF of the azimuth AoA spread in logarithm scale and exemplary PAS for low and high AoA spread cases are respectively presented. The CDF of the calculated delay spread matches to a great extent with a log-normal distribution. Moreover, several high delay spread cases over 60 ns (e.g. Rx 49) are observed. For the exemplary PDP comparison, it was found that in the Rx 13 case (with low spread), MPCs are mainly distributed in the delay range [14, 105] ns, while in the case of Rx 49 (high spread), a prominent MPC with a long delay of 340 was noticeable. This MPC is the reflection from the rear wall of the Rx 49. Furthermore, the delay spread does not provide much about the structure of the PDP, because a single MPC with long delay can drastically impact the delay spread. The CDF of the empirical AoA spread matches well with the log-normal distribution. Furthermore, there are several Tx-Rx cases with high azimuth AoA spread, such as Rx 45. For the Rx 13 case, the MPCs are mainly distributed in the AoA range [-107, -39]°. The average azimuth AoA (in the case of Rx 13) is -55.16°, closely matching with the AoA of the LoS path, which is -39°, resulting in a relatively low azimuth AoA spread. In the case of Rx 45, the estimated MPCs are located in two distinct AoA intervals, spanning from -126° to -73° and from 58° to 100°. The calculated mean azimuth AoA is -18.28° and is significantly different from both MPC azimuth AoA intervals.

The K-factor is a parameter evaluating channel characteristics on the small-scale [25], [26]. It is presented in Figure 39.

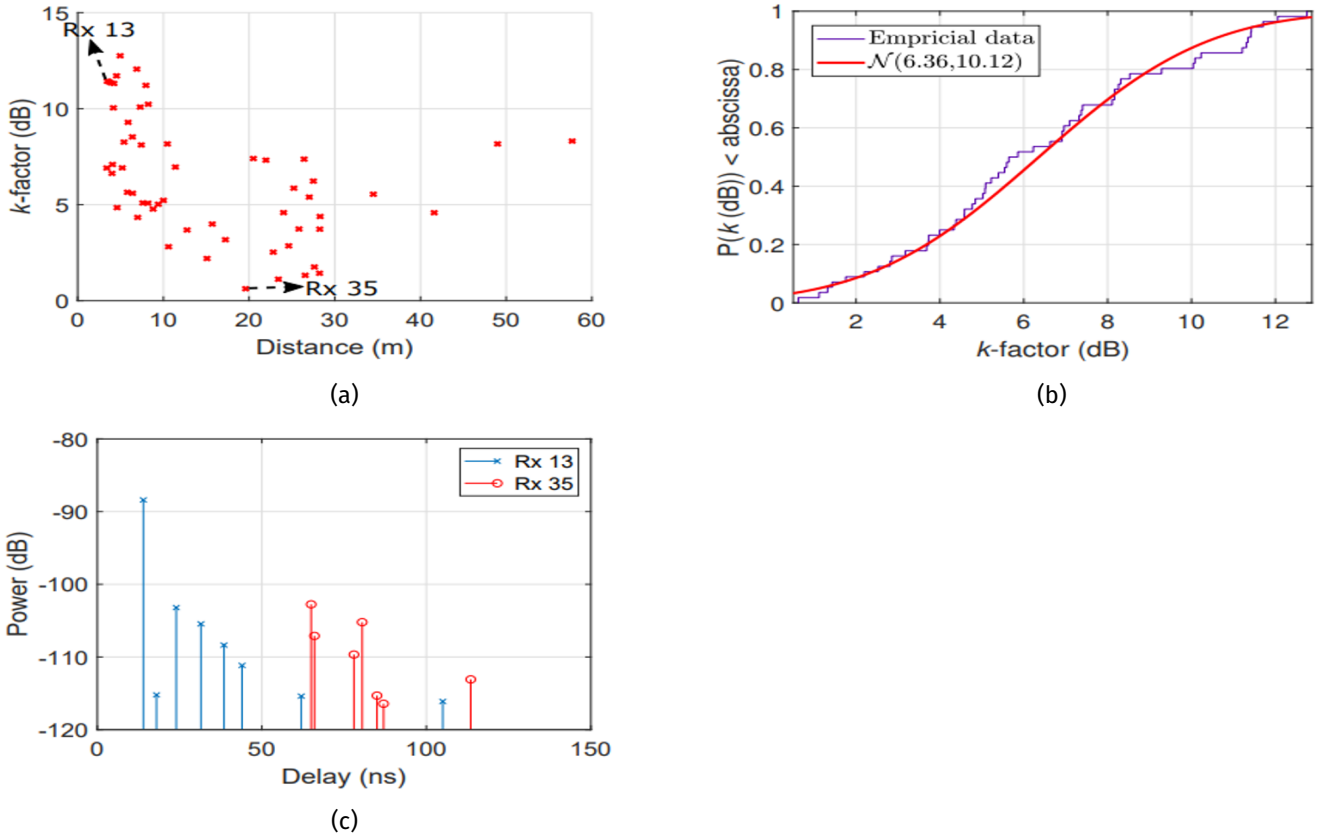


Figure 39: K-factor results calculated using the estimation results a) K-factor versus Tx-Rx distance b) CDF of the K-factor c) An exemplary PDP comparison of the low K-factor case (Rx 35, $k = 0.6$ dB) and the high K-factor case (Rx 13, $k = 11.4$ dB)

The K-factor changes in the interval $[0.62, 12.75]$ dB, as it is found that it decreases with the increase of the distance. The CDF results of the K-factor is in good agreement with the normal distribution function. In the Rx 13 case, due to the short Tx-Rx distance and spacious surrounding scenario, the LoS power is much higher than other MPCs. In the Rx 35 case, it is found that the power of the NLoS path is comparable to the power of the LoS, because the Rx 35 is in vicinity to the wall and to several metallic scatterers.

TABLE VI
COMPARISON OF OUR PROPOSED CHANNEL MODEL WITH THE EXISTING ONES.

Reference	Scenario	Path loss [dB]	Delay spread $\log_{10}(\text{ns})$	Angular spread $\log_{10}(^{\circ})$	K-factor [dB]
Our model @ 100 GHz	Indoor hall	$\alpha = 1.77$ $\chi_{\sigma}^{AB} = 74.40$	$\mathcal{N}(1.26, 0.07)$	$\mathcal{N}(1.36, 0.05)$	$\mathcal{N}(6.36, 10.12)$
[27] @ 100 GHz	Indoor hotspot	$\alpha = 1.73$ $\chi_{\sigma}^{AB} = 72.40$	$\mathcal{N}(1.28, 0.03)$	$\mathcal{N}(1.40, 0.14)$	$\mathcal{N}(7, 16)$
[28] @ 28 GHz	Indoor hall	$\alpha = 1.81$ $\chi_{\sigma}^{AB} = 62.36$	$\mathcal{N}(1.53, 0.19)$	$\mathcal{N}(1.96, 0.10)$	—

Table VI presents a comparison of our model and two other models. In [23], the reader can find more information about comparison between the proposed channel and other channel models. In the Third Generation Partnership Project (3GPP) 38.901 model [27], the channel models in indoor hotspot office ($1 \leq d \leq 150$ m) cover the frequency bands up to 100 GHz. It is quite similar to our measurement case presented here (hall scenario with the Tx-Rx distance ranging from [3 - 58] m at 100 GHz). Compared the proposed channel model with the 3GPP model, it can be observed that the fitted model of the delay spread, angular spread, and K-factor match closely to those in the 3GPP model. In order to demonstrate the channel sparsity at 100 GHz bands, the number of the extracted MPCs for Route 1 and 2 (by using a dynamic range of 30 dB) is presented in Figure 40 and analyzed.

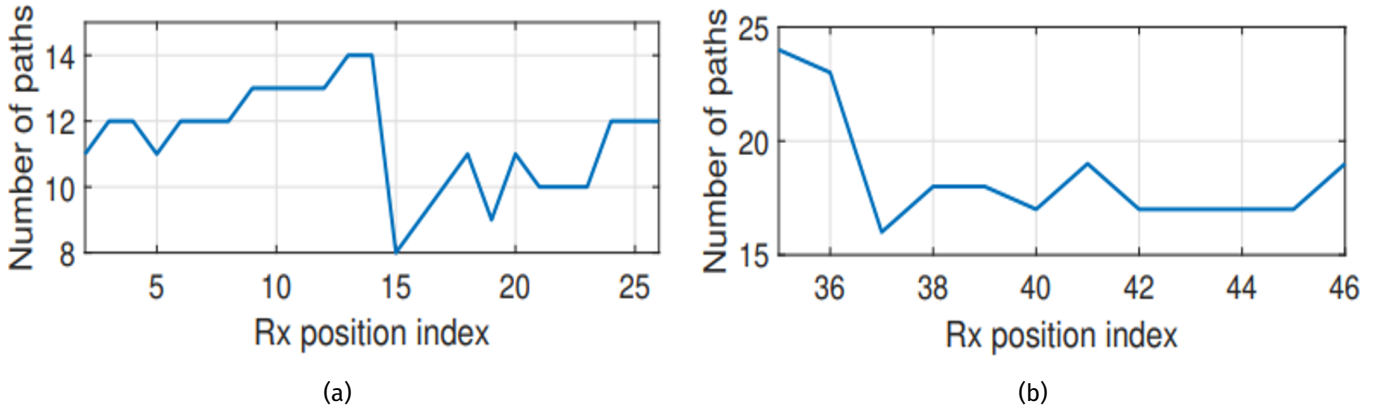


Figure 40: Number of MPCs detected using 30 dB dynamic range a) Route 1 b) Route 2

In Route 1, the number of detected MPCs is between 8 and 14. In Route 2, we can identify more MPCs (between 16 and 24). The latter is due to the fact that Route 1 is deployed in a spacious scenario with only several pillars in vicinity, while Route 2 is deployed in a scenario close to windows, walls and several metallic scatterers, providing more reflections and MPCs. The channel at 100 GHz shows sparsity and specularity. The number of trajectories per Rx location for both routes is illustrated in Figure 41.

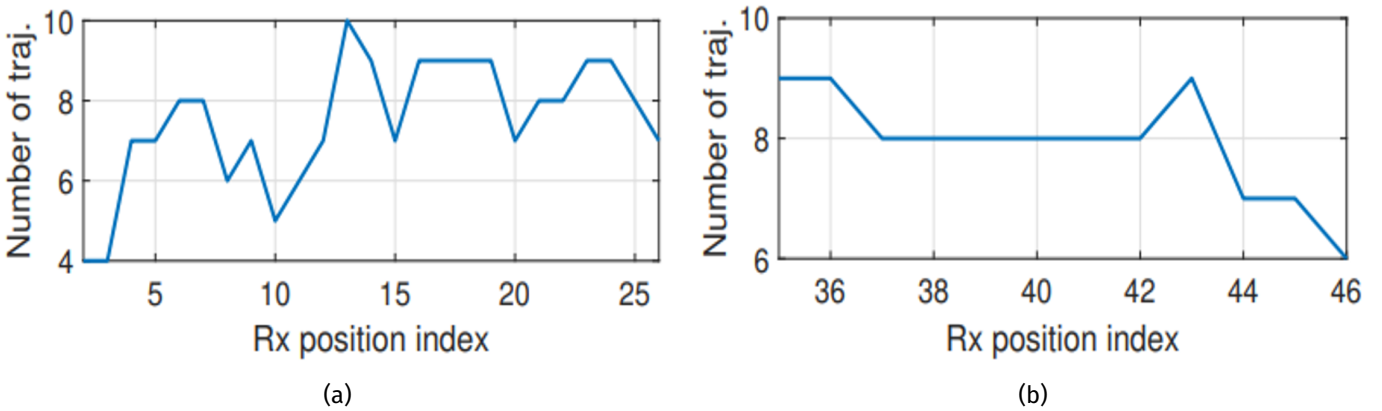


Figure 41: Number of trajectories in each Rx location a) Route 1 b) Route 2

For Route 1, the number of trajectories per Rx location varies from 4 to 10, while in the case of Route 2, it varies from 6 to 9.

In this section, sub-THz channel measurements were conducted in an indoor hall scenario at the frequency range (99-101) GHz covering the Tx-Rx distance in the range 3-58 m. The Tx was fixed, while the Rx was deployed in 55 positions, including 2 predefined routes. For each Tx-Rx measurement, the virtual UCA scheme was used with a radius of 6.7 cm and rotation step of 1° , corresponding to 360 VAA elements in each Tx-Rx measurement. By applying the FIBF algorithm with the SIC procedure, it was possible to accurately estimate and extract the channel parameters from the measurement data. The number of the detected MPCs (using a dynamic range of 30 dB) was within the range from 8 to 24, showing the sparsity of the 100 GHz channel. The PL, shown in dB over distance, exhibits a strong fit to the linear model. The delay and angular spreads are observed to match the log-normal distributions, while the K-factor fits well to the normal distribution. Furthermore, the MCD-based trajectory tracking algorithm was applied to trace the observed MPC paths within the measured channel based on the estimated MPC results. The geometry-based analysis of the dominant NLoS trajectories was made. The delay and azimuth AoA of these dominant trajectories closely match with the spatial characteristics of the hall. In addition, the proposed 100 GHz channel model was compared with the existing models. The comparison between our model and 3GPP 38.901 model, covering up to 100 GHz, demonstrates the correctness of the proposed model in the current work. Future work would include outdoor 100 GHz channel measurement and modeling and MCD-based clustering studies at different frequency bands.

2.3 Double DSS measurements for channel characterization in a large hall scenario at 300 GHz

Future wireless communication systems, i.e., beyond fifth-generation (B5G), have been attracting increasing interest worldwide as the need for high data-rate in various applications continue to grow [28], [29]. Sub-terahertz (sub-THz) technologies, defined at the frequency bands in 100-300 GHz, are envisioned to be one of the core radio technologies for B5G communication systems, due to their large unused and unused frequency resource [30], [31]. However, as it was discussed in [32] the atmospheric attenuation at sub-THz bands is much higher compared to that at lower frequency bands. Moreover, the wavelength of the sub-THz frequencies is close to the size of the dust and the rain drops, which makes the channel at sub-THz bands to behave much differently than that of the conventional low frequency spectrum [33]. Although, numerous sub-THz measurement campaigns have been proposed in the literature, they are either focused on characterization of the sub-THz channel in the short-range indoor scenarios, e.g., office and meeting rooms [34], [35], [36], [37], [38], [39], [40], or only a few of long-range measurements have been reported in the long-range scenarios and mainly at 140 GHz [22], [41].

Therefore, the lack of experimental studies on channels in long-range scenarios at 300 GHz has motivated the work in [42], which serve as the basis for the content in this subchapter. The high fidelity of the long-range channel sounder has been validated in [34]. However, the channel characteristics and channel models at 300 GHz are not further analyzed in [34], because the measurement was conducted only for one measurement location. Therefore, in this chapter (based on the work [42]), channel measurements have been conducted using a DDSS to explore 300 GHz channel characteristics in a large hall scenario. Furthermore, the channel measurements are conducted with 8 different Tx-Rx distance ranging from 3-15.6 m. The investigation was based on the large amount of the directional measurement data, i.e., 33120 CFR, which helped the calculation and analysis of the PADPs and power-angle spectra (PAS). Moreover, analysis of the key measurement-based channel parameters including PL, and dispersion spread in delay and angle domain is made. The cost-effective multi-link phase-compensated channel sounder proposed in [2] (please refer to Figure 5 in section 2.2.2.1) is used in the sub-THz channel measurements. To limit the high PL, directive antennas are used in measurements. The antenna gain for the antennas on both sides is 26 dBi. The used dynamic range is 50 dB in these measurements with the IFBW of 1 kHz.

Figure 42 illustrates the the large hall measurement deployment scenario.

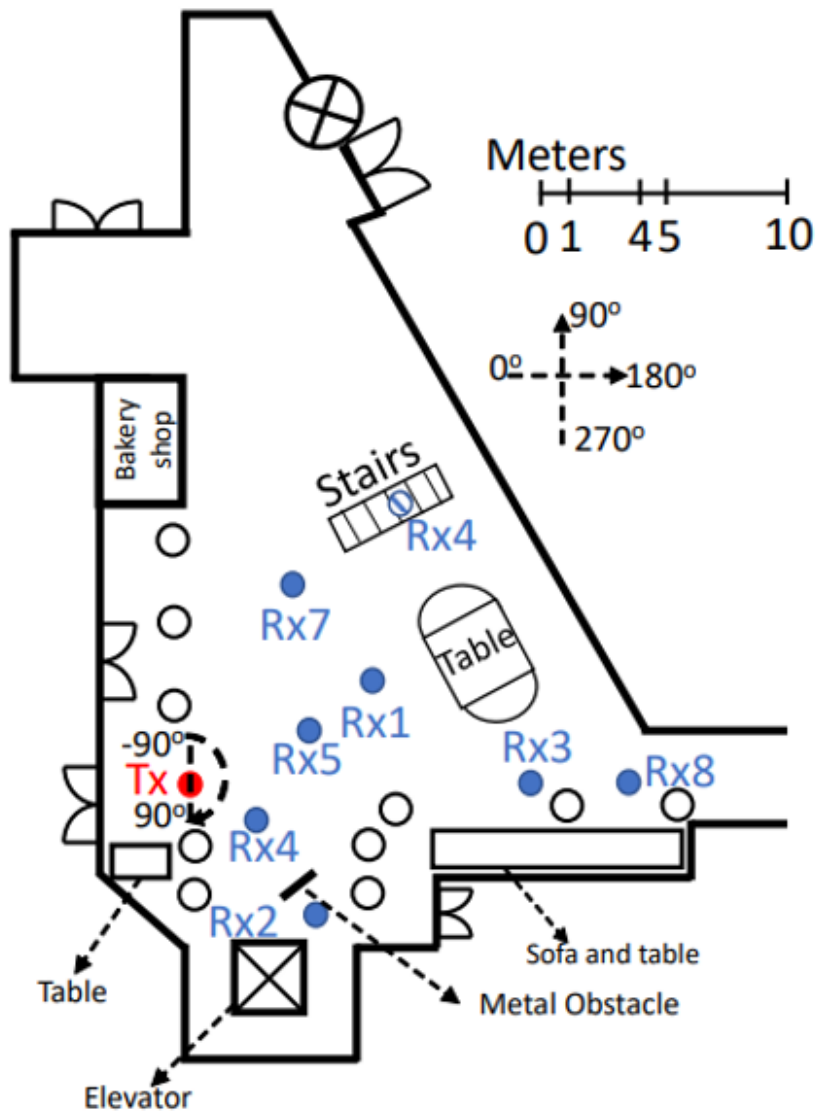
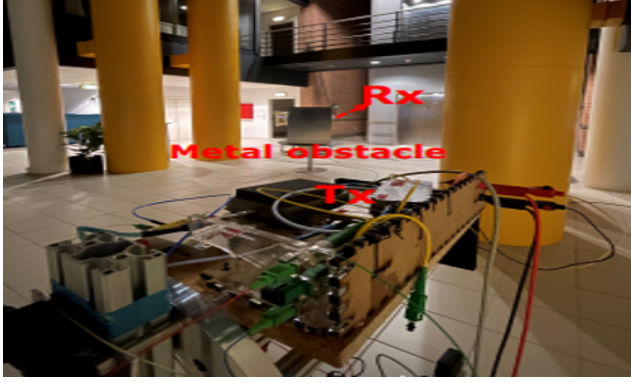
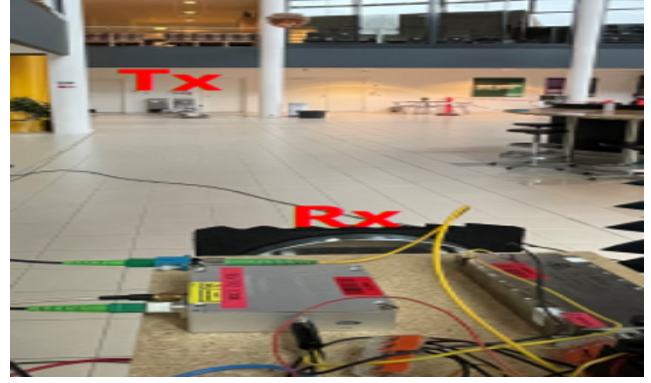


Figure 42: Top view of the large hall scenario

The channel measurements are conducted in a large hall with a size of 42 m × 25 m. More specifically, the size of the corridor is 43.4 m × 3.7 m. Figure 43 show the pictures in the real scenario.



(a) Tx-Rx 2



(b) Tx-Rx 3



(c) Tx-Rx 4

Figure 43: Photos of the measurement scenario

In these measurements, the Tx is deployed near the wall to mimic the BS, while four Rx locations are used to investigate the LoS scenario (i.e. Rx 1 and Rx 3) and the NLoS scenarios (i.e., Rx 2 and Rx 4). Note that Rx 4 is positioned underneath the stairs and the LoS is completely blocked, while the NLoS case of Tx-Rx 2 is formed by adding a metallic plate with the dimension of $56 \text{ m} \times 85 \text{ mm}$, as illustrated in Figure 43a and in Figure 43c. Moreover, four channel measurements with different Tx-Rx distances in the LoS cases are also conducted, i.e., Rx 5 - 8, to model the channel parameters. To obtain the channel information in the spatial domain, the DDSS was used in the measurements. To eliminate the effect of the system, an Over-the-Air (OTA) calibration is performed, by using 1 m LoS channel measurement results as a reference to calibrate the system and antenna responses. The Tx and Rx extenders are mounted on two turntables. The Tx and the Rx are programmed to rotate the azimuth in the range of $[-90^\circ, 90^\circ]$ and $[-180^\circ, 176^\circ]$, respectively. The rotation step is 4° at both sides. According to [34], the 4° rotation angle step is found to be sufficient for wideband channel spatial profile reconstruction. Thus, the number of CFR obtained for each measurement point is $45 \times 90 = 4140$. In total, 33 120 CFR are obtained (i.e., number of Tx-Rx pairs \times number of measurement locations). For more information, the detailed measurement specifications can be found in Table 3 in [42]. Furthermore, equations (1)-(10) in [42] give the relations for all channel characteristics and parameters estimated in the current investigation.

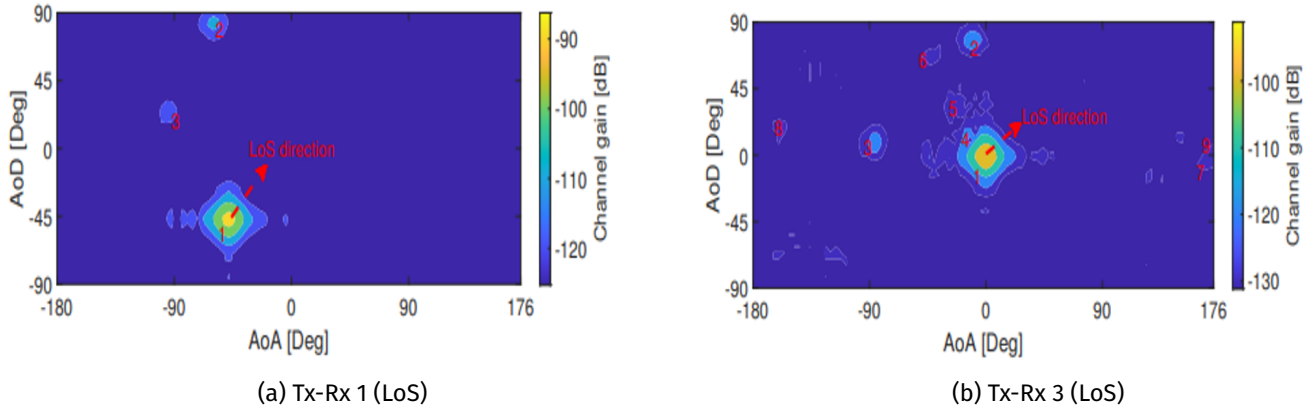


Figure 44: Exemplary DDPAS for the LoS measurement locations

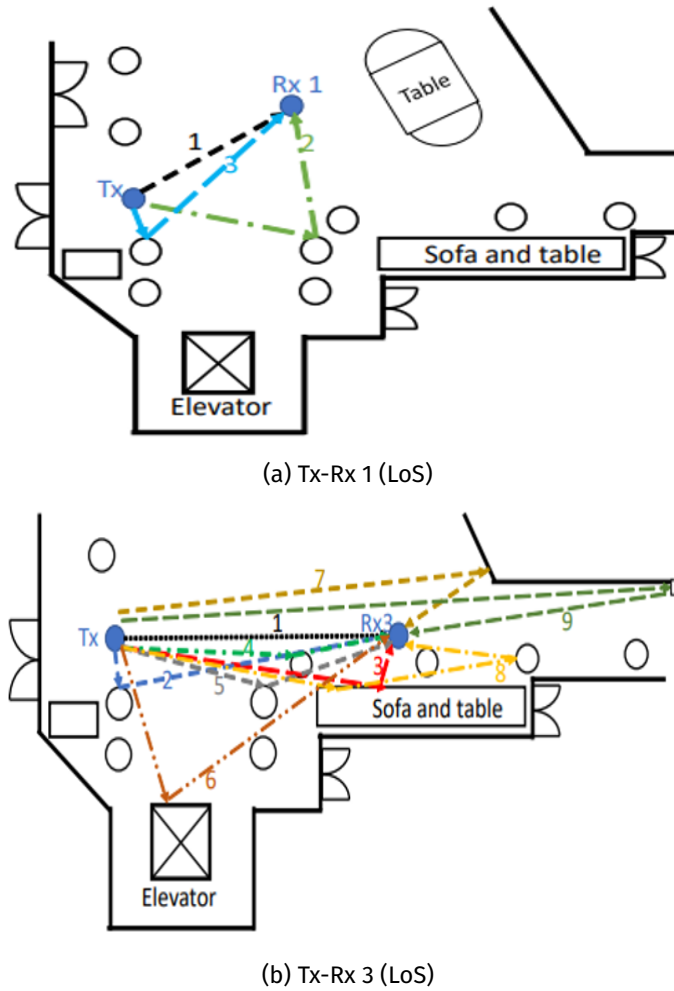


Figure 45: Exemplary DDPAS for the LoS measurement locations

Figure 44 show the exemplary DDPASs of the measured LoS channel. Furthermore, Figure 45 presents the relation of the main paths in the channel to the room geometry. In the Tx-Rx 1 scenario, the LoS path has the delay of 20 ns,

the angles of departure (AoD) of -46° , and the AoA of -48° , which matches well the geometry of the Tx-Rx deployment scenario. In the Tx-Rx 3 LoS scenario, the LoS component has the delay of 38 ns, the AoD of 0° , and the AoA of 0° . As it would be expected, the power is observed to be highly concentrated around the LoS direction, while also several additional reflection contributions from various directions could be identified. Moreover, with the measurement distance increasing from 5.9 m to 11.4 m, the LoS path power decreases from -40.4 dB to -45.3 dB. The number of MPCs in these two LoS scenarios are found to be respectively 2 and 8. Path 9 is observed to be the reflection from the window structure of the corridor. From the measured results, the multipath is found to be specular and sparse from the measured results. AoAs of the main paths in the LoS scenarios match the room geometry.

The DDPASs and PADPs in the Tx-Rx 2 NLoS scenario are presented in Figure 46 and in Figure 47, respectively.

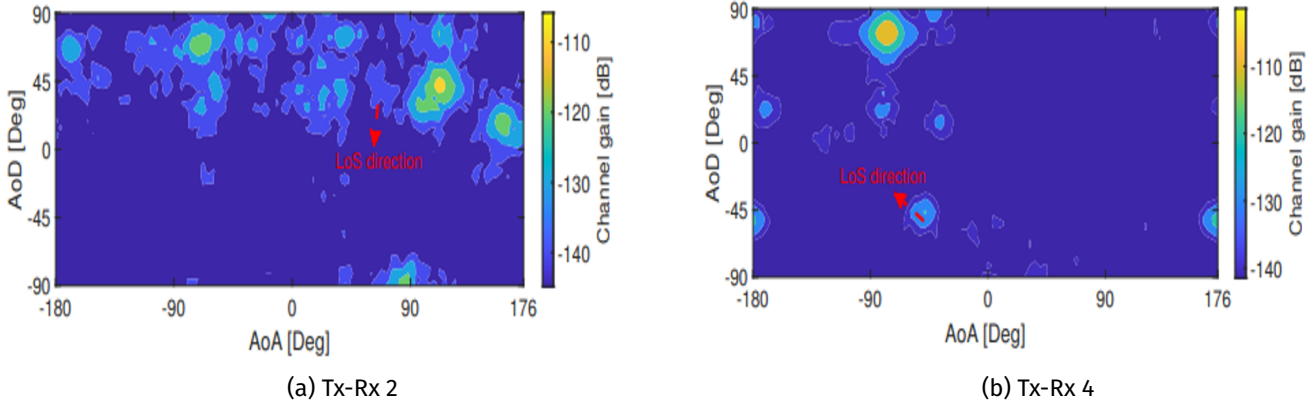


Figure 46: DDPAS for the NLoS measurement locations

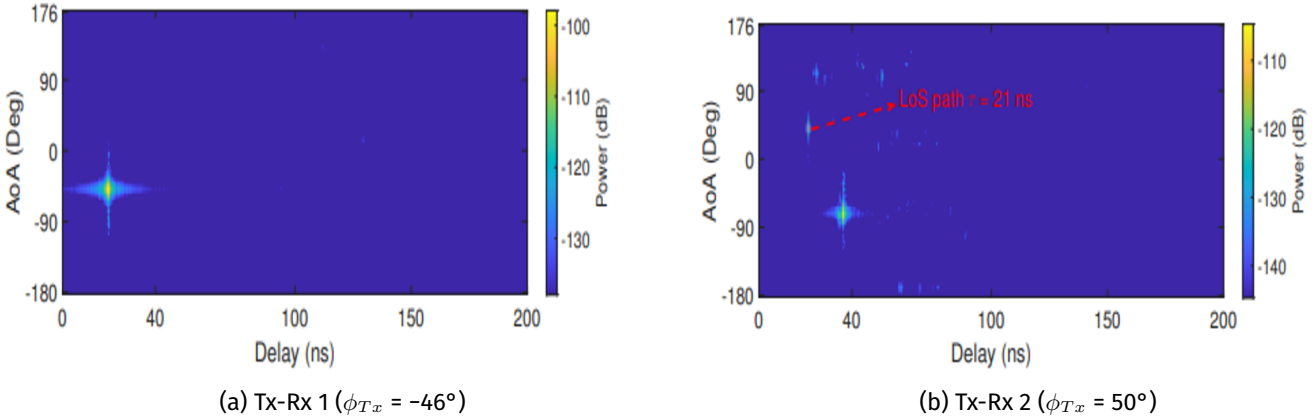


Figure 47: Exemplary PADP for LoS and NLoS locations at the LoS direction

The LoS path can be observed with the delay of 21 ns (matching well the Tx-Rx 2 distance of 6.2 m) and power of -77.2 dB, which may be caused by the diffraction from the edge of the metal obstacle. Moreover, the MPCs are mainly concentrated in the AoD range of $[0^\circ, 90^\circ]$. In the Tx-Rx 4 NLoS scenario, the LoS path is blocked totally by the stairs, and the MPCs in this case are mainly concentrated in the AoA range of $[-180^\circ, 0^\circ]$.

Furthermore, compared with the DDPAS from the LoS scenario, the MPCs in the NLoS cases are richer compared

to those in the LoS cases, because of the fact that the dominant LoS components are blocked and thus, the difference in power between various MPCs is less.

More results are presented in Figure 10 to Figure 15 in [42]. Figure 10 in [42] presents an exemplary omnidirectional PDP comparison. In the Rx 1 and Rx 2 cases, it is found that the LoS path in the OLoS case is blocked and the power decreases from -40.4 dB to -67.7 dB compared to that in the LoS case. Moreover, in both cases, the MPCs are rich. The MPCs are observed to appear in the delay range of $[21, 250]$ ns, which corresponds to the propagation distance range of $[6.3, 75]$ m. Furthermore, in both cases, few weak paths over 400 ns, which corresponds to the propagation distance of 120 m, can be identified. In the Rx 3 and Rx 4 cases, the LoS path in the NLoS case (i.e., Rx 4) is blocked completely resulting in power reduction of 58.5 dB compared to LoS case. The MPCs in NLoS case are mainly seen in the delay range of $[50.5, 270]$ ns, which corresponds to the propagation distance range of $[15, 81]$ m, while the omnidirectional PDP in the LoS case is found to have a longer decay in the delay range of $[37.5, 446.5]$ ns. Figure 11 in [42] compares the empirical and modeled PL-es. The antenna gain is not taken into an account in the omnidirectional PDP calculation. Comparatively good match between the different theoretical and measured PL-es have been observed. For more details, the reader can refer to Figure 11 in [42]. Figure 12 in [42] presents the comparison of the empirical delay spread. The empirical delay spreads in the LoS cases is within the range $[7.5, 35.6]$ ns. Moreover, the LoS delay spreads increase with the increase in the link distance between the Tx and the Rx, which is caused by the decreased LoS power and the fact that the power of MPCs becomes more comparable to that of the LoS path. In the NLoS cases, the delay spread of the Rx 2 is 14.8 ns higher than that of Rx 1, while the delay spread of the Rx 4 is 7.6 ns lower than that of Rx 3. The relation of the empirical angular spread to the link distance between the Tx and Rx is shown in Figure 13 in [42]. The LoS AoA spreads are within the interval $[18^\circ, 43^\circ]$ and increases with the distance. Moreover, the LoS AoD spreads are found to increase with the measurement distance range of $[3, 8.1]$ m, and decrease in the Tx-Rx distance range of $[8.1, 15.6]$ m. Figure 14 in [42] shows the PAS comparison of the different Rx locations - Rx 3, Rx 7, and Rx 8. The Rx 7 has a larger AoD difference between the LoS direction and the mean AoD compared to those of the Rx 3 and Rx 8, which can be explained by the higher contribution of the MPCs on the angular spread in the Rx 7 case. For the NLoS scenarios, the AoA spreads of the two NLoS cases, i.e., Rx 2 and Rx 4, are 88.0° and 115.2° , respectively, which are observed to be much higher than those AoA spreads at the same distance. Figure 15 in [42] presents the comparison of the PAS in azimuth and the mean azimuth for the LoS and NLoS cases. It is found that the mean AoA appears near the LoS peak in Rx 1 and Rx 3 (LoS cases) and that the LoS power contributes dominantly to the angular spread, which leads to a small angular spread around the mean AoA (i.e., LoS) direction. The opposite is observed for the Rx 2 and Rx 4 (NLoS cases), the LoS path is blocked and the MPCs contributed more significantly to the angular spread. The AoD spread of the Rx 4 is 43.6° higher than that of Rx 3 and the AoD spreads of Rx 1 and of Rx 2 are observed to be similar. The measured channels are found to be specular and sparse.

In this chapter, the measurement results of the double-directional sub-THz channel measurements at 300 GHz bands in a large hall scenario are presented. The distances between the Tx and the Rx are 3-15.6 m. Both LoS and NLoS cases are considered in the measurements. Channel characteristics, i.e., DDPAS, PADP, PL, delay spread, and angular spread, are estimated and discussed. The DDPAS results show a good agreement with the room geometry, which demonstrates the accuracy of the performed measurements. The DDPAS results in the LoS scenario validate also the sparsity of the multipaths at 300 GHz. The empirical PL related to the measurement distance in dB is well-fitted by the theoretical model and found to be close to the theoretical FSPL model.

The LoS delay spread is found to increase with the Tx-Rx distance. Compared with the low angular spreads in the LoS cases, the angular spreads at NLoS cases are observed to be much higher. Moreover, MPCs are observed in the omnidirectional PDP over 200 ns (corresponding to 60 m). This indicates the accuracy of the long-range channel measurement campaign at 300 GHz. More long-range 300 GHz channel measurements must be conducted in the future.

2.4 Channel measurements between 330 and 500 GHz for indoor and corridor scenerios

2.4.1 Select measurement results

2.4.1.1 Laboratory scenarios A comprehensive set of measurements was performed using both traditional short-range systems and RoF-enabled long-range systems to assess the effectiveness of the RoF approach across the 330–500 GHz frequency range. These measurements were carried out in multiple scenarios using the Keysight vector network analyzer and Rohde & Schwarz ZNA vector network analyzer using the equipment as listed in 5.

It is assumed that if the responses of both systems are comparable, the additional components in the RoF system including the electro-optic (EO)/optical-electrical (OE) converters, 600 m of optical fibre, and coaxial cables introduce negligible effects on the measurement outcomes. Due to the range limitations of coaxial cables in the non-RoF setup, the comparison was restricted to a LOS channel with antenna separations up to 250 mm. A SGH-26-WR2.2 horn antenna was employed to compensate for anticipated PLs. The tests were carried out in a temperature-controlled laboratory, with over an hour of stabilization time, and fiber was secured to minimize bending stress, eliminating the need for phase compensation.

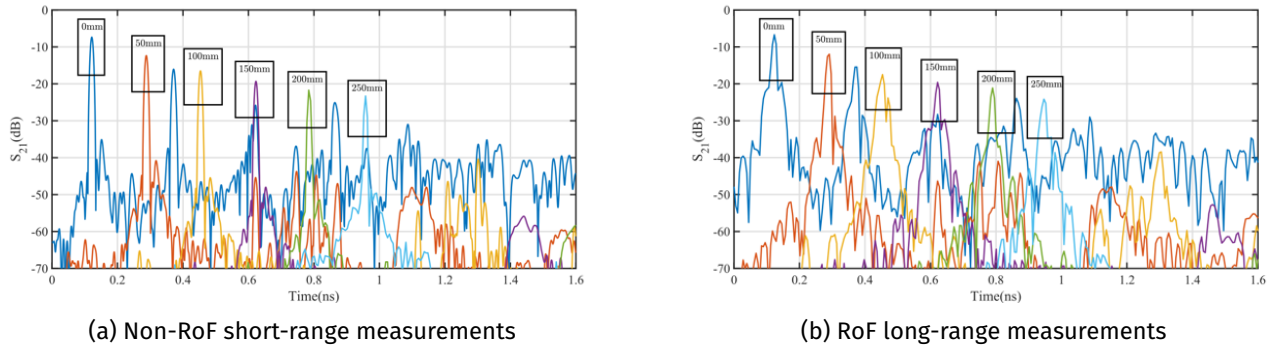


Figure 48: CIRs results for 330–500 GHz channel sounding up to 250 mm separation, and the measurement setup in a laboratory environment.

The traditional system was set up with each extender head connected to the Keysight VNA using 1.2-meter cables,

followed by a full two-port Thru-Reflect-Line (TRL) calibration. A continuous frequency sweep from 330 to 500 GHz was performed, with 25001 frequency points and an IF bandwidth of 10 MHz. The two antennas were precisely aligned in a LOS configuration using laser guidance.

The RoF-enabled long-range system, with the Rx extender head connected via up to 600 m of RoF and coaxial cables, was calibrated using the enhanced response method, moving the reference plane to the waveguide test ports. TRL standards were measured on the local Tx unit, connected to the VNA via 1.2 m cables, and SGH-26-WR2.2 horn antennas. A continuous sweep from 330 to 500 GHz was performed with 25,001 frequency points and a 50 MHz IF bandwidth.

The VNA recorded the measurements for short-range system and RoF-enabled long range system as S-parameters at discrete frequency points and then converted to the time domain. Measurements were then taken at sequential separation distances of 0, 50, 100, 150, 200, and 250 mm respectively. The results shown in Figures ??(a) and ??(b), corresponding to the CIRs results for Non-RoF and RoF systems, respectively, demonstrate that the delay between peaks increases as the antenna separation increases, which is expected as wave propagation occurs at a constant speed over a longer distance. Additionally, the amplitude of the peaks decreases with increasing separation due to greater free-space PL. Preliminary results of the non-RoF and RoF systems, with consistent peak positions and amplitudes. The noise differences are due to active components in the long-range system and a higher IF bandwidth, although the peaks remain above the noise floor.

To further validate the system configuration, the same measurement setup was employed using the Rohde & Schwarz ZNA vector network analyzer in a 6G laboratory environment at QMUL. The process began with normalization, followed by the extraction of CIR at various distances. Results for LOS separations of 2.90 m and 5.61 m are presented in Figure 48(a), while the corresponding laboratory measurement setup is shown in Figure 48(b). These measurements adhered to the procedure described earlier, with the exception that a higher number of frequency points was used for the 2.9 m and 5.61 m cases to enhance time-domain resolution.

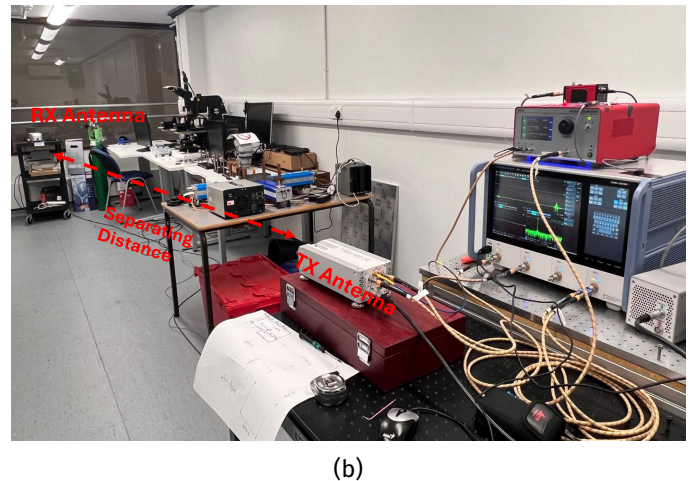
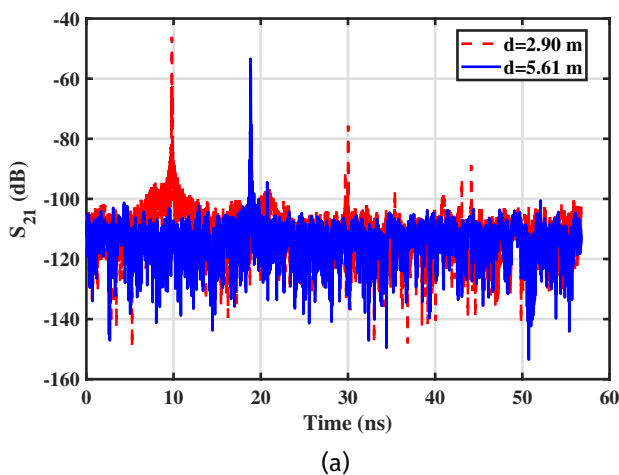


Figure 49: (a): CIRs results for 330–500 GHz channel sounding for 2.90 m and 5.61 m separation distance, (b) The measurement setup using Rohde & Schwarz ZNA in a laboratory environment.

2.4.1.2 Atrium To further validate the experimental setup, a series of measurement campaigns were conducted within the atrium environment, with its dimensions and layout illustrated in Figure 50a.

During these campaigns, the transmitter Tx remained stationary, while the receiver(Rx1 to RX7) was systematically positioned at seven distinct locations, as shown in Figure 50a. To ensure accurate LOS conditions, antenna alignment was carefully maintained along a direct LOS path by rotating Tx antenna face towards Rx antenna Face. A laser pointer was used to verify and ensure precise alignment between the transmitter and receiver, allowing unobstructed signal propagation throughout the measurement process.

The same measurement procedure described in Section 2.5.1.1 was applied here with Rohde & Schwarz ZNA vector network analyzer. The key difference lies in the environment: the NPL Atrium, which features walls constructed from a variety of materials, including a combination of metal, glass, bricks, and a concrete floor with a approximate dimension of 15x20x6 m(see Figure 50a). One of the walls is made of a glossy surface, introducing additional reflective characteristics to the environment. S-parameters were measured across a range of discrete frequency points and subsequently transformed into the time domain to extract the CIR. As illustrated in Figure 50 , the receiver Rx was systematically relocated to seven distinct positions(Rx1 to Rx7) within the environment, with one CIR recorded at each location(see Figure 51). The results reveal a progressive increase in the time delay between peaks as the distance between the transmitter and receiver grows, an expected behavior due to the constant propagation velocity of electromagnetic waves. Furthermore, the peak amplitude decreases with increasing separation, which is consistent with the rise in free-space PL over longer distances.

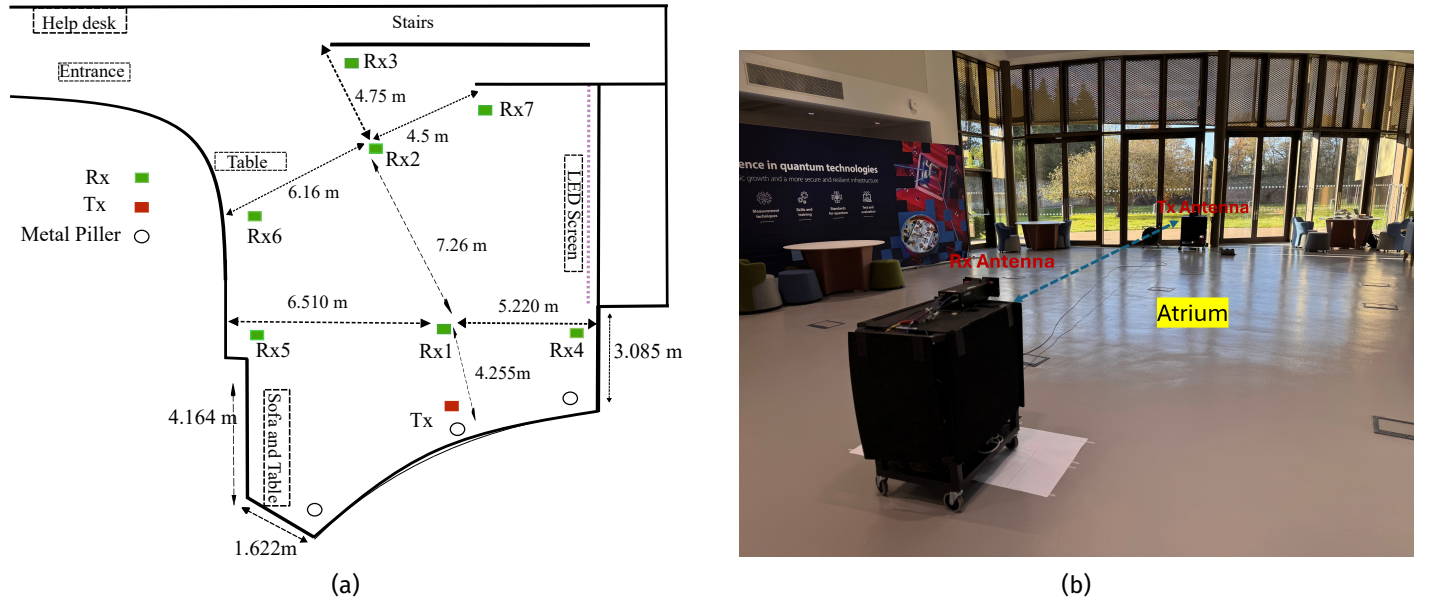


Figure 50: Measurement setup for the 330–500 GHz band in the NPL atrium environment. The transmitter (Tx) remained fixed, while the receiver (Rx) was sequentially placed at seven distinct locations, labeled Rx1 to Rx7, with measurements recorded at each position. (a) Schematic layout showing the positions of Tx and the seven Rx locations, along with the dimensions of the NPL atrium. (b) Photograph of the actual measurement setup depicting Tx and the Rx2 configuration.

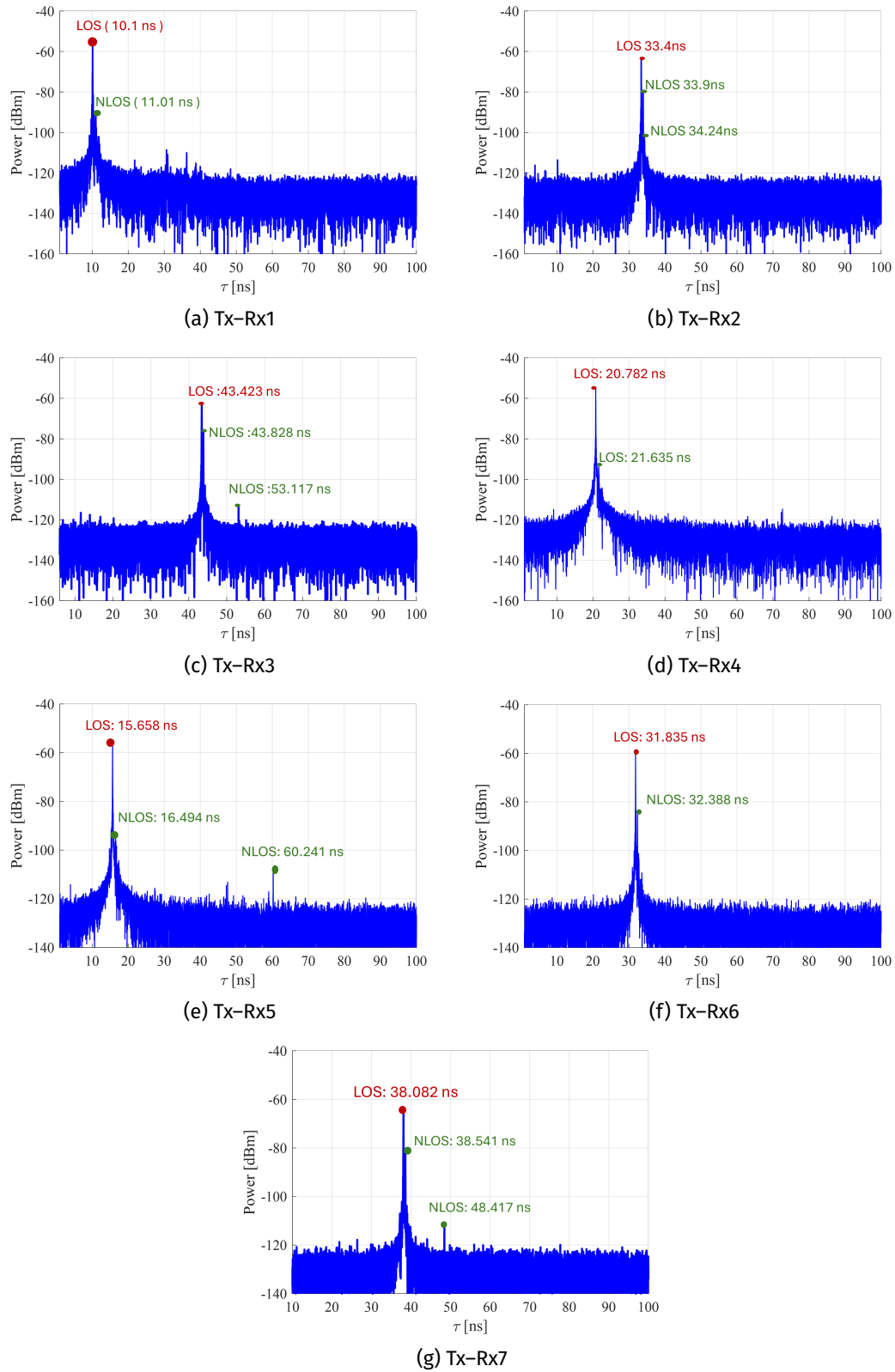


Figure 51: CIRs for 330–500 GHz frequency range measured in the NPL atrium environment with a fixed transmitter (Tx) and the receiver positioned at seven distinct locations. Each subfigure (a–g) corresponds to a unique receiver position (Rx1–Rx7), showing the CIR observed at that point.

Table 1: Non-RoF and RoF Measurement Parameters for Laboratory Scenario

Measurement Parameter	Non-RoF System	RoF System
IF Bandwidth	5 Hz ^a	10 Hz
Points	2501	2501 ^b
Start Frequency	500 GHz	500 GHz
Stop Frequency	750 GHz	750 GHz
Meas. cable length (Rx)	1.2 m	600 m
LO cable length (Rx)	1.2 m	600 m
Channel sounding range	0 m – 0.25 m	0 m–0.25 m, 1.39 m, 4.48 m

^a 1 kHz before IF Auto BW ^b 5001 for 4.49m distance

2.5 Channel measurements between 500 and 750 GHz for indoor, corridor and outdoor scenarios

2.5.1 Select measurement results

2.5.1.1 Laboratory A series of measurements was carried out using traditional and RoF enabled systems to evaluate and compare the effects of the RoF system for measurements up to 750 GHz [7]. The scenario consists of a bench-top setup, in the middle of a screened general-purpose laboratory, approximately 10x15 meters in dimension.

It is assumed that if the response of both systems are comparable, the additional components in the RoF system (EO/ OE converters, 600 m of fibre and coaxial cables) introduces negligible effects on the measurement outcomes.

Given the range limitations of the coaxial cables in the non-RoF system, the comparison was constrained to a line-of-sight channel with antenna separations up to 250 mm. The antennas used are the VDI WM-380 diagonal horn antennas, offering a high gain of 26 dB, which mitigates the significant PL encountered during channel measurements. All measurements were conducted in a temperature-controlled laboratory environment, reducing the phase shift over measurements in the fibres and coaxial cables. Prior to data collection, the system was allowed to stabilize for over one hour. Additionally, the optical fibre was coiled and secured to reduce bending stress. These precautions reduced the need for phase-compensation techniques in this scenario.

In the non-RoF setup, each extender head was directly connected to the VNA using 1.2-meter cables. A full two-port Thru-Reflect-Line (TRL) calibration was applied to establish a measurement plane at the end of the extender head waveguide test ports, before the antennas are connected. The VNA settings and measurement parameters are summarized in Table 1. The horn antennas were aligned face-to-face and repositioned incrementally at separations of 0, 10, 20, 40, 50, 100, 150, 200, and 250 mm.

S-parameters were recorded across discrete frequency points and subsequently converted to the time domain. The results, shown in Figure 52(a), exhibit a consistent increase in delay between peaks as antenna separation increases. An expected outcome due to constant propagation velocity. Similarly, peak amplitude decreases with distance, attributed to free-space PL increasing with distance. For the 0 mm separation case, the signal magnitude peak, representing the LOS path, shows a non-zero delay. This is due to the calibration reference plane being located at the antenna's input waveguide interface. The measured delay (180 ps) corresponds to a physical path length of approximately 54 mm, which aligns with the combined length of both horn antennas (24 mm each).

The next configuration measured includes the 600 m RoF link and coaxial cables to remote the Rx extender head. Calibration was performed using the enhanced response method, which shifts the reference plane to the waveguide

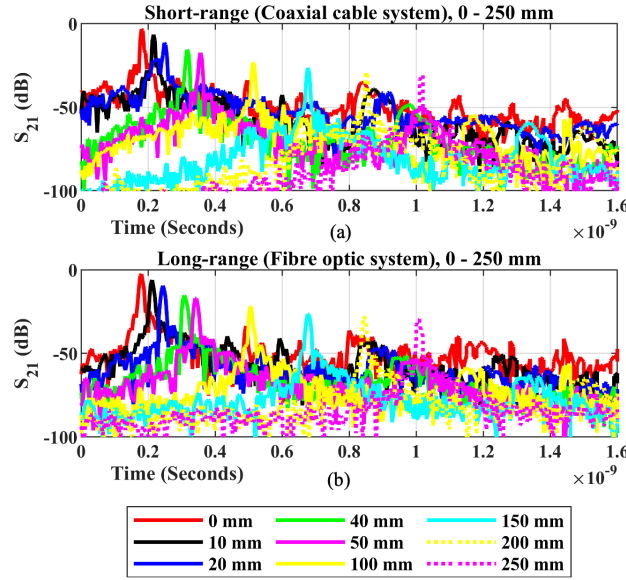


Figure 52: Time domain results for 500 GHz – 750 GHz channel sounding up to 250 mm separation with (a) Non-RoF and (b) RoF systems

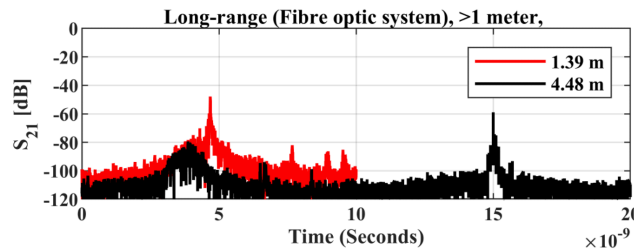


Figure 53: Time domain results for 500 GHz - 750 GHzx channel sounding at longer separations for the RoF system

test ports and enables error correction without requiring all measurement of all calibration standards at the remote unit. Reflect standards were measured only at the local Tx extender unit, which remained directly connected to the VNA with coaxial cables.

The antennas were then installed, and measurements were carried out using the parameters listed in Table 1. Figure 52(b) presents the time-domain results for the long-range system, which closely mirror those from the short-range system. The peak positions and amplitudes have strong agreement, confirming that application of the RoF system is not detrimental the measurement results. Additionally, the phase-compensation is unnecessary under the controlled setup due within this specific scenario.

Some variance in noise levels around the peaks was noted, attributed to additional active components (optical converters and amplifiers) in the RoF system. Furthermore, the IF bandwidth was increased to shorten measurement duration, which also contributed to the elevated noise floor. However, this increase remains within acceptable bounds, as signal peaks remain well above the noise.

Results for laboratory scenario channel distances exceeding 1 m are illustrated in Figure 53. These measurements followed the same procedure described earlier, except for the 4.48 m separation case where the number of frequency

points was increased to extend the time resolution. The resulting peaks correspond closely with theoretical line-of-sight delays, 4.64 ns for 1.39 m and 14.9 ns for 4.48 m. Confirming the system's validity at longer distances.



Figure 54: Atrium measurement location with (a) receive trolley located in position Rx2 and (b) the receive measurement trolley from the perspective of the transmit antenna

Table 2: Measurement Parameters for the Atrium Scenario

Measurement Parameter	Value
IF Bandwidth	50 Hz ^a
Points	25,001
Start Frequency	500 GHz
Stop Frequency	750 GHz
Meas. cable length (Coaxial)	100 m
LO cable length (Fibre)	100 m
Channel sounding range	0 m – 30 m
Sweep duration	ca. 400 seconds

^a Calibrated at 1 kHz.

2.5.1.2 Atrium Atrium, a large indoor circulation space on the NPL campus used for gatherings, seating and conferences. This is a suitable indoor environment for channel sounding measurement, where sub-THz signals could potentially be used for medium-range (c.30 meters) high bandwidth communications. The space measures approximately 15x20x6 meters in length, width and height respectively. The construction was completed in approximately 2020 and as such the structure uses modern material such as multi-layer glass glazing, plaster, brick walls and concrete flooring. There is also furniture within the space, which has been moved such that it has a minimal effect on the expected propagation paths of the channel sounding measurements.

A set of measurement locations have been chosen to sample the space around the room. These have been placed to test different effects of the room structure, such as parallel and perpendicular walls, mid-points and corners. A fixed transmit location (Figure 55 Tx1) has been selected for the measurements due to the complexity of moving the VNA measurement instrument. This transmit location is still able to be rotated around a fixed point such that it aligned to face the receive antenna. The remote receiver head can be easily moved as it is battery powered and lightweight

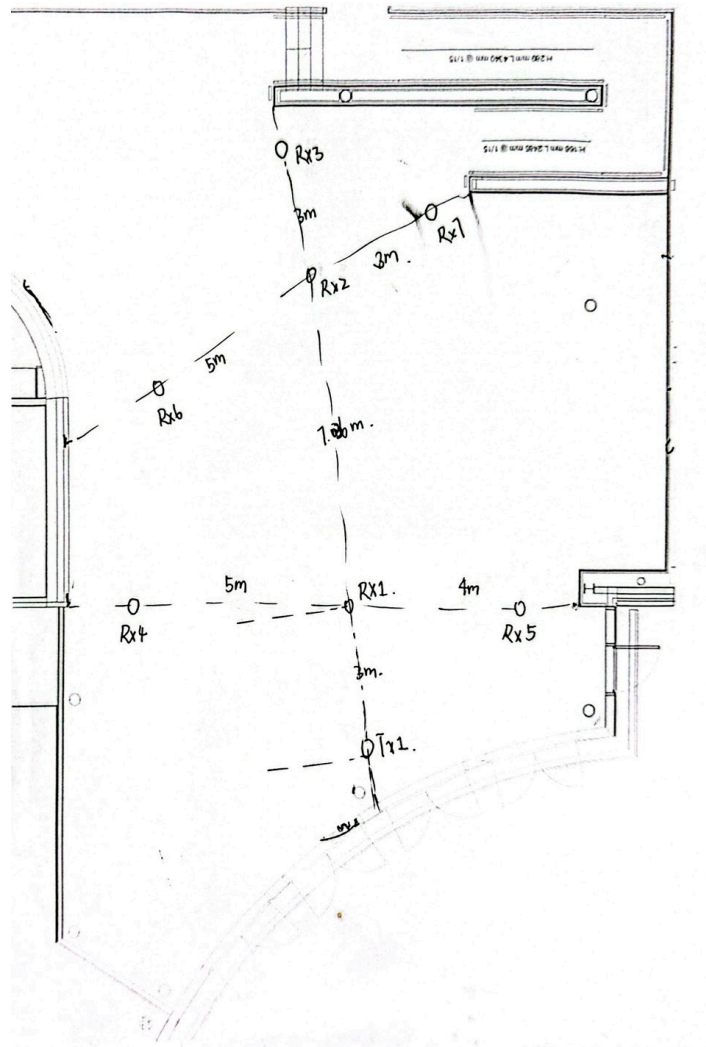


Figure 55: Positions of measurement locations within the NPL Atrium for Tx locations 1 and Rx locations 1 - 7

aiding repositioning. It is the receiver head that is moved between measurement locations, shown in Figure 55 Rx1 - Rx7. Measurement locations were measured using a tape and then marked on the floor to allow repeated measurements with different systems. The antenna is then positioned over the taped mark and alignment is then performed to ensure it is directly facing the transmit antenna.

At the start of each measurement, a system normalisation and check is performed. This is used to remove the effects of the measurement system from the results, as such successful normalisation will remove any phase or attenuation caused by the either the RoF or extender heads. The normalisation is performed to the end of the extender head waveguide test port and is measured for the direct through case with the extender heads directly connected together. This moves the measurement reference plane to the end of the wave guide test port before the antennas are connected. It is currently a limitation of this experimental setup that the antennas are not part of the normalisation. It can be seen in the literature that antenna de-embedding is possible however for the results presented the effects of the antenna are significantly small compared to the measured channel. Normalisation of the phase feedback system is performed simultaneously so that the phase change of the measurement system can be tracked from the time the normalisation was performed. A check of the normalisation is undertaken before measurements commence. The check is performed by measurement of a short (1" or 2") waveguide section that has been well characterised by previous measurements, the post normalisation results are then checked against the catalogue of previous measurements to ensure the system response is accurate. This allows for identification of normalisation errors that tend to come from inaccuracies in the connection of the sub-THz waveguide components.

The measurement system used is the same as the laboratory RoF case presented in 2.4.1.1. This includes the directional VDI waveguide horn antennas, phase compensated RoF system and Keysight PNA.

Results from the Atrium measurement campaign are shown in Figure 56. These figures show the different channel responses for each measurement location. Each figure shows a strong LOS peak that is correlated with the distance between the Tx and Rx locations, increasing in time delay as the separation increases. After this first peak there are additional peaks present in the measured results, which are from the Non-LOS effects such as reflections, scattering and diffraction created by the environmental interaction of the sub-THz signals.

Table 3: Measurement Parameters for the Raceway Scenario

Measurement Parameter	
IF Bandwidth	100 Hz
Points	50,001
Start Frequency	500 GHz
Stop Frequency	750 GHz
Meas. cable length (Coaxial)	100 m
LO cable length (Fibre)	100 m
Channel sounding range	0 m – 60 m
Sweep duration	c. 400 seconds

2.5.1.3 Corridor (Raceway) Raceway, a long, enclosed corridor-like indoor space on the NPL campus primarily designed for movement between laboratories. This environment is chosen for channel sounding measurements for evaluating sub-THz signal propagation in confined, modern indoor settings. The raceway measures approximately 30 meters in length, 2 meters in width, and 3 meters in height, making it representative of a typical high-traffic corridor

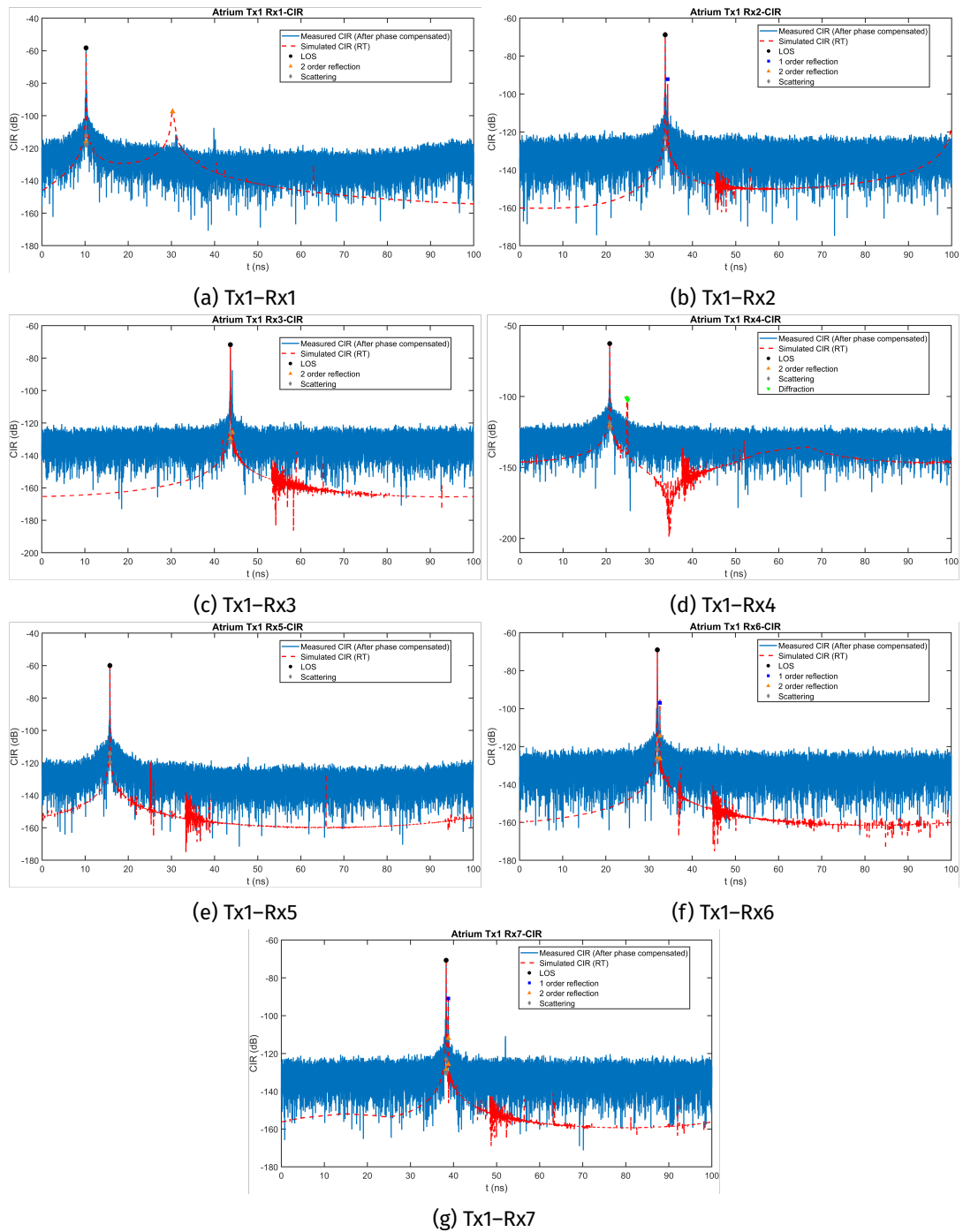


Figure 56: CIRs measured in the NPL atrium with a fixed transmitter (Tx) and the receiver positioned at seven distinct locations. Each figure (a-g) corresponds to a unique receiver position (Rx1-Rx7), showing the CIR observed at that point.

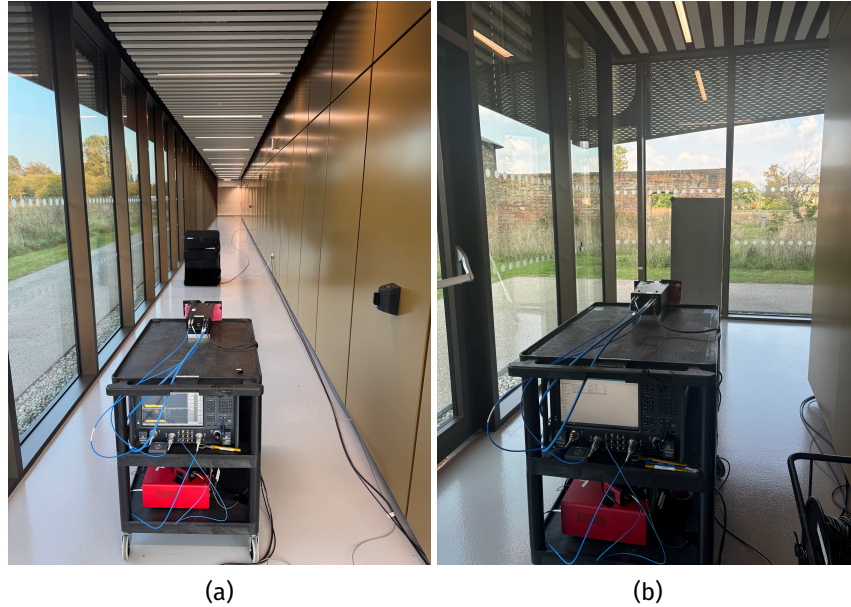


Figure 57: Raceway measurement location with (a) transmit trolley located in position Tx2 and (b) the transmit measurement trolley facing the metal reflector plate

in institutional or commercial buildings. Constructed as part of a recent development around 2020, the space features modern building materials including metallic wall panels, multi-layer double-glazed windows spanning one side of the raceway, and a concrete epoxy-coated floor. The ceiling consists of exposed infrastructure partially concealed by a linear baffle system, which incorporates integrated lighting. The corridor is free from obstructions, with only minimal presence of equipment during measurements to ensure accurate assessment of signal behaviour in a static scenarios. This setting supports realistic propagation environments for high-frequency wireless communication testing, particularly over short- to medium-range distances in line-of-sight and reflective multipath conditions.

The measurement locations in Figure 58 Rx2a – d, represent increasing distances along the corridor, with distances of 5, 10, 20 and 30 meters respectively from the Tx antennas. The Tx and Rx trolleys are located centrally in the corridor and the antennas are aligned so that the Tx and Rx antennas are bore-sight to bore-sight. The Tx2 position is 3 meters from the glass windows behind, along the corridor in the long direction. Transmit position 3, Tx3, is located around the corner to exhibit a Non-LOS case for the propagation channel when the Rx antenna is located at any of the Rx2 positions. For this case, the channel was augmented with and without a metal plate, approximately 0.6x1.3 meters, to provide a reflected path around the corner. The plate was placed at 45° to the Tx antennas directly in the path of propagation.

The measurement process from the atrium measurements was repeated, including normalisation and checking with a waveguide through section. Additionally, the measurement setup was repeated from the atrium measurements, shown in Table 3, although the number of measurement frequency points was increased to allow for a longer channel distance to be assessed, to include longer reflected signal path components. To keep the measurement, sweep period similar to the atrium measurements an increased IF bandwidth was selected. The raceway results in figure 59 show greater multipath components than the results presented for the atrium. This is especially evident for the channel measurements of greater distance such as figure 59c (Rx2c) and 59d (Rx2d). This is attributed to the material properties

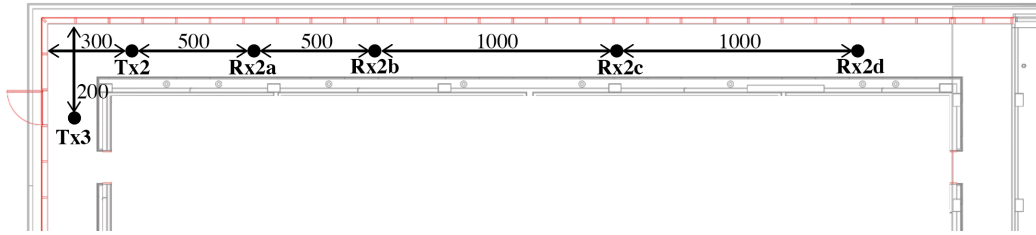


Figure 58: Positions of measurement antennas for the NPL Raceway measurement scenario. Distance in units of centimetres.

of the measured environment; it is expected for there to be significant reflected signal from the metal clad wall panels and possibly the window glass or metal framework. The ceiling design, made of metal plates, will also provide multipath effects shown in the results, due to reflection off the surface and diffraction or scattering from the edges.

In comparison between both the channel measurements 'around a corner' there is significant difference with, (figure 59f) and without (figure 59e) a metal plate. The position of the metal plate greatly aids the reflection of the signal around the corner and provides an approximate 45 dB increase in signal amplitude when it is used. Without the metal plate there are two weak reflected paths around the corner however these are close to the noise floor of the measurement system.

Table 4: Measurement Parameters for the Outdoor Scenario

Measurement Parameter	
IF Bandwidth	300 Hz
Points	100,001
Start Frequency	500 GHz
Stop Frequency	750 GHz
Meas. cable length (Coaxial)	100 m
LO cable length (Fibre)	200 m
Channel sounding range	0 m – 120 m
Sweep duration	c. 00 seconds

2.5.1.5 Outdoor Measurements were performed in an outdoor space, along the footway adjacent to Essen Way on the NPL Campus. This open-air environment offers a relatively uncluttered and extended line-of-sight range up to 100 meters for sub-THz channel sounding measurements. The pavement measures approximately 110 meters in length and 3 meters in width, bordered on one side by a tall red-brick wall and on the other by a wide road surface, shown in figure 60, providing a mix of reflective and absorptive surfaces for multipath analysis. The site features minimal obstructions and is surrounded by mature trees and some low foliage, which contribute to realistic scattering effects typical of semi-urban or landscaped environments. The brick wall introduces periodic shadowing and potential for diffraction, making it ideal for evaluating high-frequency signal behaviour in partially obstructed outdoor corridors.

The test equipment, including channel sounding and measurement apparatus, is deployed on mobile trolleys as seen in the foreground of figure 60a. A temporary blue tent is situated at the far end of the track to support continuous data collection and environmental control. This location enables long-range, controlled outdoor experiments to evaluate signal attenuation and multipath characteristics for future sub-THz wireless systems.

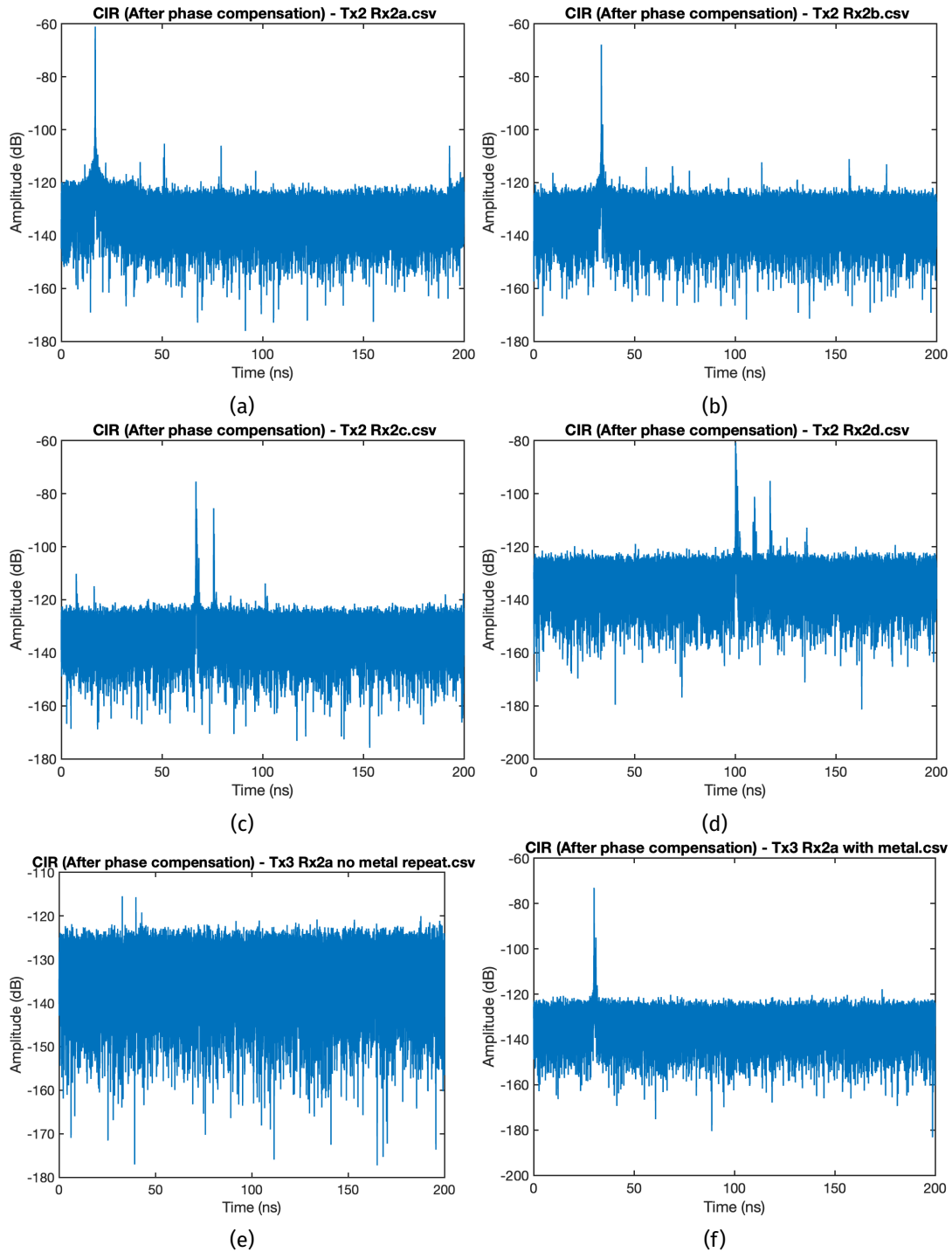


Figure 59: CIRs measured in the NPL Corridor (Raceway) for two transmitter locations (Tx2 - 3) and the receiver positioned at seven locations. Each figure (a-f) corresponds to a receiver position showing the CIR observed at that point. figures (e) and (f) show the same channel with and without a metal reflector plate

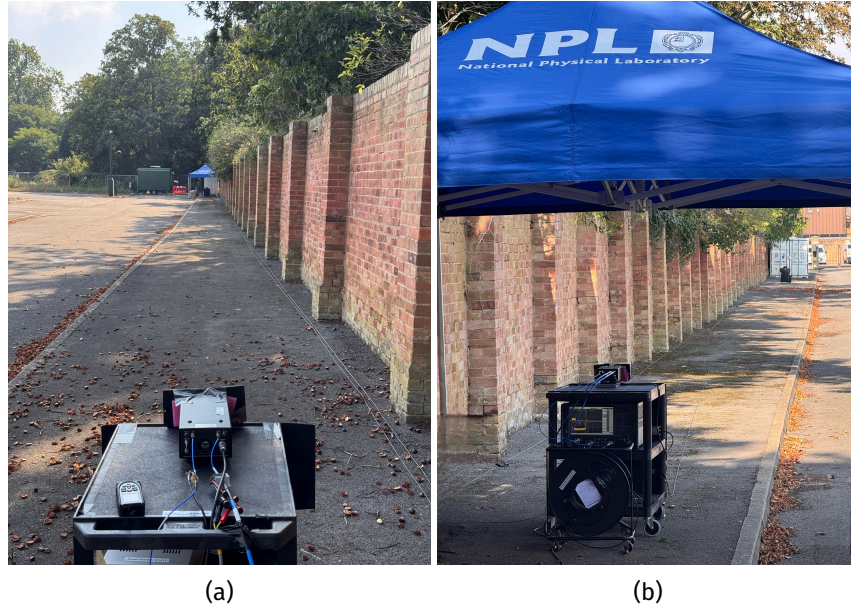


Figure 60: Outdoor measurement location with (a) the receive trolley in the foreground and (b) the transmit trolley in the foreground for the 100 meter separation case.

Four receive antenna measurement positions were used, at 25, 50, 75 and 100 meters separation from the fixed Tx antenna placed near the blue tent are shown in Figure 61.

The same measurement procedure detailed in previous sections was used, including normalisation and checks of a known waveguide through with comparison to previous results. Again, the measurement parameters have been maintained from the previous measurements, however the number of measurement points has been increased to 100,001 to capture channels up to 120 meters. Currently there is a limitation within the Keysight PNA that a single measurement can have up to 100,003 points, limiting the maximum possible distance in a single sweep for the 250 GHz bandwidth. An additional 100 meters of fibre is used, bringing the total to 200 meters of optical fibre within the system. The IF bandwidth is also increased to 300 Hz providing a sweep time of approximately 10 minutes.

As expected, Figure 62 shows as the length of the measured channel increases, the peak of the CIR moves further in time and decreases in magnitude. The measurement at the 100 meter case, figure 62d, exhibits that the increase in attenuation of the channel at these distances is sufficient to bring the LOS signal path within 15 dB of the system noise floor. This limits the ability of the system to identify reflected and other multipath signals as these will be of a lower magnitude than the LOS path and therefore in the system noise. The shape of the peaks at distances of 25, 50 and 75 meters are broadened, this may be due to system non-linearity and inability for the phase compensation mechanism to correct for all phase drifts within the system. The 100 meter measurement was performed first and does not exhibit this effect, although this could be masked by the noise floor. The effect is especially strong due to the long lengths of fibre and outdoor temperature fluctuations affecting not just the fibre but also the extender heads and RF components of the system which are uncompensated. With an increased measurement sweep time, an decreased RF bandwidth can be used which would improve the system dynamic range by approximately 10 dB. Upgraded components may also offer an additional 30 dB dynamic range improvement at this frequency range allowing for measurement of longer lossy channels.

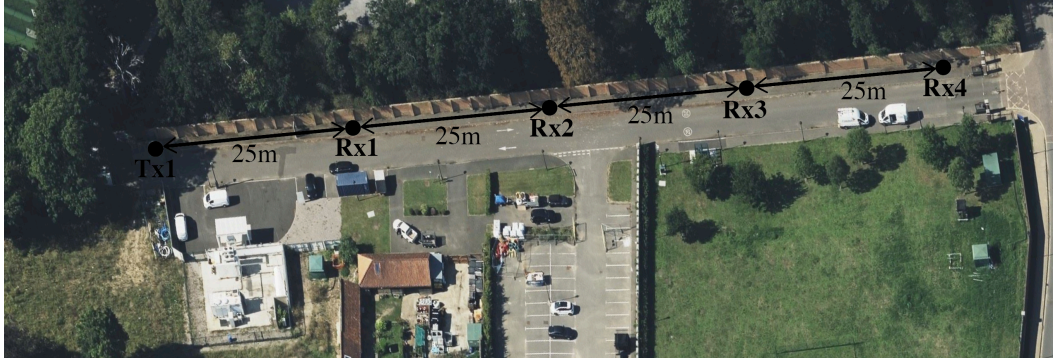


Figure 61: Measurement positions for the NPL outdoor channel sounding case. Each distance is in units of meters.

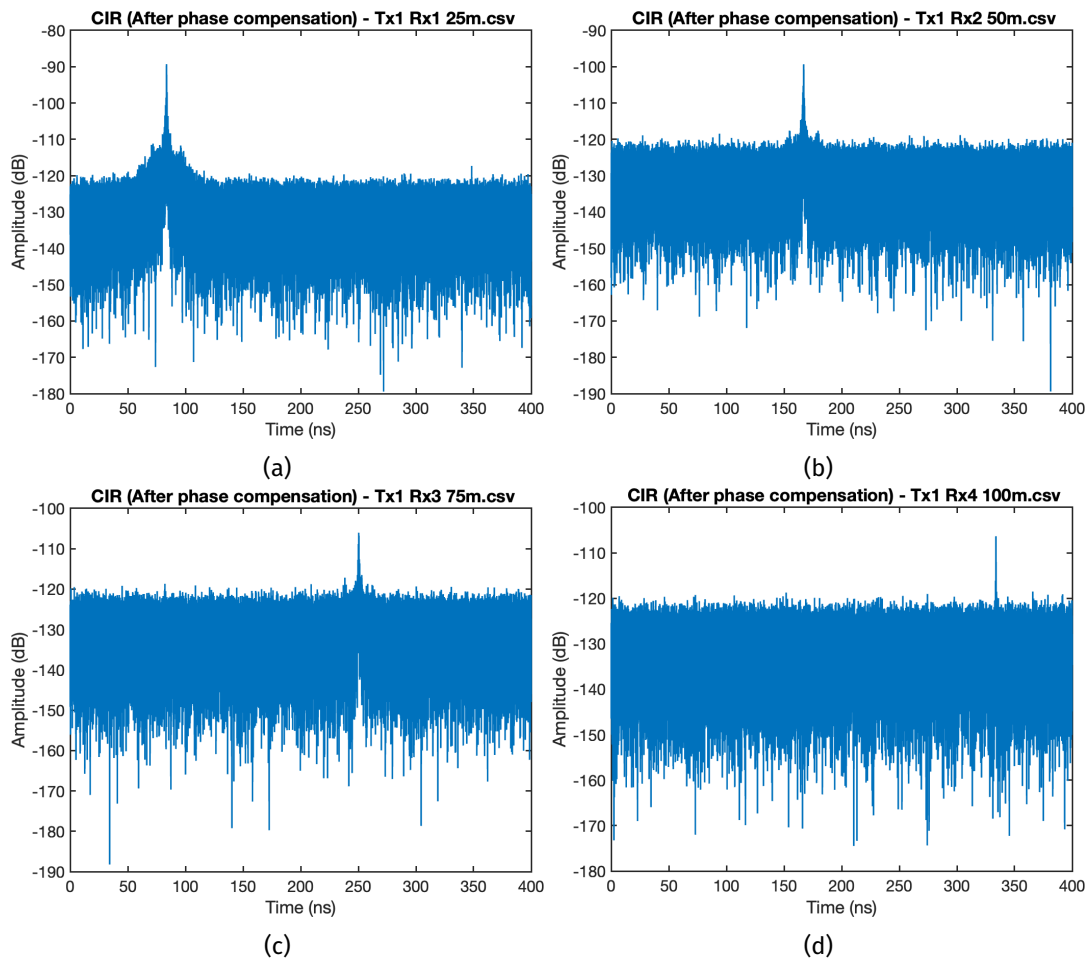


Figure 62: CIRs measured outdoors for one transmitter locations (Tx1) and the receiver positioned at four locations. Each figure (a–d) corresponds to a receiver position showing the CIR observed at that point.

2.5.2 Discussion of practical measurement techniques Table 5 provides a comparison of the components used in both measurement systems operating in the 330–500 GHz and 500–750 GHz bands. The primary difference lies in the use of different frequency extenders for each range. The measurement setups—particularly in the indoor laboratory and atrium environments—were kept identical across both systems. The results show consistent behavior, and successful channel sounding was achieved. In the following sections, ray-tracing analysis will be presented for frequencies up to 750 GHz to support the validation of the measured channel characteristics.

Table 5: Equipment used across different frequency bands

Equipment	330–500 GHz	500–750 GHz
VNA	Rohde & Schwarz /Keysight	Keysight
Frequency Extenders	Rohde & Schwarz ZC500	VDI WR1.5
E/O Converter	Thorlabs MX40G	Thorlabs MX40G
Amplifier 1	ERZ-LNA-1000-2700	Minicircuits ZX60-06183LN+
Amplifier 2	Mini-Circuits ZFL-500L	Mini-Circuits ZFL-500LN
Horn Antennas	SGH-26-WR2.2	DI WM-380
Photo Receiver	Thorlabs RXM40	Thorlabs RXM40
Coaxial Cable	100 m	100 m
Coaxial Cable type	RG58U	RG58U

3. Development of band-stitching algorithm. mmWave 8 × 8 Antenna-in-Package (AiP) Array Platform - experimental validation and applications

3.1 Development of band-stitching algorithm

3.1.1 Enabling High-Fidelity Ultra Wide-band Radio Channel Emulation: Band-Stitching and Digital Pre-distortion (DP) Concepts

3.1.1.1 Introduction The evaluation of the end-to-end performance of wireless devices under realistic propagation conditions is very important. The idea of virtual drive test (VDT) has attracted a significant interest [43], [44], [45]. The main concept behind it is to translate the conventional field testing to a controllable laboratory environment, where either a cable-conducted setup or an OTA radiated setup is used [46], [47]. Radio channel emulator (CE) are the key blocks in the VDT concept [48], [49]. The modern CE have a digital architecture due to the requirement for a high reconfigurability [50], [51], [52], [53]. As new generations of wireless communication technologies develop, wider radio spectra are allocated to obtain higher data rates. For example, the 5th Generation (5G) New Radio (NR) signal may occupy a bandwidth of up to 400 MHz per carrier in the FR 2 [54], which is a significant increase in the bandwidth compared to the 4th Generation (4G) long term evolution (LTE) signals using only 20 MHz bandwidth. However, most of the available commercial CE can support an emulation bandwidth of up to 160 MHz, which poses a limitation on testing radio devices operating with a wider bandwidth.

To enable UWB channel emulation, a band-stitching technique has been proposed in the literature [55], [56], [57], [58]. In that regime, multiple digital channels of a CE, operating at different IF, are utilized together to synthesize a single virtual digital channel of a larger bandwidth. Ideally, the *intrinsic frequency response of each physical digital channel needs to be of raised-cosine*, and the coherence of amplitude and phase between adjacent channels needs to be guaranteed for a perfect band-stitching result. In [56], the effect of a misaligned phase between adjacent channels on the resulting stitched channel is shown, resulting in a huge distortion over the stitched channel. The coherence misalignment can be resolved by careful emulator calibration to some extent. Currently, emulator calibration for band-stitching has been done mostly in a trial-and-error manner [55], [58], i.e., tuning the attenuation (e.g., at 0.1 dB step) and phase shift (e.g., at 1° step) of each digital channel until the flatness of the frequency response of the stitched channel reaches some acceptable tolerance on a VNA. Therefore, even if the entire tuning process is automated, calibration performed in this way can be very time-consuming and its accuracy is limited by the tuning resolution. Moreover, this calibration method does not account for the shape of the intrinsic frequency response of the digital channels if there is a deviation from the ideal raised-cosine. In a recent work [58], the intrinsic frequency response of a commercial CE was observed to have a magnitude variation of ± 1.5 dB and a phase variation of $\pm 15^\circ$ per digital channel over 160 MHz bandwidth, and the variation worsened to ± 3.5 dB and $\pm 30^\circ$ for the stitched channel of 960 MHz bandwidth with the aforementioned calibration accounted.

When performance testing of regular cellular device is needed, fading channels following, e.g., geometry-based stochastic channel models [59], are typically targeted for emulation. It has been evaluated empirically that the additional intrinsic distortion, which is on top of the target fading channel, has only negligible effect on the obtained test results. However, for some static-link communication scenarios, e.g., satellite, aerospace, the target channels are expected to be wide-band and static. Moreover, notches may occur in the channel frequency response due to potential strong reflections in the scenarios. It has been very popular to test those communication links with a notch channel

model, e.g., the Rummler model [60] or the two-ray model, with variable notch frequencies and depths. In this case, a better emulator calibration method is desired, because the notches in the emulated channel will be highly sensitive to the amplitude and phase of the intrinsic frequency response of CEs. Another critical scenario would be the error vector magnitude (EVM) measurements. In this particular case, the intrinsic distortion of emulators needs to be low enough so that it does not make the true EVM of devices under test uncertain. In the open literature, there are not any reported solutions on mitigating the intrinsic distortion introduced by CE, which is of importance for achieving high-fidelity UWB channel emulation.

The work in [61] serve as a basis for this subchapter. A novel DP scheme for CEs for achieving high-fidelity UWB channel emulation is proposed. The proposed technique is based on the minimum mean square error (MMSE) equalization. Measuring the intrinsic frequency responses of the CE can be used for pre-distortion of the target channel profile accordingly so that the total response of the emulated channel matches the intended target channel with a higher accuracy. This is especially important for the band-stitching process, because the proposed method regulates the effective intrinsic responses of the emulator to be the desired raised-cosine, which is a big advantage compared to the conventional calibration methods. However, the pre-distorted channel coefficients may result in more taps than the maximum number of taps available in a CE. Therefore, a possible solution to derive the pre-distorted channel coefficients under the limitation of the tap resources of CEs is suggested.

3.1.1.2 Band-stitching with CEs Figure 63 presents a general schematic diagram of stitching two digital channels of a CE into a single virtual digital channel having wider bandwidth for the Single-Input Single-Output (SISO) case.

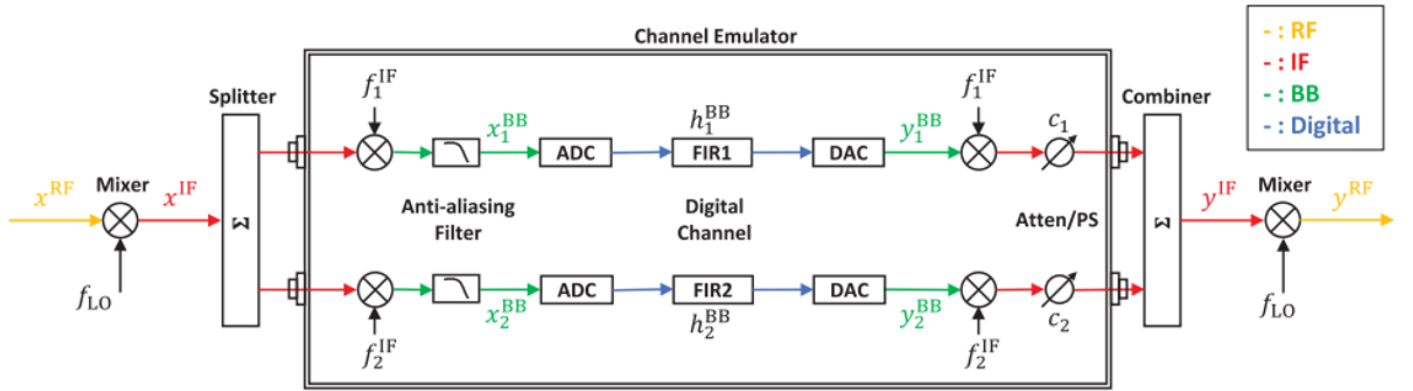


Figure 63: Schematic diagram of stitching two sub-bands for a SISO system

The mixer down-converts the RF input signal x^{RF} to the IF signal x^{IF} with the LO frequency f_{LO} . The IF signal x^{IF} is split into two identical streams, as each stream is further mixed down to baseband (BB) with its individual sub-band center frequency f_1^{IF} and f_2^{IF} respectively. The BB signal of each sub-band, x_1^{BB} and x_2^{BB} , is filtered by using the anti-aliasing filter and then it is converted to discrete baseband signal in the Analog-to-Digital Converter (ADC). Afterwards, the discrete baseband signal convolves with the emulated channel, h_1^{BB} and h_2^{BB} , generated according to the target channel model, in the finite impulse response (FIR) filter. The signal of each digital channel is converted to analog through the Digital-to-Analog Converter (DAC) and then it is up-converted back to its respective IF. The combiner stitches the two streams back to one, which is lastly up-converted to RF to form the RF faded signal y^{RF} over the stitched band.

The variable attenuators and phase shifters (Atten/PS) are used to change the relative amplitude and initial phase, c_1 and c_2 , between the two branches for calibration.

The digital channel of each branch can be seen in a simplified way as a single FIR filter. It is composed of a set of cascaded FIR filters, namely an input filter, a fading channel filter, and an output filter. The input filter is an all-pass filter with a pre-configured bandwidth (relative to the ADC sampling rate) used to suppress potential out-of-band signals for further processing. The fading channel filter is one generating the target channel for emulation by specifying tap delay indices and associated tap coefficients according to the target channel impulse responses. The output filter is also low-pass filter with a pre-configured bandwidth suppressing any out-of-band signals before the DAC. Typically, the fading channel filter is the configurable by the users, while the other two filters are preset by the emulator vendors and hidden to the users. The reader can refer to equations (1)-(5) in [61] presenting the mathematic relationships for the different impulse responses.

3.1.1.3 Digital pre-distortion - an alternative calibration and fading method The calibration method can be represented as an equalization problem, and eq. (9) in [61] shows that the frequency-domain representation of the impulse response can be solved with the MMSE method. A numerical example of the equalization is presented in Figure 64.

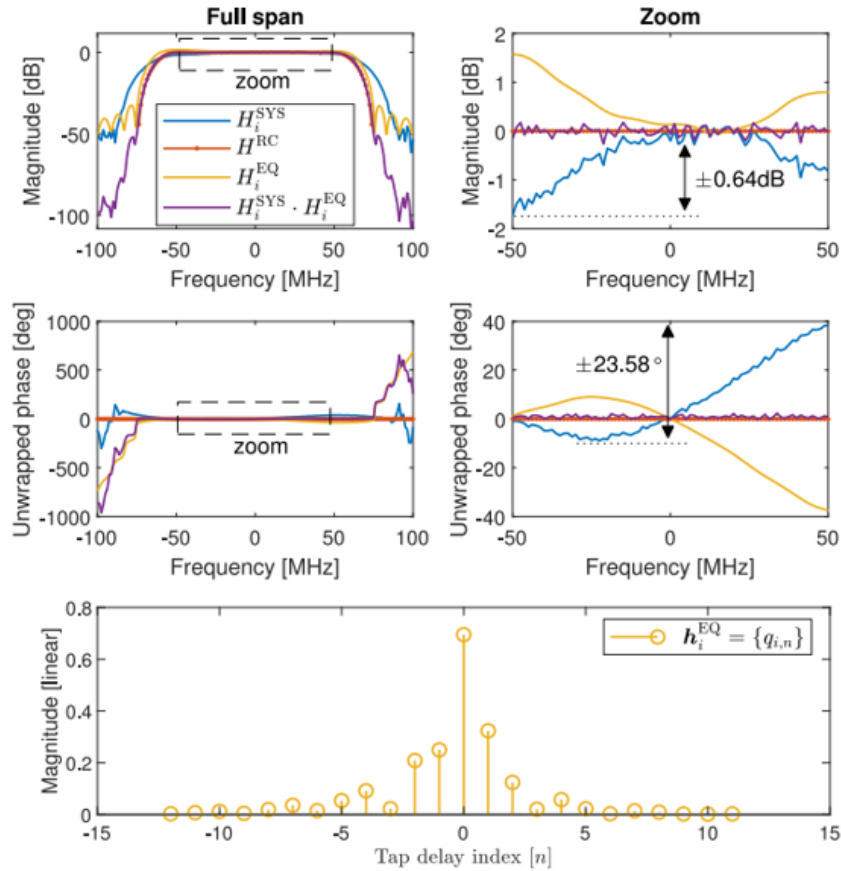


Figure 64: An example of the equalization for a measured system response $H_i^{SYS}(f)$ of a commercial CE. $H_i^{RC}(f; T, \beta)$ denotes the target raised-cosine, $H_i^{EQ}(f)$ denotes the frequency response of the equalization filter, and $H_i^{SYS}(f) \cdot H_i^{EQ}(f)$ denotes the effective intrinsic system response after the equalization. h_i^{EQ} denotes the vector of the tap coefficients of the equalization filter

The figure shows the magnitude and phase of the frequency response of a measured $H_i^{SYS}(f)$, a target $H^{RC}(f; T, \beta)$, the resultant $H_i^{EQ}(f)$, and the product $H_i^{SYS}(f) \cdot H_i^{EQ}(f)$. For this example, a 24-tap equalization filter is used. The resultant tap coefficients are shown at the bottom of Figure 69. The system response $H_i^{SYS}(f)$ was measured for a commercial CE (Propsim F8). The clock rate of the digital channel was 200 MHz, resulting to 5 ns tap delay interval. The parameters of the raised-cosine were $\frac{1}{T} = 125$ MHz and $\beta = 0.2$. The settings correspond to a distortion-free bandwidth of 100 MHz, denoted as “Zoom” in the figure. Within this bandwidth, there is a magnitude variation of ± 0.64 dB and a phase variation of $\pm 23.58^\circ$ before the equalization. However, the variations are significantly reduced after the equalization to ± 0.25 dB and $\pm 1.28^\circ$, respectively. There is a much larger deviation between the $H_i^{SYS}(f)$ and the $H^{RC}(f; T, \beta)$ in the transition frequency band. Those large deviations in the transition band violate the odd symmetry for the band-stitching process, and lead to a deteriorated intrinsic frequency response of the stitched channel.

The fading channel filter for both the equalization purpose and the target channel emulation can be utilized by convolving the coefficients of the target channel with the obtained equalization coefficients, and then set that to be the new target channel to emulate in the fading channel filter. This is referred to as the DP process. Equations (11) and (12) in [61] express the impulse response of the new target channel.

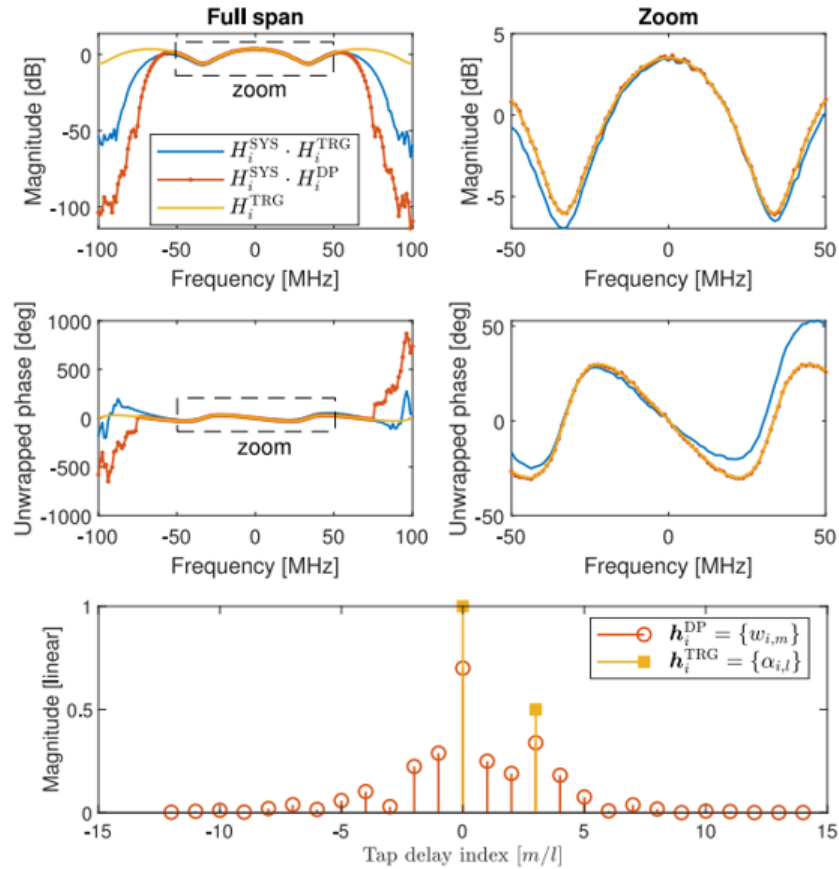


Figure 65: An example of the pre-distortion for a target channel $H_i^{TRG}(f)$ with the resultant pre-distorted channel coefficients. $H_i^{SYS}(f) \cdot H_i^{TRG}(f)$ denotes the emulated channel without the pre-distortion, and $H_i^{SYS}(f) \cdot H_i^{DP}(f)$ denotes the emulated channel with the pre-distortion. h_i^{TRG} denotes the vector of the tap coefficients of the original target channel, and h_i^{DP} denotes that of the fading channel filter with the pre-distortion method

3.1.1.4 Digital pre-distortion for band-stitching

Figure 65 presents a numerical example of the pre-distortion including the magnitude and phase of the frequency response of a band-unlimited target channel, $H_i^{TRG}(f)$, the emulated channel without pre-distortion, $H_i^{SYS}(f) \cdot H_i^{TRG}(f)$, and that with pre-distortion, $H_i^{SYS}(f) \cdot H_i^{DP}(f)$. The target channel is a two-ray channel with a delay difference of 3 tap intervals, i.e., 15 ns, and a power ratio of 3 dB between the two rays. With the 100 MHz distortion-free bandwidth, there is a large deviation of the magnitude and the phase for the case without pre-distortion with respect to the target channel, whereas only negligible deviation for the case with pre-distortion.

In the next example, we consider stitching two digital channels of a CE (Propsim F8) into a signal virtual digital channel of a larger bandwidth operating at the center frequency of 28 GHz. The target for each branch is the raised-cosine with parameters $\frac{1}{T} = 125$ MHz and $\beta = 0.2$ corresponding to a 225 MHz distortion-free bandwidth for the stitched channel. The system setup is the same as in Figure 63. An analog signal generator creates a LO signal with a frequency of 33.1 GHz, resulting in an IF frequency of 5.1 GHz after the external mixer. The center frequencies of the two branches are set to $f_1^{IF} = 5.1625$ GHz and $f_2^{IF} = 5.0375$ GHz respectively so that $|f_1^{IF} - f_2^{IF}| = \frac{1}{T}$. VNA measures from 27.5 GHz to 28.5 GHz with 801 frequency samples the intrinsic frequency response of each branch, i.e., $H_1^{RF,cal}(f)$ and $H_2^{RF,cal}(f)$. Figure 66 shows the magnitude and phase frequency response of the stitched channel from the conventional method.

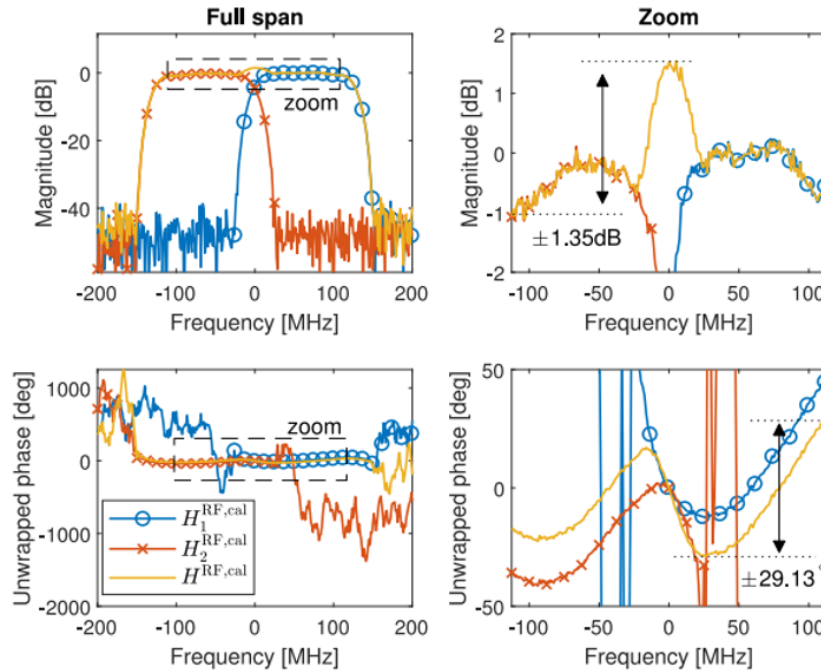


Figure 66: The measured intrinsic responses $H_i^{RF,cal}(f)$ and $H^{RF,cal}(f)$ of a CE for band-stitching with the conventional calibration method. $H_1^{RF,cal}(f)$ and $H_2^{RF,cal}(f)$ denote the frequency responses of the higher and lower sub-bands, respectively. $H^{RF,cal}(f)$ denotes the frequency response of the stitched channel

The center 225 MHz band of the measurement is the targeted distortion-free band of the stitched channel denoted as “Zoom”, while the center 400 MHz band of the measurement is denoted as “Full span”. Within the distortion-free band, there is a variation in the magnitude of ± 1.35 dB and a variation in the phase of $\pm 29.13^\circ$ for the stitched channel. Compared to the single band case (shown in Figure 68), the increased values for the variations are caused mostly by the intrinsic response of each branch in the transition band being different from the targeted raised-cosine.

Applying the equalization procedure to both branches will lead regulation of the intrinsic response of each branch to the targeted raised-cosine, and the equalized intrinsic response of each branch and the resultant stitched channel are shown in Figure 67).

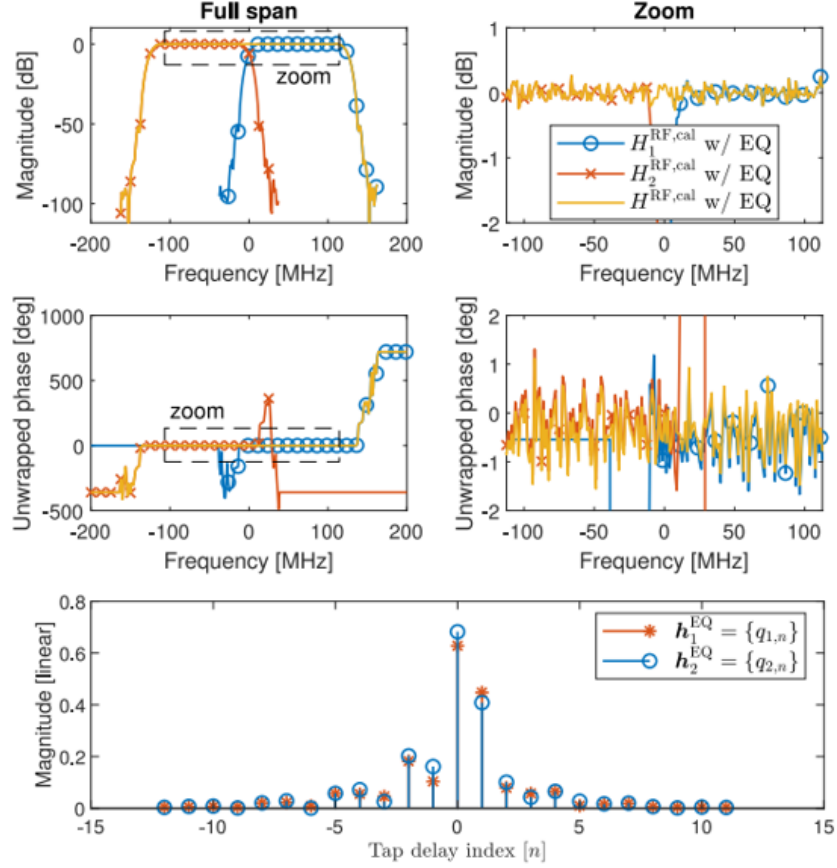


Figure 67: The equalized intrinsic frequency responses $H_i^{RF,cal}(f)$ and $H^{RF,cal}(f)$ of a CE for band-stitching with the equalization method. $H_1^{RF,cal}(f)$ and $H_2^{RF,cal}(f)$ denote the frequency responses of the upper and lower sub-bands, respectively. $H^{RF,cal}(f)$ denotes the frequency response of the stitched channel

The magnitude and phase variations are significantly decreased to ± 0.26 dB and $\pm 1.34^\circ$, respectively, which are both one order of lower than that when using the conventional method. The equalization coefficients for both branches are shown at the bottom in Figure 67). In order to emulate the target channel in the band-stitched virtual digital channel of 225 MHz bandwidth, the target two-ray channel is pre-distorted with the respective equalization coefficients of each branch. The resultant frequency responses of the emulated channel with the conventional calibration method and with the DP method are shown in Figure 68).

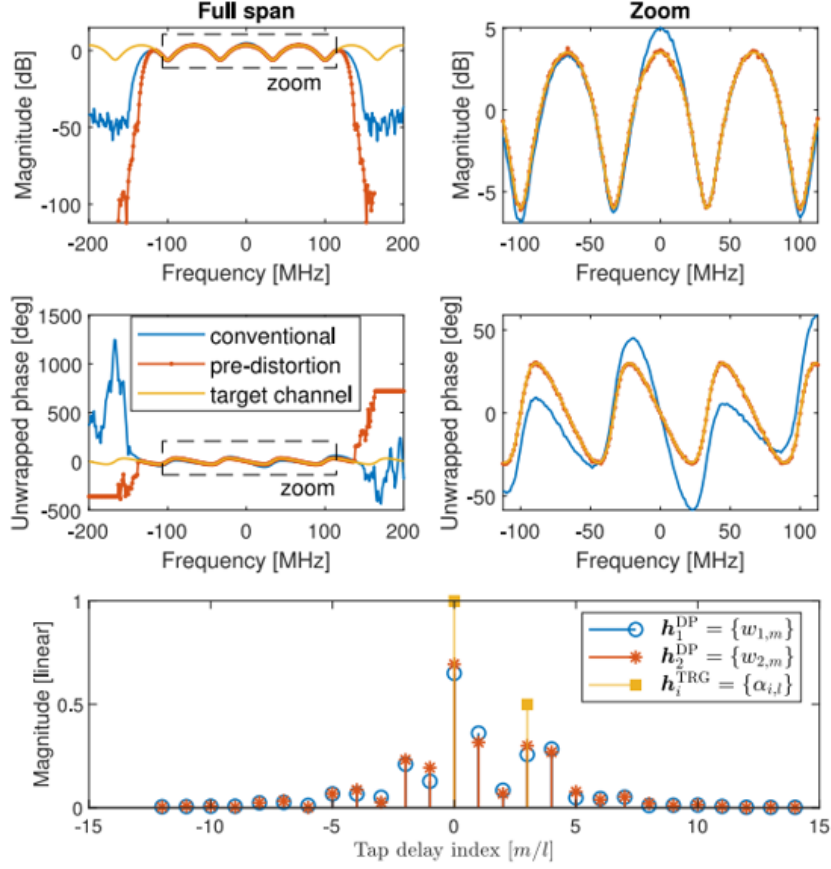


Figure 68: The frequency responses of the emulated channel over the stitched band with the conventional calibration method and the DP method. h_i^{TRG} denotes the vector of the tap coefficients of the original target channel, and h_1^{DP} and h_2^{DP} denote the vector of the tap coefficients of the fading channel filter with the pre-distortion method for the upper and lower sub-bands, respectively

Serving as a reference, the band-unlimited frequency response of the target two-ray channel is also shown. In terms of both magnitude and phase deviations, the result from the pre-distortion method clearly outperforms that from the conventional method. The pre-distorted coefficients h_1^{DP} and h_2^{DP} for the two branches are presented at the bottom of Figure 68). The considered two-ray channel can be emulated with high fidelity over a roughly doubled bandwidth by loading $[h_1^{DP}, \tau_1^{DP}]$ and $[h_2^{DP}, \tau_2^{DP}]$ to the corresponding fading channel filters of a CE. High-fidelity ultra-wideband emulation can be implemented by using the same principle and extending for band-stitching with more digital channels.

3.1.1.5 Conclusion In this subchapter, the conventional calibration method for the band-stitching for ultra-wideband channel emulation is explained. However, to overcome its disadvantage of reshaping the intrinsic response of each sub-band to raised-cosine, a DP method is proposed by exploiting the user-accessible fading channel filter in the CE. The suggested technique can be explained as the convolution between the original target fading channel and an equalization filter, where the raised-cosine is set as the equalization target. The coefficients of the equalization filter were solved with the MMSE method. The proposed method is realized by using an extra number of taps of the fading channel filter, which is a limited resource of a CE.

The original target fading channel and the raised-cosine were considered as a whole as the equalization target and the equalization coefficients were calculated over the confined taps in order to limit the number of taps of the resultant pre-distorted channel coefficients. The resultant equalization coefficients correspond directly to the final pre-distorted channel coefficients. The proposed method and the conventional method were numerically evaluated with the measured intrinsic responses of a commercial CE for a two-band stitching scenario. As the figure of merit for the band-stitching performance, the variations of the magnitude and phase were used. It was found that for the conventional method, the variations of the magnitude and phase were ± 1.35 dB and $\pm 29.13^\circ$, compared to ± 0.26 dB and $\pm 1.34^\circ$ for the proposed method.

3.1.2 On Band Stitching for Wideband Vector Measurements With Vector Signal Analyzers

3.1.2.1 Introduction It is stated in the standard [62] of the 3GPP that each carrier of the 5G NR signal in the Frequency Range 2 (FR2) could occupy a bandwidth of up to 400 MHz per carrier, compared to only 20-MHz bandwidth per carrier for 4G LTE system. While the wider bandwidth increases significantly the throughput of the communication systems, it sets also a challenging task for the measurement instrumentation utilized for the development or testing. In the case of vector measurements, such as waveform or demodulation measurements, the analysis bandwidth of the instrument needs to be wider than the bandwidth of the input signal. However, with the increase of the bandwidth of signals, the analysis bandwidth of many existing commercial instruments becomes insufficient. To address this problem, several measurement bandwidth extension methods have been proposed in [63], [64], [65], [66], [67], [68], [69], [70]. The proposed solution enable instruments of insufficient bandwidth to be utilized without any hardware modification. Those methods can be divided into two groups, i.e., time-interleaved methods [64] and frequency-interleaved methods [66], [67], [68], [70].

The work in [71] is used as a basis for the content in this subchapter. The band stitching, which is the fundamental principle in use, is discussed initially. It was widely used in other applications, where bandwidth extension is considered, such as channel sounding [72], channel emulation [55], [58], and signal generation [73]. The general procedure of band stitching for vector measurements involves several steps as follows: 1) spectrum division; 2) sub-band sampling; 3) interpolation and mixing; 4) sub-band impairments calibration; and 5) sub-band stitching. Depending on whether the first two steps the spectrum division and the sub-band sampling are done sequentially or simultaneously for all sub-bands, the practical measurement setup can be configured in a sequential structure [65], [66], or a parallel structure [67], [68], respectively. The different sub-band data are recorded typically separately either in time (the sequential case) or at different branches (the parallel case), timing, magnitude, and initial phase impairments in recorded sub-band data may exist. The key element in recovering the original signal is the precise estimation of the sub-band impairments. For more general input signals, the timing correction is mostly resolved through either circular cross correlation or trigger signals among different sampling branches [65], [67], [68], [69]. However, these methods do not ensure an accurate estimate for the timing impairment. Therefore, estimation methods with higher accuracy are needed. Afterwards, both the sequential and the parallel setup with vector signal analyzers (VSAs) are discussed. The advantages and disadvantages of both setups are analyzed. For the timing correction, a two-step delay estimation method, which combines the common circular cross correlation and an additional refining step is proposed.

3.1.2.2 Setups and planning

Figure 69) shows both setups.

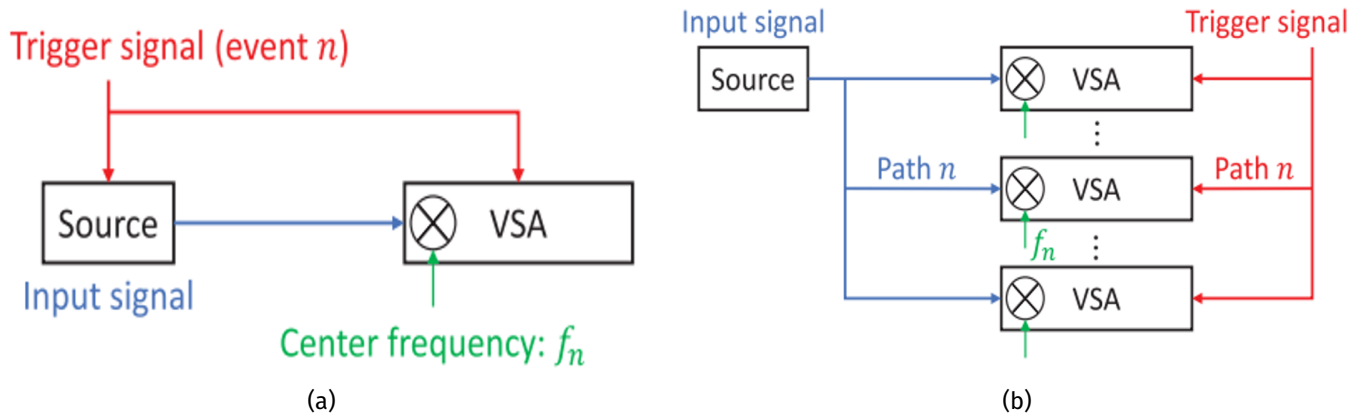


Figure 69: Diagrams of a) sequential setup and b) parallel setup. The center frequency of the VSA of the n th trigger event or the n th sampling branch is denoted as f_n

Figure 69a) presents the sequential setup. As it is visible it requires only one VSA in the measurement. A common trigger signal is used to control the transmission of the signal source and the reception of the VSA. Every time when a trigger event occurs, the signal source replays the input signal from the beginning. Let's suppose that the spectrum of the input signal is divided to N sub-bands. During the n th trigger event, the center frequency of the VSA, f_n , is set to the center frequency of the n th sub-band. Then, the in-phase and quadrature (I/Q) data of that sub-band are recorded. The parallel setup is presented in Figure 69b), and it is composed of multiple VSAs conducting parallel recording in a simultaneous manner. The number of VSAs is equal to the number of sub-bands. Likewise in the previous setup, the reception of all VSAs is controlled by a common trigger signal. The center frequency of the VSA at the n th sampling branch, f_n , is set to that of the n th sub-band. One trigger event is required to capture the I/Q data of all sub-bands, because different sub-bands are recorded at their respective sampling branches in the same time. It is recommended that the VSAs and signal source are locked to the same reference frequency, e.g., through a 10-MHz signal, to minimize any carrier frequency offset for both setups. If this is not the case, then the carrier recovery may be needed for each sub-band. In comparison to the parallel setup, the sequential setup has the advantage of a much lower cost of the system cost, because only one VSA is used in the measurement. However, the measurement with the sequential setup takes N times longer than that for the parallel setup.

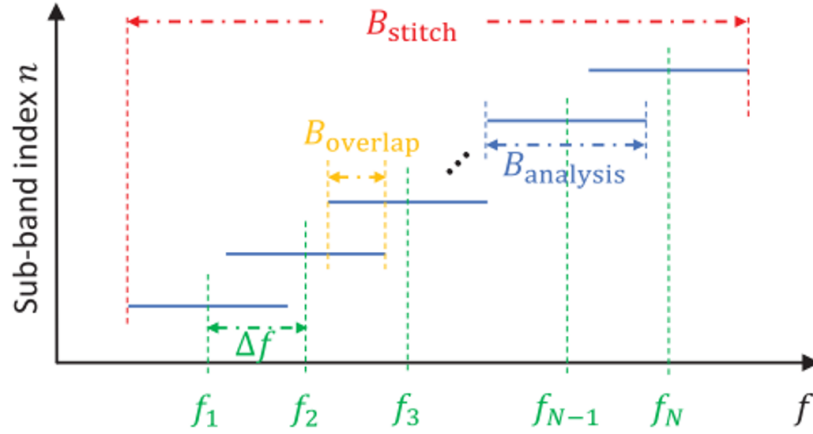


Figure 70: Diagram of the relations among sub-bands. The n th sub-band is centered at f_n with the analysis bandwidth of $B_{analysis}$. The spacing between the center frequencies of adjacent sub-bands is Δf . The overlap bandwidth between adjacent sub-bands is $B_{overlap}$. The total stitched bandwidth is B_{stitch}

Figure 70) shows a diagram of the relations of the individual sub-bands and the total stitched band. It is visible that all sub-bands have a bandwidth equal to the analysis bandwidth $B_{analysis}$. The spacing between the center frequencies of the adjacent sub-bands is Δf for all sub-bands. The input signal is first filtered by the analysis filter of the VSA [74]. The analysis filter can be seen as an effective filter that includes the total filtering, e.g., at the IF analog filter, the anti-aliasing filter, and so on. The bandwidth of the analysis filter is $B_{analysis}$ and it is often referred to as the analysis bandwidth in instrument manuals [74]. $B_{analysis}$ determines the bandwidth within which the spectrum of the raw input signal can be recorded approximately without distortion, i.e., $H_{analysis}(f) \approx 1$ within the analysis bandwidth. The value of the analysis bandwidth is usually scaled to the sampling rate of the VSA by a factor of 0.8 [74]. For instance, if the sampling rate is 100 MHz, then the corresponding analysis bandwidth is 80 MHz. The reader can refer to equations (1)-(2) in [71], showing the relations between the different frequency bands.

3.1.2.3 Sub-band impairment correction The timeline of the recording of two sub-band signals is presented in Figure 71.

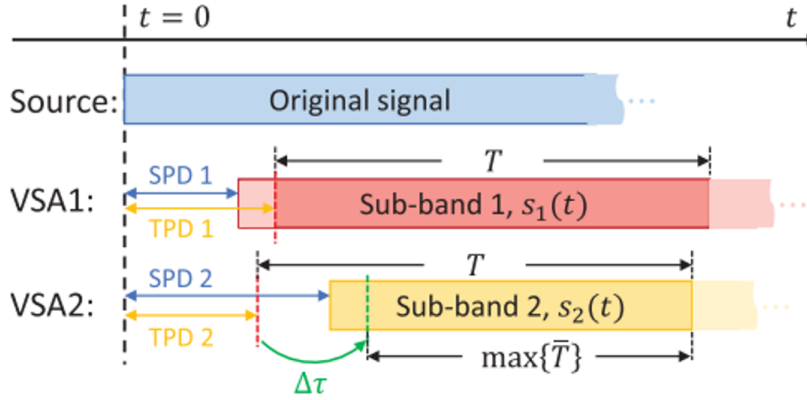


Figure 71: Timing impairments between sub-bands with respect to the original signal for a two-band-stitching scenario. The input signal arrives at each VSA after a sampling path delay. Each VSA starts recording after a triggering path delay, indicated with the red dashed line. The recording duration is T for both VSAs. The green dashed line indicates a virtual start of recording after delay $\Delta\tau$ correction. The recoverable duration of the data is \tilde{T} with a maximum value of $\max\{\tilde{T}\} = T - |\Delta\tau|$.

The three types of impairments are estimated with the recorded sub-band I/Q signals in the overlap band. We assume that when there is no impairment, the signals of adjacent sub-bands in the overlap band shall be about the same if noise is not taken into an account. Recall that $H_{analysis}(f) \approx 1$ in the overlap band. We will consider the parallel setup in Figure 69b) and let's suppose a common trigger signal is sent to both VSAs. Owing to the potential different lengths of the sampling paths, triggering paths, or jitters, the starting of recording of the two VSAs (see Figure 71) may not necessarily coincide at the same position relative to the beginning of their respective sub-band signals. This timing impairment from various sources can be identified as a delay offset, $\Delta\tau$ (between the recorded data of the two sub-bands). Equations (3)-(6) in [71] give the relations between the $\Delta\tau$ and the spectrum of the signals.

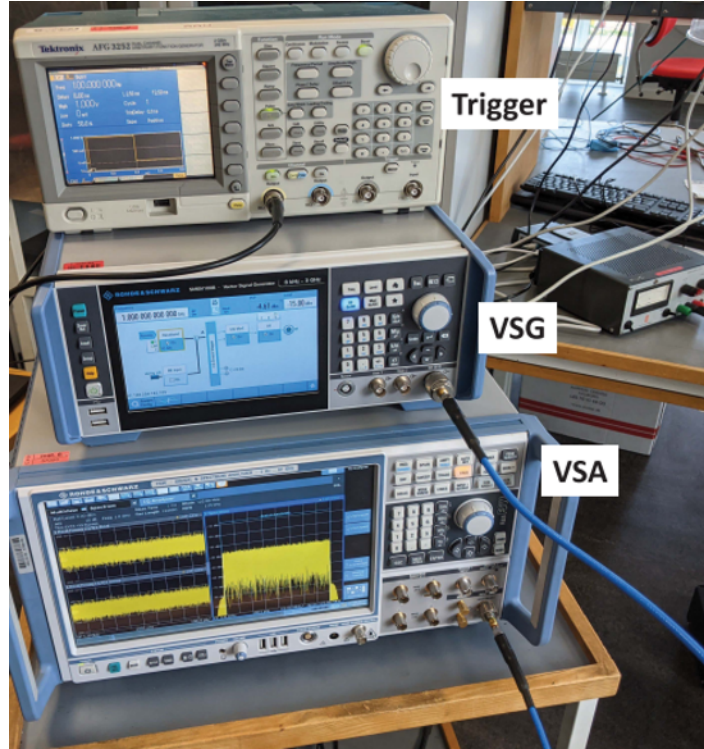


Figure 72: Photos of the measurement setup

3.1.2.4 Validation measurements Table I in [71] represents the general details about the conducted measurements, while the settings of the sub-band measurements for the individual band-stitching cases are given in Table II in [71]. A photos of the measurement setup is presented in Figure 72. An example of the measured I/Q converted to the frequency domain is presented in Figure 73 for the B1 and B3 cases of Series 1, i.e., the conventional full-bandwidth measurement case and the three-band-stitching cases.

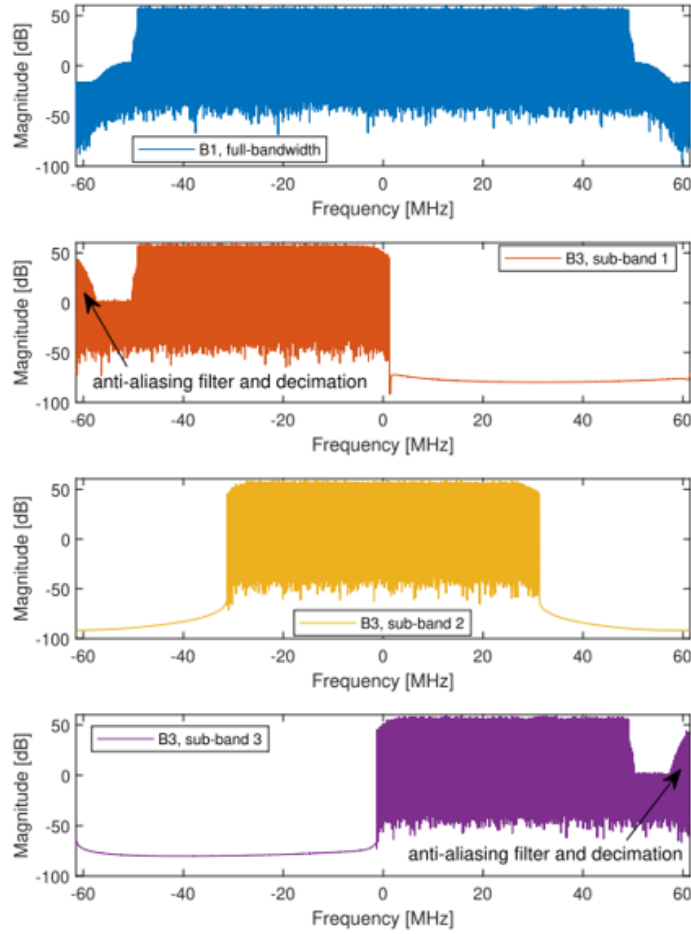


Figure 73: Measured I/Q converted to the frequency domain. Each sub-band I/Q of the B3 case has been interpolated to 122.88-MHz sampling rate and mixed to their respective IF frequencies, i.e., -30 MHz, 0 Hz, and 30 MHz

Each sub-band I/Q of the B3 case has been interpolated from its recording sampling rate, 62.5 MHz, to the target sampling rate 122.88 MHz, and further mixed to their respective IF center frequencies, i.e., -30, 0, and 30 MHz. The small frequency components on the very left-hand and right-hand sides of the “sub-band 1” and “sub-band 2” are caused by the anti-aliasing filter and decimation of the VSA while recording the I/Q data. We can see the envelopes of the three sub-bands, if superimposed, follow that of the B1 case within the channel bandwidth.

The same example (the B3 case of Series 1) showed in Figure 73 is taken for the illustration. The impairment estimation and correction are done over the 20-MHz overlap frequency band between adjacent sub-band I/Q. The initial and refined delays between “sub-band 1” and “sub-band 2” are estimated to be $\Delta\tau' = 1 \cdot \delta_\tau$ and $\Delta\tau' = 0.03 \cdot \delta_\tau$ with $\Delta\tau' = 1/122.88 \mu\text{s}$. Between “sub-band 2” and “sub-band 3,” the delay estimates are $\Delta\tau' = 1 \cdot \delta_\tau$ and $\Delta\tau' = 0.18 \cdot \delta_\tau$. The phase alignment in the two overlap frequency bands is shown in Figure 74 for the cases without delay correction, with the initial delay correction, and with the refined delay correction.

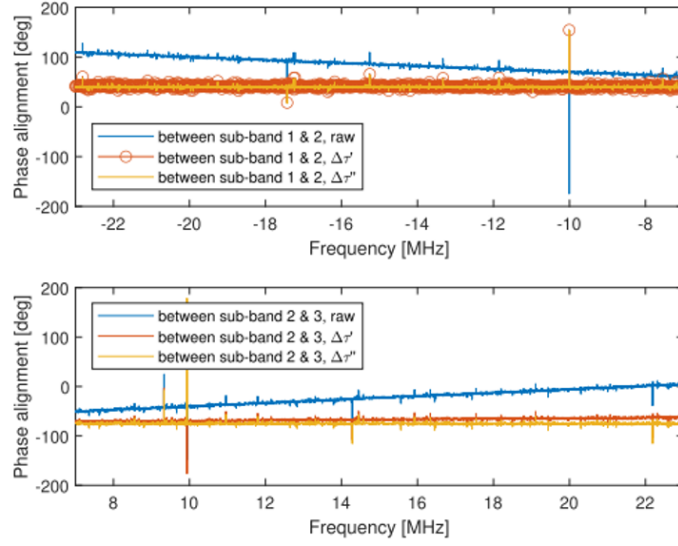


Figure 74: Phase alignment in the overlap frequency band between the adjacent sub-band I/Q, i.e., (top) between “sub-band 1” and “sub-band 2,” and (bottom) between “sub-band 2” and “sub-band 3.” Three cases are shown, i.e., the phase alignment without any delay correction (raw), that with the initial delay correction ($\Delta\tau'$), and that with the refined delay correction ($\Delta\tau''$)

We can see a clear improvement in the alignment with the initial delay correction, and that of the refined delay correction seems marginal. The initial phase offset is estimated from the phase alignment with the refined delay correction, and it is $\Delta\phi = 39.92^\circ$ between “sub-band 1” and “sub-band 2” and $\Delta\phi = -74.83^\circ$ between “sub-band 2” and “sub-band 3.” Similarly, the magnitude alignment in the two overlap frequency bands is shown in Figure 73.

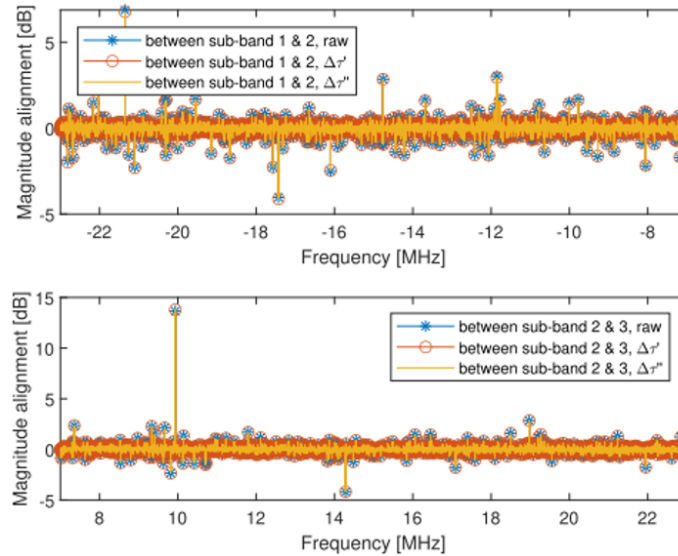


Figure 75: Magnitude alignment in the overlap frequency band between the adjacent sub-band I/Q, i.e., (top) between “sub-band 1” and “sub-band 2,” and (bottom) between “sub-band 2” and “sub-band 3.” Three cases are shown, i.e., the magnitude alignment without any delay correction (raw), that with the initial delay correction ($\Delta\tau'$), and that with the refined delay correction ($\Delta\tau''$)

No significant difference among the three cases is seen, which is reasonable, since the estimated delay offsets between adjacent sub-bands are relatively small. The estimated magnitude offsets in the linear scale are $\Delta\alpha = 0.9986$ between “sub-band 1” and “sub-band 2” and $\Delta\alpha = 0.9995$ between “sub-band 2” and “sub-band 3,” which indicates that the magnitude offsets between the adjacent sub-bands are almost negligible.

A summary of the estimated delay, initial phase, and magnitude offsets for all three repetitions of the B3 case of Series 1 is given in Table III in [71]. We can see that the estimated delay offsets ($\Delta\tau'$ and $\Delta\tau''$) for all three repetitions remain relatively small, i.e., within two delay resolutions. Besides, an interesting observation is that the estimated initial phase offset $\Delta\phi$ changes over the repetitions under the condition that the signal generator and the VSA were locked to the same 10-MHz reference frequency during the measurement, which indicates that the impairment correction is probably needed every time a new band-stitching measurement is conducted.

From the EVM evaluation point of view, it is specified in the standard [75] that the EVM is evaluated over a complete one-frame signal from its frame head. Therefore, we stitch the I/Q data for a two-frame duration to ensure that there exists at least one complete frame of the signal within the stitched duration. Moreover, we generate a frame of the golden I/Q data for the considered “NR-FR1-TM3.1a-FDD-100 MHz–30 kHz” signal according to the standard [75], [76]. Both the I/Q data of the B1 and B3 cases are time and power aligned to the golden I/Q data, and a segment of 1- μ s duration of the aligned I/Q data is shown in Figure 76 in terms of the real and the imaginary part, respectively. No significant differences among the three datasets are seen.

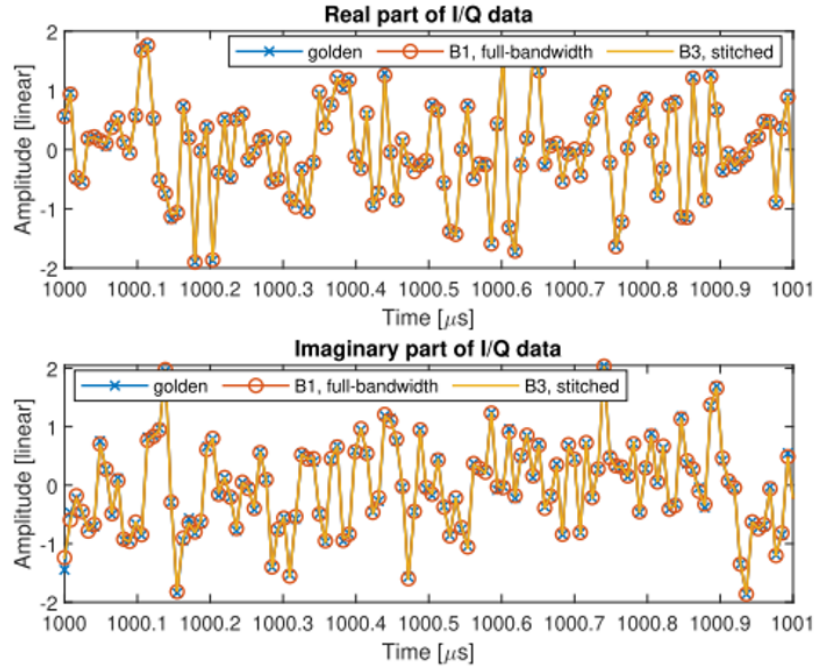


Figure 76: Real part (top) and the imaginary part (bottom) of the golden I/Q data and that of the B1 and B3 cases, respectively. A 1- μ s segment is shown

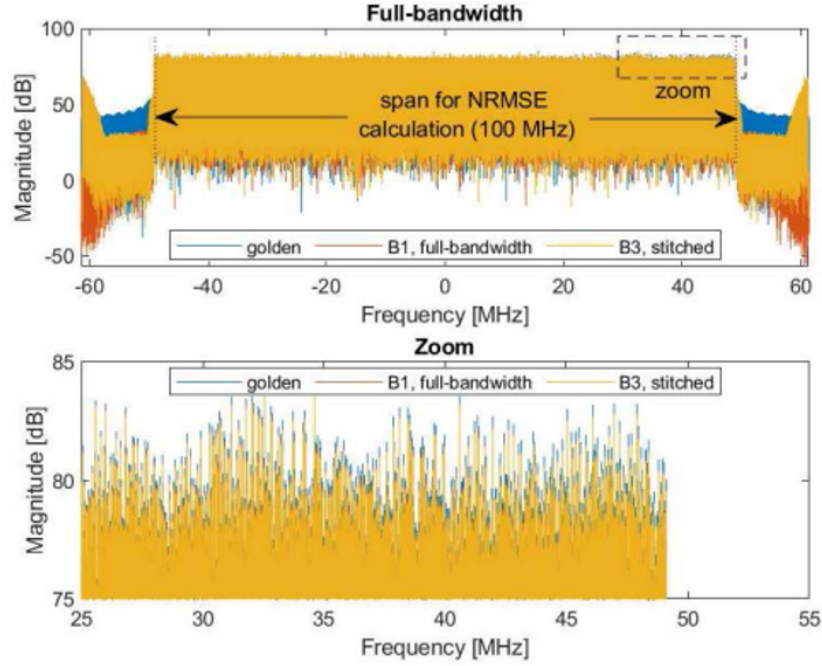


Figure 77: Frequency-domain counterpart of the golden I/Q data and that of the B1 and B3 cases, respectively, (top) over the full 122.88-MHz band and (bottom) that zoomed to the frequency range around 40 MHz where a slight deviation is observed

The I/Q data are further compared in the frequency domain, which is more important for OFDM signals, as shown in Figure 77. Within the center 100-MHz channel bandwidth, both the B1 and B3 cases have a good match to the golden I/Q data, except for the frequency range around 40 MHz. Since the deviation happened in both the B1 and the B3 cases in the same way, it is probably caused by the signal generator that the original RF signal itself is slightly distorted in that frequency range.

The normalized root-mean-square error (NRMSE) is further calculated to quantitatively measure the deviation from the B1 and B3 cases to the golden data, respectively, within the center 100-MHz channel bandwidth. The NRMSE is defined by eq. (10) in [71]. The resultant NRMSE for the B1 case and the B3 case is 3.32 % and 3.78 %, respectively. A summary of the resultant NRMSE for all measurements is given in Table IV [71]. We can see that the NRMSEs are stable across the three repetitions. Taking the values of the B1 case, i.e., the conventional full-bandwidth measurement, as the reference, the B4 case results in the largest difference of about 1 % for Series 1, and the B3 case results in the largest difference of about 0.5 % for Series 2.

An in-house demodulation and EVM evaluation algorithm is implemented according to the standard [75]. Given the known golden data, the frame head is found, and the carrier recovery is conducted. Given the known frame structure, the symbols are further demodulated. Moreover, equalization is performed with respect to the demodulation reference signal symbols. Finally, the EVM is calculated for each slot within the frame over the symbols in the physical downlink shared channel (PDSCH).

The constellation of the demodulated symbols of the first slot in the PDSCH channel is shown in Fig. 10 in [71] for the golden I/Q data and that of the B1 and B3 cases, respectively. The root-mean-square averaged EVM is calculated over the individual EVMs of the 20 slots within the frame to represent the EVM of the whole frame. The resultant

averaged EVMs

for the B1 and B3 cases are 1.31 % and 0.97 %, respectively. A summary of the resultant averaged EVM for all measurements is given in Table V in [71]. We can see that the averaged EVMs are stable across the three repetitions. Taking the values of the B1 case, i.e., the conventional full-bandwidth measurement, as the reference, all the band-stitched results (from B2 to B4) seem to be lower than the reference values by about 0.3 % in Series 1, whereas no significant differences between the band-stitched results and the reference values are seen in Series 2. The power spectrum density of the I/Q data is calculated with the Welch method [77] for all band-stitching cases and measurement series, as shown in Figure 78.

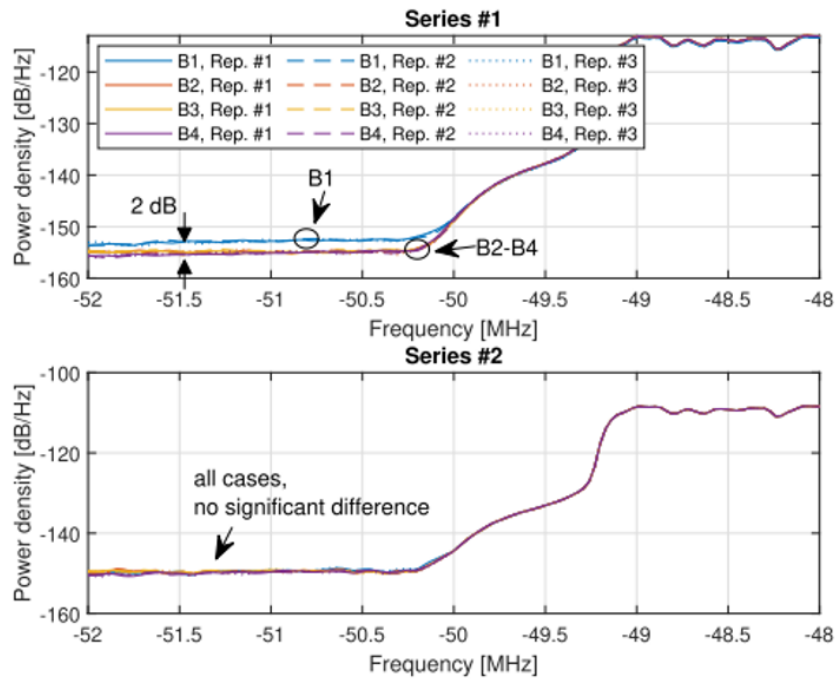


Figure 78: Power spectrum density of all band-stitching cases and measurement series around -50-MHz frequency where the transition between the signal and the noise occurs. A difference of about 2 dB in the noise density is seen between the full-bandwidth B1 cases and the stitched B2–B4 cases in Series 1, whereas no significant difference is seen for all cases in Series 2

A difference of about 2 dB in the noise power density is seen between the full- bandwidth B1 case and the stitched B2–B4 cases in Series 1, whereas no significant difference is seen in Series 2. The difference in the resultant averaged EVM is likely caused by the change of signal-to-noise ratio in Series 1. From a separate stand-alone noise measurement of the VSA, we find that the VSA might switch its internal sampling paths depending on the configured sampling rate with 100 MHz as a threshold, above which the noise power density increases by about 2 dB. This difference coincides with the observation in Series 1 of Figure 77. As for Series 2, the effect of the change of noise power density from different sampling rates is obscured by the extra noise from the external mixers.

Finally, the effect of the two-step delay correction method is shown in Figure 79 and Figure 80 in terms of the NRMSE and the averaged EVM, respectively.

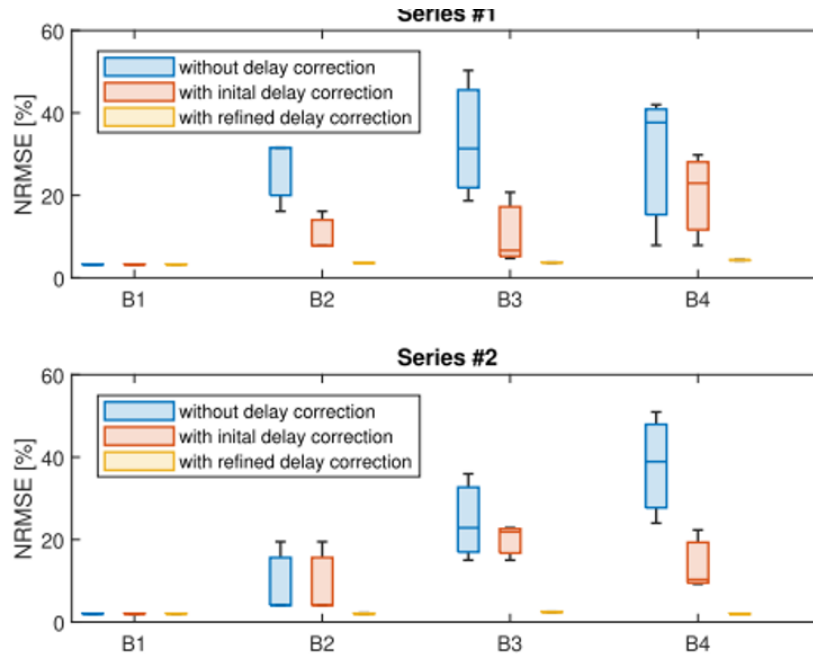


Figure 79: Effect of the two-step delay correction method in the NRMSE for all band-stitching cases and measurement series. The central mark of the box denotes the median, and the top and bottom edges of the box denote the 75th and 25th percentiles, respectively. The tips of the top and the bottom whiskers indicate the maximum and minimum values, respectively. The statistics are derived from the three repetitions

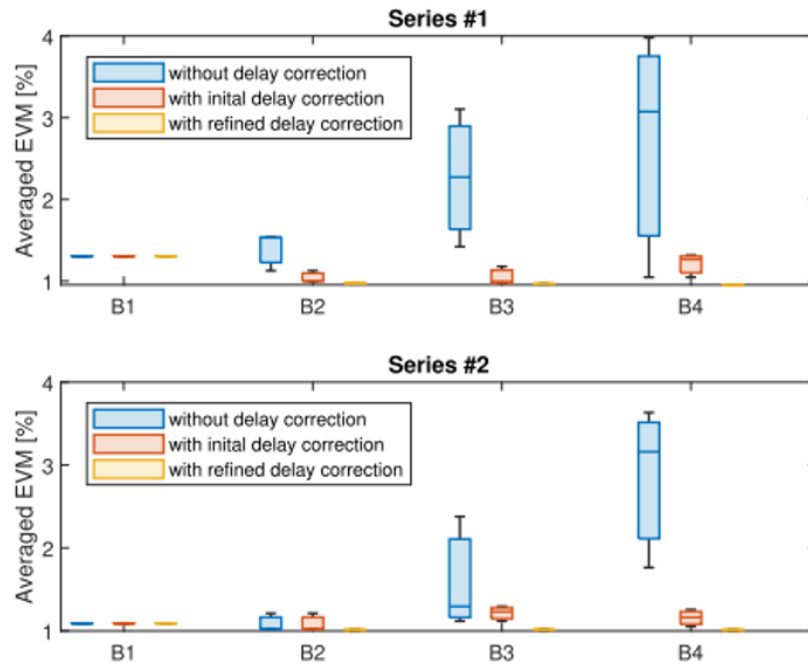


Figure 80: Effect of the two-step delay correction method in the averaged EVM for all band-stitching cases and measurement series. The central mark of the box denotes the median, and the top and bottom edges of the box denote the 75th and 25th percentiles, respectively. The tips of the top and the bottom whiskers indicate the maximum and minimum values, respectively. The statistics are derived from the three repetitions

Three cases are compared, namely, without delay correction, with initial delay correction, and with refined delay correction. The first case is equivalent to timing alignment only with common trigger signals, and zero delay offset is applied to the raw sub-band I/Q data before the stitching. The second case is equivalent to timing alignment with both the triggering and the cross correlation, and the estimated initial delay offset is applied before the stitching. In the third case, both the estimated initial and refined delay offsets are applied before the stitching. Note that the initial phase and magnitude offset correction are always conducted in all three cases under their respective delay offset conditions. Therefore, the only variable among the three cases is the delay offset to be corrected. The statistics are computed from the three repetitions for each case and presented in the box plot. The central mark of the box denotes the median, and the top and bottom edges of the box denote the 75th and 25th percentiles, respectively. The tips of the top and the bottom whiskers indicate the maximum and minimum values, respectively. For the NRMSE in Figure 79, within each band-stitching case (B2, B3, or B4), the spread of the boxes, i.e., the difference between the maximum and the minimum decreases, as the initial and refined delay corrections are conducted, and the level of the box converges to that of the B1 case. It is also worth mentioning that, in the case of the “without delay correction” (blue boxes), the spread of the box increases with the number of sub-bands that are stitched (from B2 to B4). This is reasonable since the more sub-bands to be stitched, the more impairments are left untreated in this case. A similar behavior is seen for the averaged EVM in Figure 80.

3.1.2.5 Conclusion In this subchapter, we discussed how to use band stitching for wideband vector measurements with VSAs of insufficient analysis bandwidth. We proposed a two-step delay estimation method to correct the timing impairment between adjacent sub-bands in postprocessing based on the recorded sub-band data. The method was assessed with two series of validation measurements for the sequential setup at 1- and 28-GHz center frequencies, respectively. The results from three band-stitching scenarios, i.e., two-band stitching, three-band stitching, and four-band stitching, were compared in terms of the NRMSE and the averaged EVM. Excellent consistency between the stitched I/Q data and the reference I/Q data has been seen, which indicates that the proposed sub-band impairment estimation method works well. Moreover, the significance of conducting the second refined delay correction has also been demonstrated by comparing the resultant NRMSE and averaged EVM to that of the state-of-the-art methods, i.e., timing alignment through common trigger signals and through the cross correlation.

The band-stitching process with the proposed sub-band correction method allows for measurement of signals of wider bandwidth than the intrinsic analysis bandwidth of VSAs. Potential applications may include ultrawideband signals, THz communication, spectral leakage measurement of power amplifiers, and so on. The whole process can be implemented with software defined radios as well with a high flexibility. Compared with the traditional vector measurement with a single VSA where all measures are reported at once without much user intervention, additional computational complexity is introduced in the postprocessing for sub-band correction in exchange of the effectively extended analysis bandwidth. In future work, an extensive measurement uncertainty analysis needs to be investigated to quantify more thoroughly the accuracy of the whole measurement process for, e.g., various types of test signals and a larger number of stitched bands.

3.2 Experimental Validation and Applications of mmWave 8 × 8 AiP Array Platform

The 5G communications at mmWave frequency bands would provide new valuable radio spectrum for wireless communications [78]. The large bandwidth, which is available at mmWaves communications can lead to a significant

increase of the speed of wireless data transmission in numerous applications [79]. The US Federal Communications Commission (FCC) released considerable available spectrum in the 28–73 GHz band. Further, some frequency bands, which may be available in the future are being reviewed in [80]. Therefore, mmWave communications has great promise for research and application. However, the high propagation loss and the low SNR at the mmWave frequency band have limited to some extent the rapid expansion of mmWave communications [81]. Directional high gain antennas are widely utilized as Tx or Rx in communication systems [[82], [83] to overcome the above mentioned disadvantages. However, with the increase of the antenna gain, the beam-width of the antenna decreases. The latter decreases the effective coverage of the antenna. Reliable communication in dynamic scenarios for time-variant locations of Tx/Rx and propagation scenarios are ensured by the use of beam-tracking. Electrical beam-steering of phased arrays is important to provide real-time tracking of the dominant propagation paths [84]. Phased array systems, where each radio frequency chain consists of an antenna, a phase shifter and an attenuator [85], are widely used in the mmWave systems. The phase and amplitude excitation of each element can be regulated by the use of the phase shifters and attenuators. Therefore, the phased array beam pattern can be directed to a given spatial directions. This leads to low development and maintenance costs, easy installation and portability, fast product iterations, and low operational energy consumption. The AiP system combines the antennas and control circuits of a phased array into a single package. AiP technology has been widely used in mmWave, for instance, radios, automotive radars, imaging sensors [86]. Among the benefits are small size, low development costs, low power consumption and fast beam-steering capability.

In this subchapter, based on the work in [87], hardware and control architecture of an 8×8 AiP is proposed. The suggested architecture can be seen as an extension of the 4×4 AiP design architecture presented in [88]. Experiments are performed to validate the AiP stability and evaluate the accuracy of the array calibration. Two application examples of the AiP are presented, where the AiP is used as an experimental platform for phased array calibration and mmWave channel sounding, respectively.

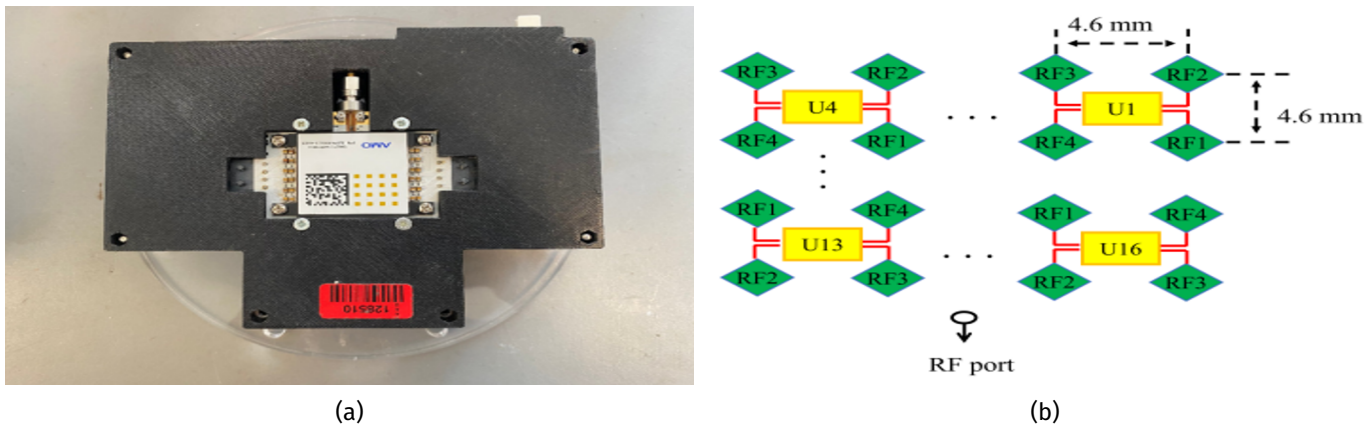


Figure 81: a) Photos and b) chips and antennas layout of the 8×8 AiP model

The 8×8 AiP array module is presented in Figure 81. The 64 antenna elements of the AiP array are arranged in the form of 8×8 . The spacing between the antennas elements is 4.6 mm, which is approximately equal to a half-wavelength at 28 GHz. The block diagram of the 8×8 AiP is shown Figure 82.

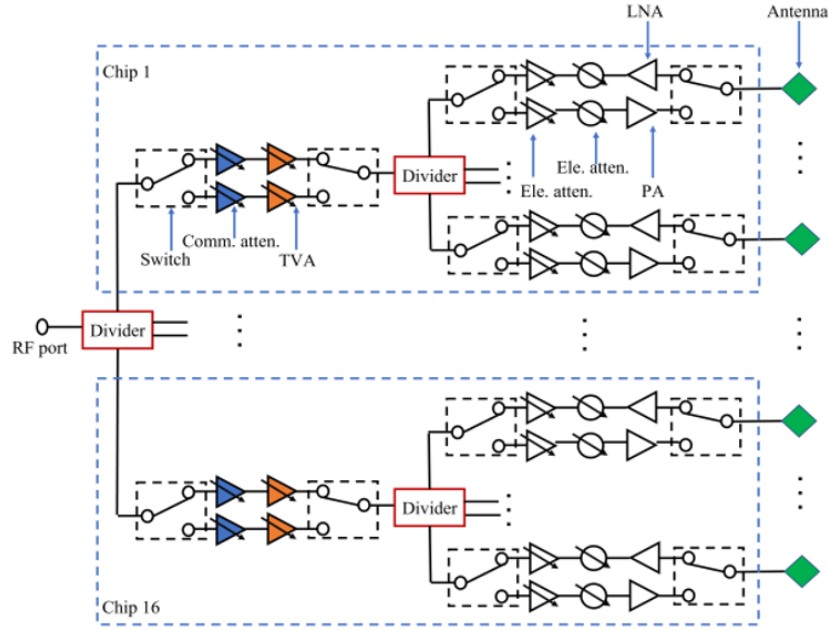


Figure 82: Block diagram of the 8 × 8 AiP

The 8 × 8 AiP consists of 64 patch antennas functioning at 26.5 to 29.5 GHz. Furthermore, 64 6-bit phase shifters are used, with a phase shift range of 0° to 359° and a control resolution of 5.625°. 64 6-bit attenuators with an attenuation range of 0 to 7.5 dB and a control resolution of 0.5 dB are utilized. 32 common attenuators with an attenuation range of 0 to 15 dB and a control resolution of 1 dB are used. Moreover, 32 temperature variable attenuators (TVAs), providing gain compensation for the disturbance of RF chains due to the variation of the AiP temperature, are used. There are available 64 power amplifiers (PAs), which are tuned when the AiP works in a Tx mode, and 64 LNAs, which are tuned with the AiP operating in a Rx mode. The operation mode (i.e., Tx or Rx) of the AiP is programmed by 160 switches. Furthermore, there are 16 ANOKIAWAVE AWMF-0158 RFICs chips. Each RFIC has four control chains, each of which is connected to a patch antenna. To control the amplitude and the phase, a 6-bit phase shifter and a 6-bit attenuator are integrated in each control chain. Therefore, controlling the attenuator and the phase shifter in the RFIC is used to feed the the excitation of the patch antenna. One STM32F427VIT6 chip operates as the microprogrammed control unit (MCU) of the AiP board. The external control computer interacts with MCU by the use of a universal asynchronous receiver/transmitter (UART). The control the AiP RFICs chips by the MCU is made with the use of the serial peripheral interphase (SPI). The main program of the designed AiP includes commands to control the element phase shifters, common attenuators and element attenuators. Moreover, Tx/Rx mode switching commands for setting the AiP to work in a Tx or a Rx mode, element switch commands for controlling each element of the AiP to turn on or off and chip temperature read commands for reading the temperature of each chip of the AiP are used.

Calibration measurements in the compact antenna test range (CATR) chamber are carried out. Photo of the measurement setup is shown in Figure 83.

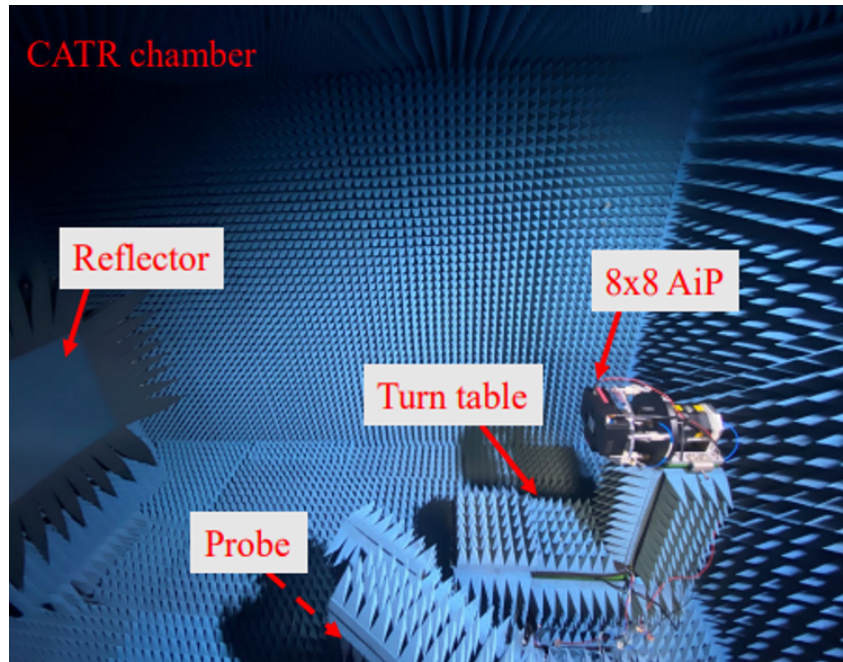


Figure 83: Photo of the AiP calibration measurement setup

The measurement system consists of a VNA operating from 10 MHz to 43.5 GHz, a laptop (controlling the AiP and VNA) and an adjustable 12 V DC power supply working for the AiP module. The VNA measures the transmission S-parameters S₂₁ between the AiP and the CATR probe antenna at 28 GHz. It has to be noted that the broadside direction of the AiP is aligned with the center of the CATR reflector. For this measurement setup, the CATR probe antenna is set as the Tx and the AiP is set as the Rx. The probe antenna and the reflector generate plane waves impinging at the AiP phased array. The Tx power is 10 dBm and the used IF in the VNA is 10 Hz. The complex least squares method presented in [89] is used to calculate the calibration coefficients of the AiP elements for 10 repetitive measurements. The impact of temperature on the stability of the AiP is analyzed by first turning the AiP on for a period of time to warm up before the calibration measurements. Afterwards, the first to the sixth calibration measurements are carried out after the temperature was stabilized. After the sixth calibration measurement is performed, the AiP is turned off to allow it to cool down, and then the AiP is turned on again to carry out the seventh through tenth calibration measurements. It is worth to note that during each calibration measurement, the temperature of the 16 element chips of the AiP is recorded before each element's phases are reset. If the tenth calibration measurement is used as the reference, the respective differences between the first nine measurements and the tenth are shown in Figure 84.

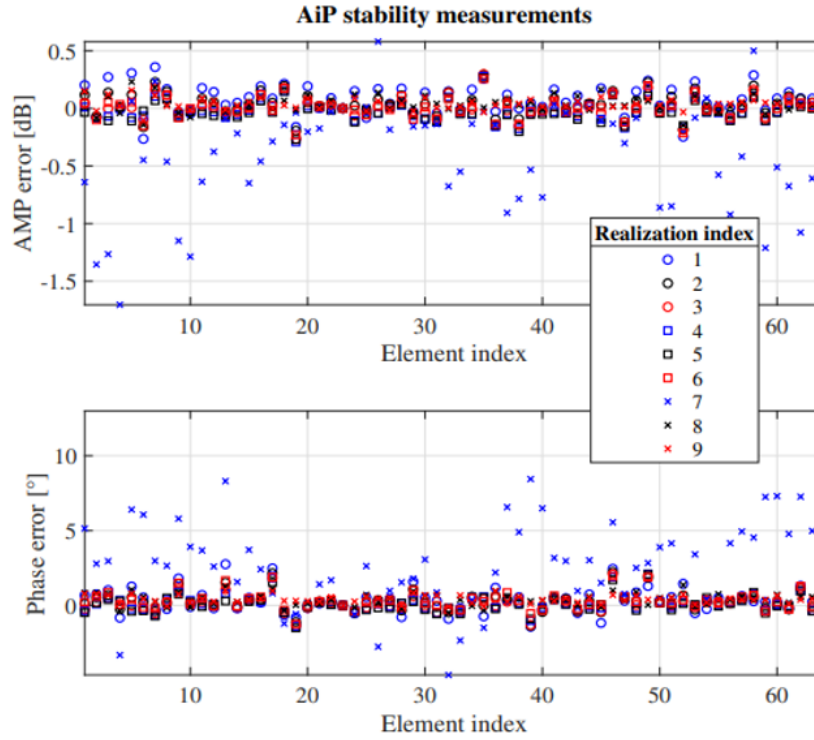


Figure 84: AiP elements stability measurement results

Excluding the result of the seventh measurement, all the rest of the measurements have a good agreement with the tenth one in terms of both the amplitude and phase excitation of array elements. Additionally, the average AiP chips temperature is constant throughout the measurements, except for the seventh measurement. Obviously, the offset in the result for the amplitude and the phase in the seventh measurements can be explained by the fact that this measurement is done after the AiP being off for some time and again then turned on, the average temperature of the AiP chips is a bit high during the early part of the measurement procedure until it again stabilizes. Therefore, the operating temperature of the AiP has a significant impact on the stability of the elements. It is recommended that the AiP must be used when it is in its stable state (the temperature is stabilized).

The beamforming pattern measurements of the AiP are also performed in the CATR. The block diagram of the AiP beamforming pattern measurement setup is presented in Figure 85.

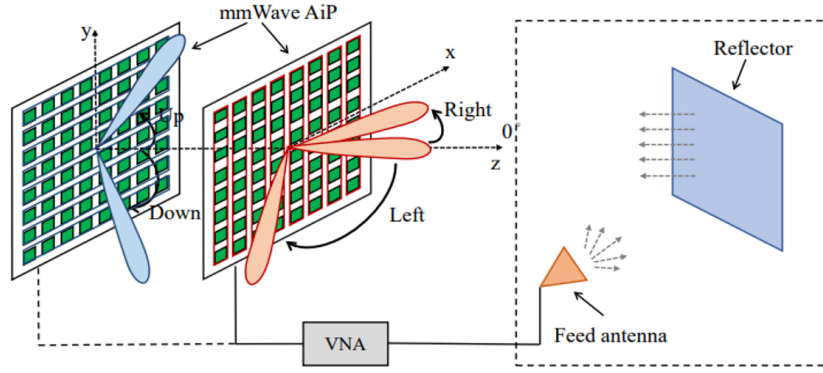


Figure 85: Block diagram of the AiP beamforming pattern measurement setup

The AiP beamforming patterns at different angles are presented in Figure 86. The AiP beamforming performance is validated by showing that the peak directions of the patterns varies with the beam-steering angles.

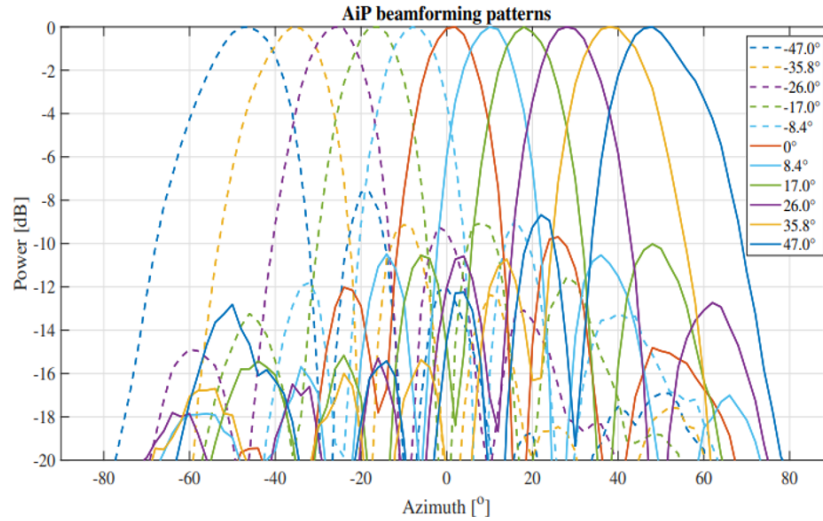


Figure 86: AiP beamforming patterns at different angles

The 8×8 AiP is used also as a validation platform to investigate the calibration accuracy of the calibration methods on large arrays and the performance of AiP-based channel sounding, respectively. The 8×8 AiP array with 64 elements can be defined as a large array. The effectiveness of the 'inverse', 'on-off' and 'least squares' calibration methods on large phased array is investigated. Details on the obtained results can be seen in Figure 9 - Figure 11 in [87]. The reader can find more details about the calibration methods and most particularly how the amplitude and the phase of some elements of the AiP are changed intentionally. The 'inverse' method is not able to effectively calibrate the AiP with a large array. The calibration excitation matrix is large, which makes the calibration influenced significantly by the measurement noise. Therefore, the 'inverse' method is not suitable for calibration on large phased arrays. The AiP array calibration excitation matrix of the 'least squares' method is based on the Hadamard matrix [89], and the condition number is 1. Therefore, the phased array calibration is less affected by the measurement noise. The errors between the calibration results of the other two methods ('least squares' and 'on-off') for the four intended changed elements and the corresponding reference values are shown in Table VII.

TABLE VII
VARIATION BETWEEN THE RESULTS OF AIP ELEMENTS CALIBRATION MEASUREMENTS

Element	'On-off' Amp. Err. [dB]	'LS' Amp. Err. [dB]	'On-off' Pha. Err. [°]	'LS' Pha. Err. [°]
1	-0.2	-0.2	1.6	2.8
2	-0.3	0.2	5.0	-1.9
3	0.7	-0.4	2.6	1.7
4	1.5	-0.2	2.9	-3.6

The results show that both methods can perform effective measurements on the AiP array. As expected, some error are also observed. The errors are mainly introduced by the limited control accuracy of the element attenuator and phase shifter and the measurement noise. Most particularly, when the element complex filed amplitude is small, the measurement noise has a large impact on the 'on-off' calibration accuracy.

The environment and system setup of the AiPs channel sounding measurement can be seen in Figure 87.

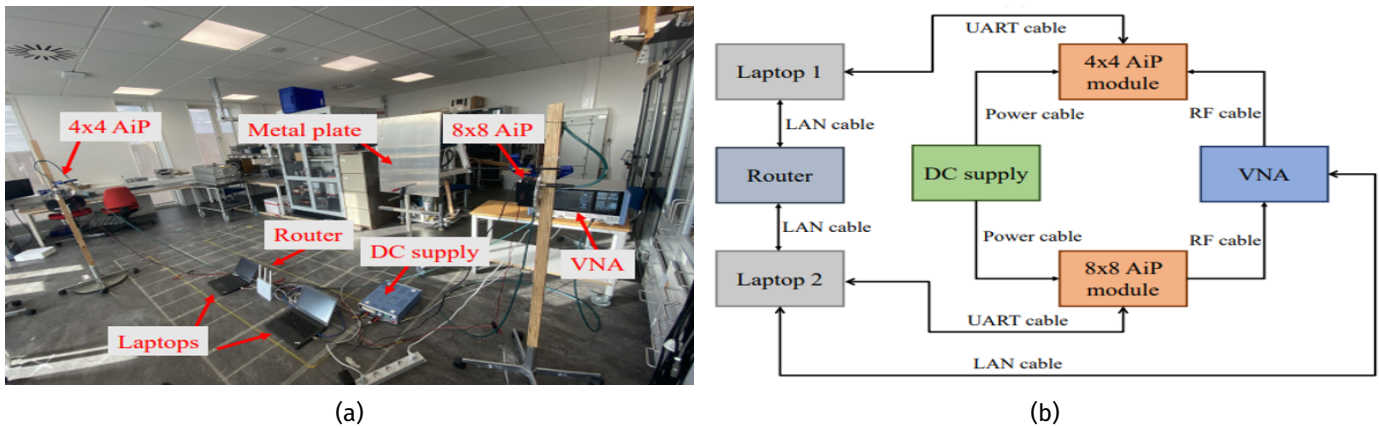


Figure 87: a) Photo and b) block diagram of the AiPs channel sounder setup

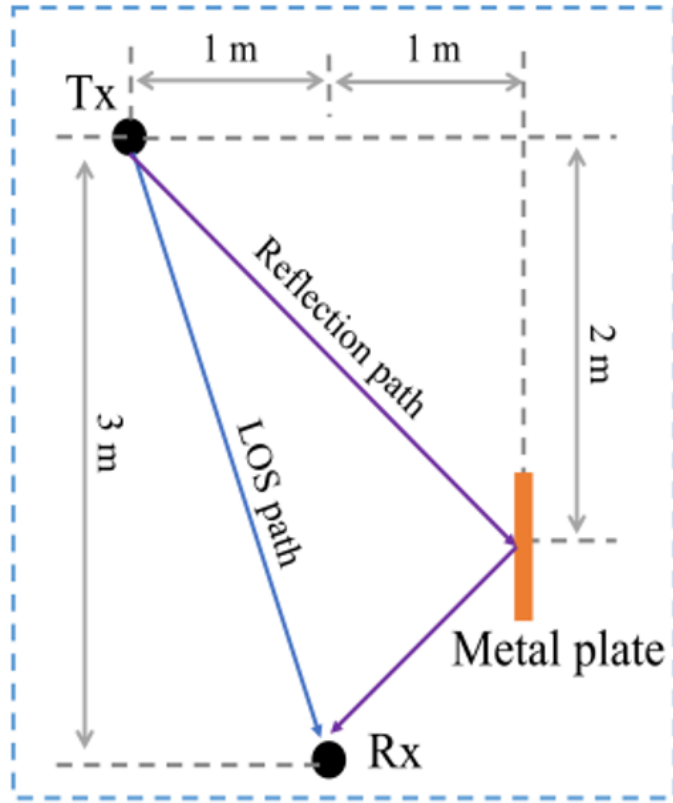


Figure 88: Placement of the Tx, Rx and metal plate

The 4×4 AiP described in [88] is employed as the Tx, while the 8×8 AiP configuration is used as Rx. A metal plate is used to act as a reflector in the channel environment. The height of the Tx and the Rx is 1.2 m. The placement of the Tx, the Rx and metal plate is shown in Figure 88. Port 2 of the VNA is connected to the Rx, while port 1 to the Tx. By measuring the S-parameter with the VNA, the channel frequency response between the Tx and the Rx is obtained. When the AiPs channel sounder measures the channel, laptop 1 controls the Tx AiP beam-steering, which enables the AiP to beam-steer in the horizontal plane from -53° to 53° . For each beam steered by the Tx AiP, laptop 2 controls the Rx AiP steering beams from -72° to 72° in the horizontal plane.

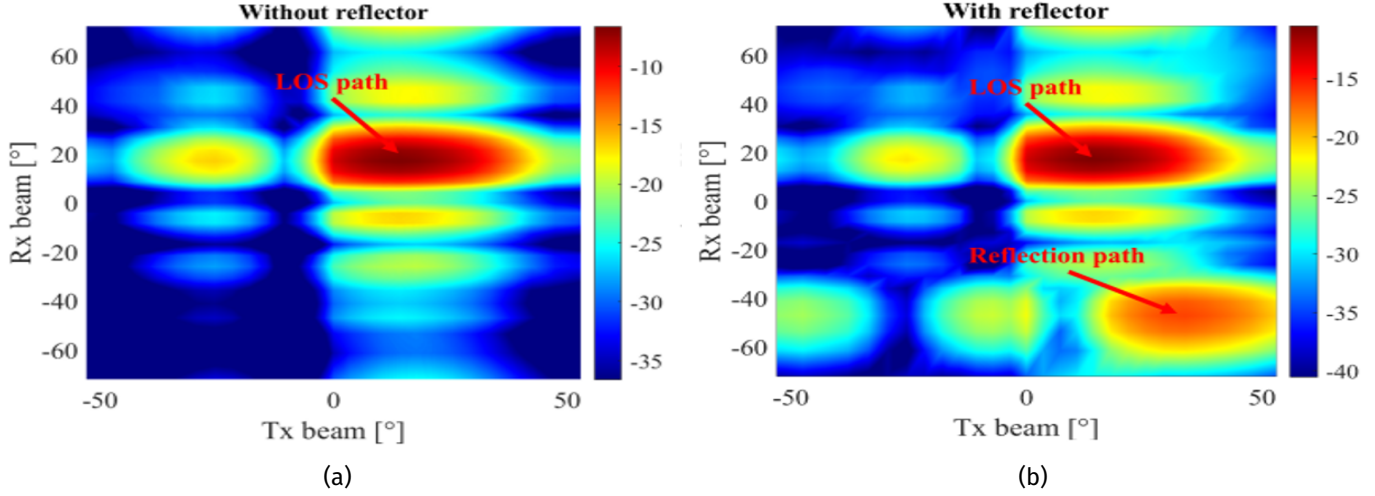


Figure 89: Measurement results for a) without the metal plate and b) with the metal plate

The channel sounding measurements results are shown in Figure 89 for scenarios without and with the metal plate. The AOD and AOA of the LOS path between Tx and Rx are the same and is approximately 18.4° . It is found that the highest peak appears when both the Tx AiP and Rx AiP steering the beam in approximately 18° , demonstrating the ability of the AiPs based channel sounder to detect accurately the LOS propagation path in the measured channel. Figure 15 and Figure 16 in [87] present more measurement results.

In this sub-chapter, the hardware structure and control program of an 8×8 AiP array experimental platform are proposed and discussed. Further, the stability, element weighting control accuracy and beamforming feasibility of the AiP are measured and verified. It is demonstrated that temperature has a high impact on the AiP performance. The calibration accuracy of three different calibration methods for large phased array is investigated with the AiP platform. Due to the measurement noise, the results show that the calibration accuracy of 'inverse' method for large phased array is low. In the channel sounding measurements, the dominant propagation components were analysed in terms of AoA, AoD and delay. The results validate the effective work of the channel sounder. It would save measurement time and make the measurement setup simplified due to the capability for swift beam control of the phased array.

4. Terahertz (THz) Channel Modeling in 6G Deployment Scenarios via Ray Tracing (RT)

4.1 Introduction

Terahertz (THz) communication, which is planned to use (0.1-10 THz) frequency band, is considered to be the key enabling technology to meet the requirement for the high data rate demand in 6G. The main advantage of the THz communications is the abundant available spectrum resources. One precondition for implementing the THz communication systems is to understand and model the THz radio channel for 6G in realistic deployment scenarios. However, channel sparsity, NF propagation and large-scale antenna configuration are among the new radio characteristics in THz bands. They bring new opportunities, but also challenges to channel modeling in terms of accuracy and complexity of the modeling. It was proved experimentally in [90] that the THz channels show directionality and can be characterized by a few dominant paths. Therefore, the propagation channel in the THz bands will be highly sparse and specular. For long-range applications, the THz communication systems will rely mainly on the LOS path, while for short-range applications, a few dominant paths (LOS and reflected paths) can be used. Owing to the use of large-scale antenna configurations (to limit the severe propagation loss), combined with the short-range deployment scenario and short wavelength in the THz bands, channel non-stationary is another aspect that one must take into an account in channel modeling [91]. Considering the channel characteristics and applications of the THz communication systems, a RT method may be a promising approach to model the propagation characteristics and parameters in THz bands for 6G. RT is deterministic modeling approach based on electromagnetic field theory and geometrical optics. Therefore, it enables precise modeling of the dominant paths of THz waves. Moreover, the quasi-optical property of THz waves secures the precision of the RT approach. The requirement for precise modeling of dominant paths can efficiently reduce the complexity of RT (in terms of database precision and interaction orders of propagation mechanisms). For future data-driven research, the RT simulations can provide the essential massive input data, which may not feasible and manageable with measurement data.

This chapter based on the work in [92] presents that deterministic RT is a promising solution to channel modeling in THz bands. Two sets of indoor measurement campaigns in THz bands are carried out to validate the obtained RT simulation results. Good agreement is achieved between the RT simulation and measurement results, which demonstrate the effectiveness of RT approach in THz bands for 6G. In this work, the commercial RT tool Wireless InSite is used to perform the RT simulations.

4.2 Channel characteristics of THz communications systems

1. High propagation loss: The high propagation loss of the THz channel is defined by FSPL and non-negligible atmosphere molecular absorption. The THz channel is known to have high FSPL according to the theory (the Friis formula). Therefore, to compensate for the high propagation loss and to consider the power limitations of the current THz transceivers, high-gain directional antennas must be used at both Tx and Rx ends. Moreover, the absorption of oxygen and water vapor is very common in atmospheric absorption in the THz channel, as the absorption of water vapor is dominant. Unlike at lower frequency bands, the molecular absorption is not a negligible factor and should be also considered for long-range communication scenarios.

2. Sparsity: As it was experimentally demonstrated, the propagation channel becomes sparser and more specular with the increase of the frequency. As it was discussed, the THz propagation channels will be characterized only

by a few dominant paths, i.e. LOS and a few low-order reflection paths, due to high diffraction [93], penetration, and reflection losses of THz waves.

3. Near field and spatial non-stationary: When analyzing the massive Multiple-input-multiple-output (MIMO) systems, the FF and spatial stationarity assumptions applied for traditional MIMO systems may be violated [94]. Typically, due to the high frequency (HF) of THz waves and the small size of the antennas, a large number of antennas can be embedded in limited space. Generally, the assumption of plane waves is not valid, when the propagation distance is less than the Rayleigh distance. Due to the high propagation loss, the communication range will be rather short, making the NF (i.e., plane-wave model assumption is not valid) and spatial non-stationary (i.e., the spatial stationary assumption is violated) effects a significant problem in the THz bands. Therefore, it may be important and beneficial to model these effects in the THz channel modeling.

4.3 Measurement-calibrated ray tracing

Channel modeling can be generally classified into two groups - based on using deterministic or statistical methods. RT is a typical representative of the deterministic modeling approach. The RT-based channel modeling has been extensively used in sub-6 GHz and mmWave bands. However, the channel modeling using the RT approach in the THz band is different from that in mmWave and sub-6 GHz bands. Due to the inherent characteristics of RT, i.e. it is based on geometric optics and it can be explained by the high-frequency approximation of Maxwell's equations, the quasi-optical characteristics make the RT results in the THz band more reliable and suitable than those in the sub-6 GHz band. Moreover, for the THz channel characteristics, the high propagation loss and sparsity characteristics of the THz channel define the requirement for site-specific analysis, which can be provided by the RT simulation. Compared to the sub-6 GHz, the propagation range of THz waves is shorter. Therefore, the RT simulation needs only to be performed over a limited distance and in a limited space. Moreover, considering the sparsity and specularity of the THz channel, RT simulation of the dominant paths, taking into account the limited propagation mechanism and orders of reflections, can be sufficiently precise. However, some challenges to RT-based channel modeling in THz bands must be outlined. A fundamental difficulty is that it does not exist a complete set of EM properties for the materials at THz bands. Moreover, there is a lack of adequate measurements for validating and calibrating RT.

In this work, the performance of the deterministic RT in the THz band is explored by using measurements to calibrate the material EM properties in the corresponding scenario. The measurement-calibrated RT flow is presented in Figure 90.

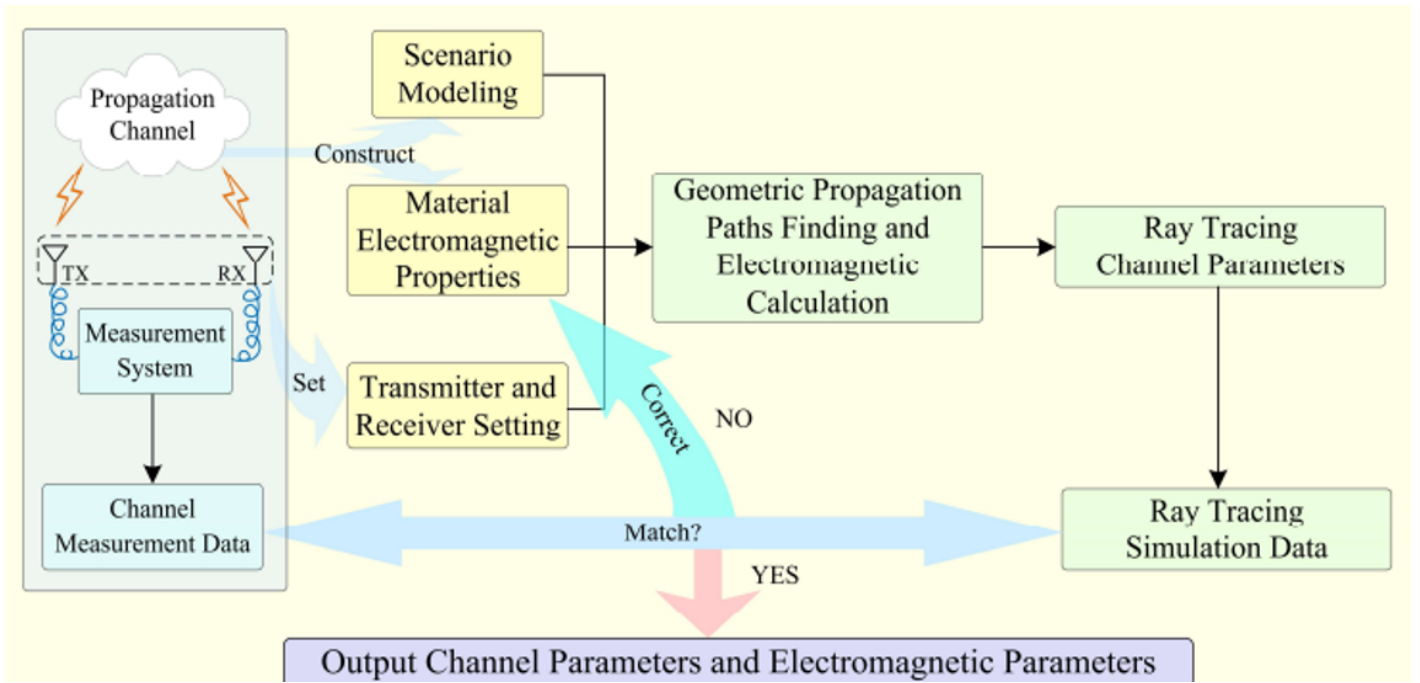


Figure 90: Flowchart of measurement-calibrated RT channel simulation

The knowledge of the measurement scenario (including the Tx and Rx coordinates) is used in the RT simulation to model the environment simulation scenario. The EM calculations are performed and the results such as power gain, delay, and angle for each path (i.e. the RT channel parameters) are obtained. The RT channel parameters are then processed to obtain the required channel information, which is shown as RT simulation data in Figure 90. The calibration process is shown in Figure 90. Afterwards, the material EM properties in the RT simulations are tuned to obtain the best agreement in terms of power and delay for the dominant propagation paths. In the beginning, the RT simulation results, corresponding to the initially used EM parameters for the materials in the RT simulation, are compared with the measurement data. If the results of power and delay parameters for the dominant paths match (a minimization of the root mean square error is targeted), the simulation results are considered as the expected (desired) output. If the results do not match, the relative permittivity and conductivity of the materials are updated, simulation is performed again and a comparison between the results is made again. This operation repeats until the best agreement (match) between the simulation and measurement results is achieved.

The performance of the measurement-calibrated RT is analyzed based on two sets of indoor measurement campaigns at the THz bands. Channel measurements were carried out by using the VNA based channel sounder (utilizing the RoF technique to extend the measurement distance) at Aalborg University, Denmark [1]. The measurement setting parameters are listed in Table VIII. The measurements were conducted in two indoor typical scenarios, i.e., the empty room and the spacious hall. The investigated scenarios were chosen such that the channel characteristics are different and therefore the accuracy of RT simulation in different deployment scenarios can be demonstrated. The obtained parameters of several dominant paths are presented in Table IX for comparison of the measurements and RT simulations. The gain in the empty room scenario is calculated with the antenna gain included.

TABLE VIII

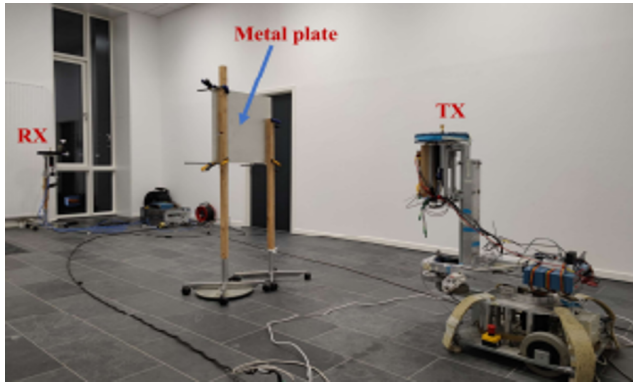
MEASUREMENT SETUP

Parameter	Empty room scenario	Spacious hall scenario
Frequency (GHz)	100	300
Bandwidth (GHz)	6	2
Transmitted power (dBm)	0	5
Measurement description	Virtual array (Aperture = 1 m)	Horn antenna rotation
TX antenna type (gain, HPBW)	Omnidirection (4.5dBi, –) Fixed	Horn antenna (26dBi, 8°) [–90 : 4 : 90]
TX rotation	Omnidirection (4.5dBi, –)	Horn antenna (26dBi, 8°)
RX antenna type (gain, HPBW)	[–180 : 0.5 : 180] (virtual array)	[–180 : 4 : 180]
RX rotation	6.5	4.2
	1.25	1.25

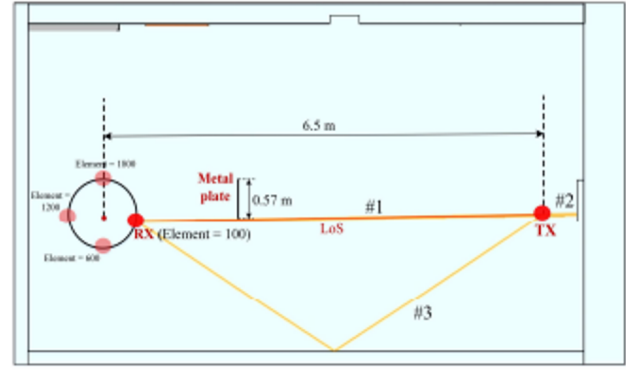
TABLE IX
PARAMETERS OF MEASUREMENT AND RT PATHS

Scenario	Path Index	Parameter	Measurement	RT	Difference
Empty room*	1	Delay [ns]	20.3	20.2	0.1
		Path gain [dB]	-86.9	-87.1	0.2
	2	Delay [ns]	23.7	23.7	0
		Path gain [dB]	-87.5	-87.2	-0.3
	3	Delay [ns]	27.2	27.2	0
		Path gain [dB]	-91.3	-91.2	-0.1
Spacious hall	1	AOA [deg]	-38.0	-36.3	-1.7
		AOD [deg]	-36.0	-36.3	0.3
		Delay [ns]	14.0	14.1	-0.1
		Path gain [dB]	-44.5	-44.5	0
	2	AOA [deg]	-56.0	-54.3	-1.7
		AOD [deg]	82.0	82.4	-0.4
		Delay [ns]	24.0	24.4	-0.4
		Path gain [dB]	-57.9	-57.6	-0.3
	3	AOA [deg]	-104.0	-102.2	-1.8
		AOD [deg]	22.0	23.5	-1.5
		Delay [ns]	31.5	30.8	0.7
		Path gain [dB]	-65.4	-64.7	-0.7

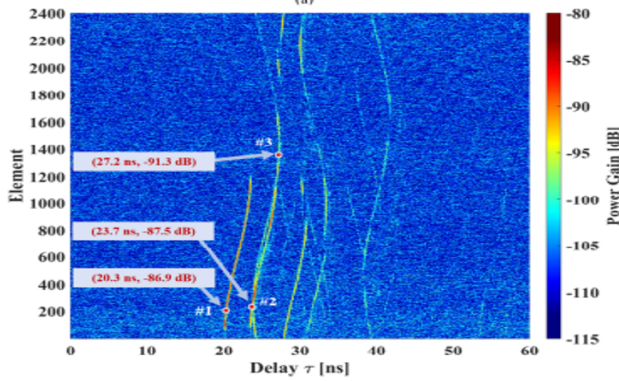
*: Note that the path parameters of this scenario are obtained with one element of the virtual large-scale array as the reference.



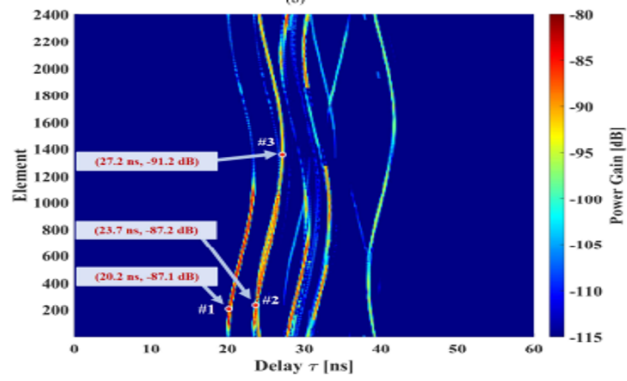
(a)



(b)



(c)



(d)

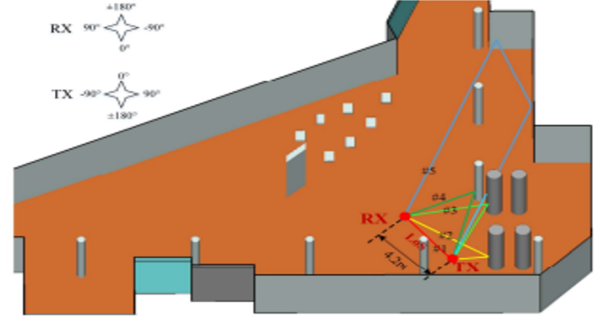
Figure 91: Empty room scenario a) RX view in the empty room scenario b) Ray trajectories c) Power-delay-element measurement result d) Power-delay-element simulation result

Figure 91 presents the empty room scenario and the obtained results. This measurement campaign was carried out at 100 GHz with a bandwidth of 6 GHz. The Tx uses a vertically polarized omnidirectional antenna, while a virtual UCA antenna with a radius of 0.5 m and 2400 elements was created and used at the Rx end. With the used UCA antenna, accurate parameters of MPCs (path gain, delay, and angle) can be extracted from measurement data via parametric estimation [95]. The gain of the Tx and Rx antennas is 4.5 dBi. The distance between the Tx and the center of the UCA is 6.5 m. The height of both Tx and Rx is 1.25 m. A metal plate is positioned near the Rx during the measurements (as shown in Figure 91a). Figure 91b presents the diagram of the ray trajectories of the dominant path. The trajectory color changes from red to yellow, indicating the decrease in the received power. It was found that the dominant paths come from first-order reflection and second-order reflection paths. As expected, the received power of the paths generally decreases as the reflection order increases. The measured power delay profile across elements of UCA is presented in Figure 91c. The power and delay of MPCs vary with the elements, identifying clearly the existence of non-stationary characteristic in the spatial domain. The non-stationary characteristics of the path with high delay are more obvious, defined by the extended range of power values and the increase of the curvature of the delay-element curve. Therefore, it can be concluded that the spatial non-stationary characteristics of higher-order reflection paths may be more visible. Figure 91d presents the RT results with performed measurement-based calibration. Comparing the RT results and the measurement results, the trajectory of MPCs across the array elements is almost the same. The three strong MPCs are denoted by numbers. A good agreement is obtained between the measurement and RT simulated paths in terms of power, angle, and delay.

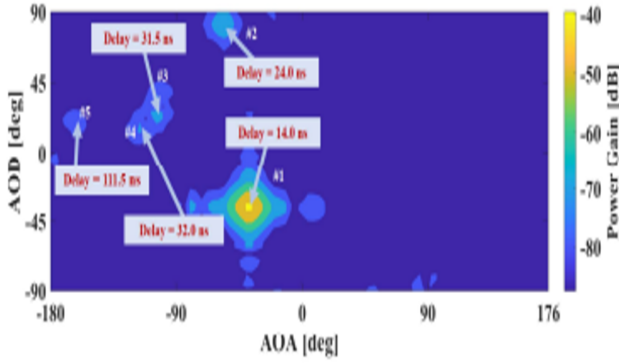
As listed in Table IX, the delay differences between the three dominant paths are within the interval $[0, 0.1]$ ns and the power differences are within ± 0.3 dB. It is worth it to note that the standard geometry-based stochastic channel modeling approaches most probably will fail to model such NF and spatial non-stationarity effects.



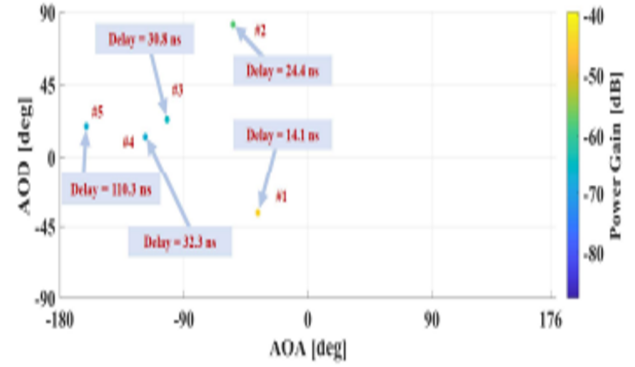
(a)



(b)



(c)



(d)

Figure 92: Spacious hall scenario: a) Photos in the hall scenario b) Ray trajectories c) Power-AOA-AOD measurement result d) Power-AOD-AOA simulation result

Figure 92 presents the spacious hall scenario and the obtained results. The measurement campaign was conducted at 300 GHz with a measurement bandwidth of 2 GHz. Horn antennas with horizontal HPBW of 8° and a gain of 26 dBi were used at both Tx and Rx ends. Tx was rotated within the range $[-90, 90]^\circ$ and Rx was rotated within $[0, 360]^\circ$, both with a step of 4° . The distance between Tx and Rx is 4.2 m. The height of both Tx and Rx is set to 1.25 m. Figure 92b presents the ray trajectories. It was found that 5 dominant paths come from the LOS path and the reflection paths of the adjacent columns. Figure 92c illustrates the measured power angle profile, in which 5 dominant paths are also marked in numbers. Furthermore, the delay of 5 dominant paths is added in a written form for comparison purpose. Figure 92d presents the RT simulation results for the five dominant paths. By comparing Figure 92b with Figure 92d, a good agreement in the MPCs in both the spatial and the delay domains between the measurement and RT results is obtained. For example, the differences between the measurements and RT simulations for the delay of the 5 paths are within ± 2 ns. From the listed numbers in Table IX it can be concluded that the maximum differences of AOA, AOD, delay and power gain of the dominant paths are -1.8° , -1.5° , 0.7 ns and -0.7 dB respectively, while the minimum differences are observed for path 1, and they are -1.7° , 0.3° , -0.1 ns and 0 dB respectively.

4.3.1 Ray tracing validation for 330 to 500 GHz

The performance of the proposed channel sounding system implemented for the measurements was validated using a ray-tracing (RT) model developed with the BJTU RT Cloud software. This validation was based on two sets of indoor measurement campaigns conducted within the 330–500 GHz frequency range. The measurements employed a Keysight VNA-based channel sounder, which utilized a RoF technique to extend the effective measurement range. The experiments were carried out in the atrium at NPL London an indoor environment with approximate dimensions of $15 \times 20 \times 6$ meters, as explained in Section 2.5.1.2. During the measurements, the transmitter (Tx1) remained stationary, while the receiver (Rx) was moved to two different positions to capture spatial variations in the channel response.

Table 6: Typical parameters of the SGH-26-WR2.2 horn antenna used in the Ray tracing model.

Parameter	Typical Value
Frequency	330 – 500 GHz
Directivity	26 dBi
3 dB Beamwidth, E-plane	7.7 deg
3 dB Beamwidth, H-plane	8.5 deg
Sidelobe, E-plane	-10 dB
Sidelobe, H-plane	-33 dB
S11	-20 dB

As an initial step, the environment was modeled in SketchUp with precise dimensions to accurately replicate the real-world scenario. Figure 93 presents a detailed indoor model of the NPL atrium measurement area. The virtual setup incorporates realistic materials such as concrete flooring, brick walls, glass windows, and a wooden table to closely emulate the actual measurement environment (see Table 7). The high-gain SGH-26-WR2.2 horn antennas, whose parameters are listed in Table 6, were used for both transmission and reception. Each antenna has a directivity of 26 dBi and a half-power beamwidth of 8.5 degrees. The antennas were aligned in a direct LOS configuration to ensure accurate channel sounding measurements. The results of the simulated and measured indoor scenario

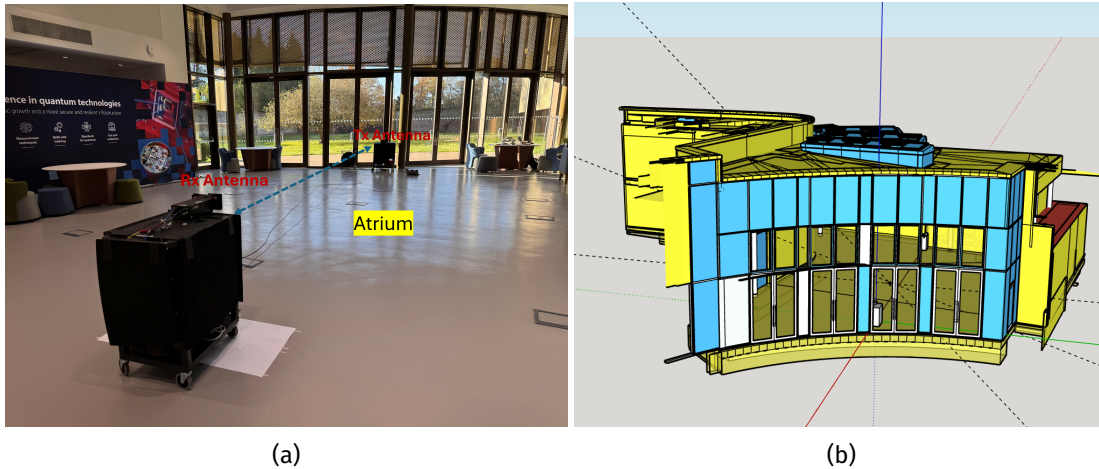


Figure 93: Visual comparison of the real and simulated environments: (a) actual NPL atrium; (b) 3D equivalent model of the atrium created in SketchUp.

at 330–500 GHz are presented in Figure 94b. The simulated LOS peak position closely aligns with the measured LOS peak; however, a slight time difference of approximately 0.02 ns is observed between the two. This discrepancy can

Table 7: Material properties used in the ray-tracing simulation at (330-500) GHz frequencies.

	ceiling	Floor	Paper Glossy	Wood (Dry)
Real Permittivity	1.52	3.00	1.96	2.00
Loss Tangent	1.10	0.06	0.07	0.05

be attributed to factors such as the waveguide connection flange between the Tx or Rx antenna and the frequency extender head, which introduces a distance error of approximately 6 mm. Furthermore, the difference may also result from potential measurement errors in determining the Tx–Rx separation, as well as calibration errors or drift in the actual measurement setup.

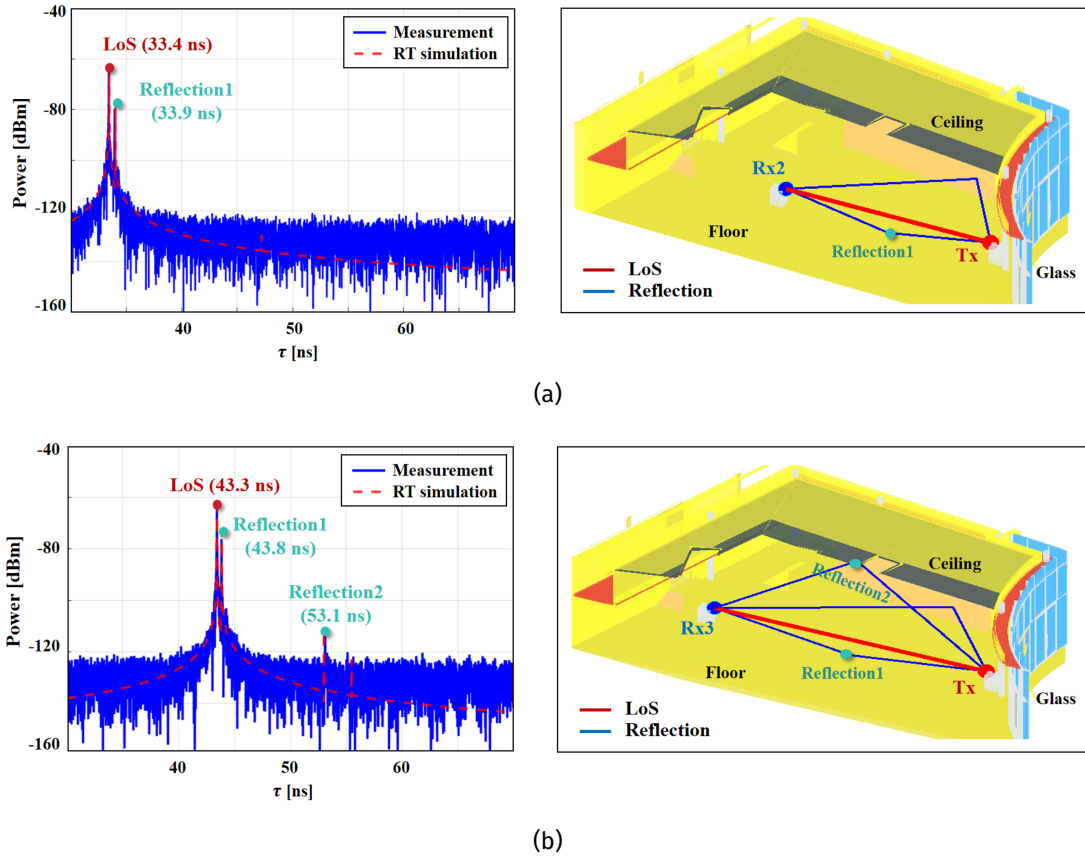


Figure 94: Comparison between measured and ray-tracing (RT) results using the BJTU RT Cloud software in the NPL atrium scenario: (a) Tx–Rx2 configuration; (b) Tx–Rx3 configuration.

As the distance between the Tx and Rx increases, the propagation delay is observed to increase correspondingly. Additionally, ray-tracing results reveal the presence of NLOS components. These delayed reflection paths originate primarily from interactions with the floor, ceiling, and surrounding walls as shown in Figure 94 .

4.5 Ray tracing validation for 500 to 750 GHz

A comparison between ray-tracing (RT) simulation outputs and measured data was undertaken across various indoor environments within the 500–750 GHz (sub-THz) frequency band [96]. The purpose of this validation was to assess

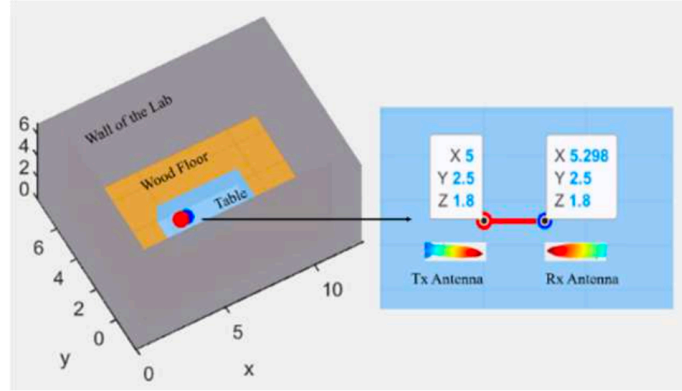


Figure 95: Simulated laboratory scenario (the distance between the Tx and Rx antennas is 250 mm for illustration purposes).

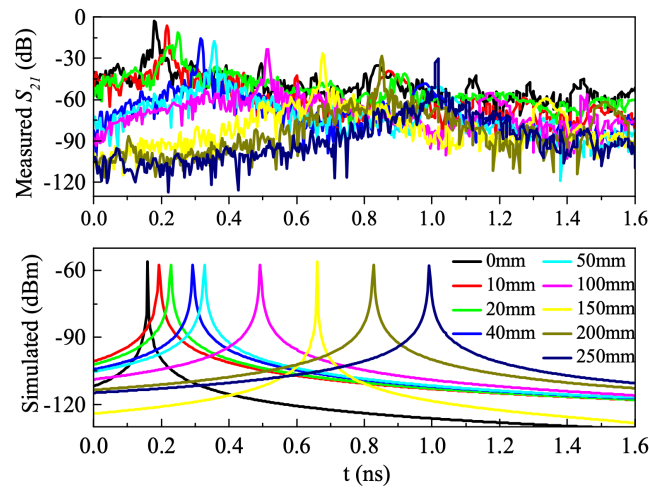


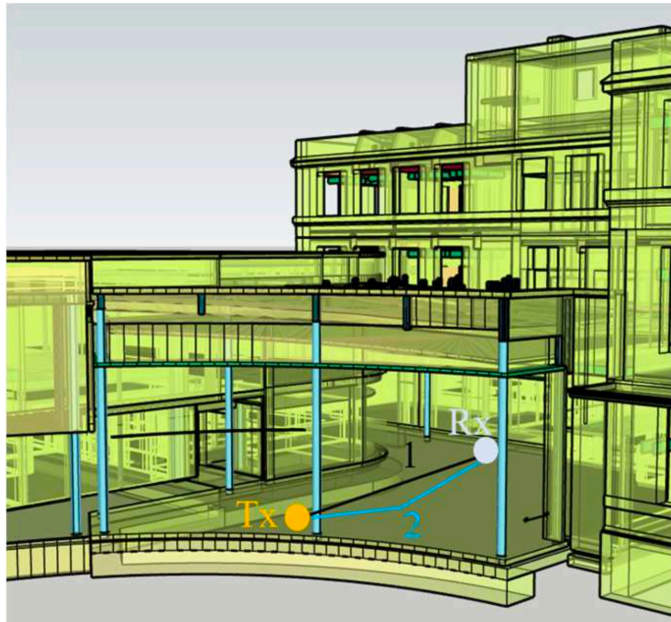
Figure 96: Results of measured (top) and simulated (bottom) indoor scenario.

the accuracy of the simulation platform in replicating real-world channel behaviour and to establish its applicability for predicting propagation characteristics in support of future sub-THz communication systems.

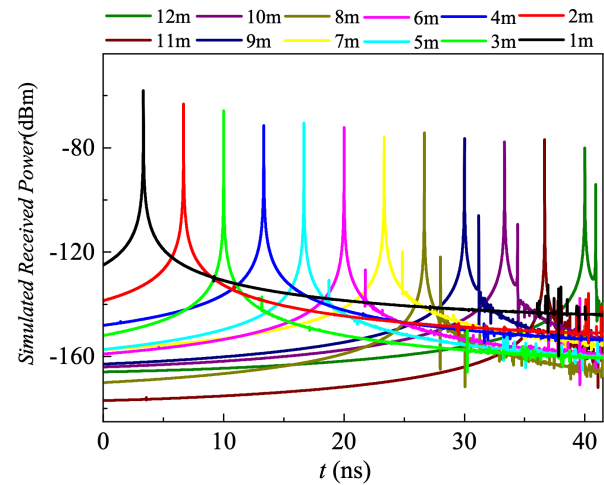
The RT simulations were conducted using the cloudRT modelling tool, which uses detailed environmental geometries and frequency-appropriate material parameters to predict the sub-THz propagation response. Both simulated and experimental campaigns used directional horn antennas with a gain of 26 dBi and a HPBW of 10°, ensuring consistency between modelled and measured setups. Enabled by the flexibility of the simulation software for some cases an omni-direction antenna results are also shown. There are currently no omni-directional antennas available for the 750 GHz waveguide standard so these results cannot be compared directly to a measured result. The simulation model of the indoor environment (Figure 95) was constructed to closely replicate the physical measurement laboratory at the National Physical Laboratory, where channel sounding was performed at separation distances ranging from 0 mm to 250 mm.

Initial validation focused on a short-range line-of-sight (LOS) configuration with Tx and Rx antennas aligned on a tabletop. The time-domain comparison between simulated and measured S-parameters (Figure 96) revealed a close

correspondence in LOS peak positions and amplitude levels. A minor temporal discrepancy of approximately 0.02 ns between simulated and measured LOS peaks was identified, attributed primarily to systematic factors such as phase centre offsets within the antennas and potential calibration or distance measurement uncertainties.



(a)



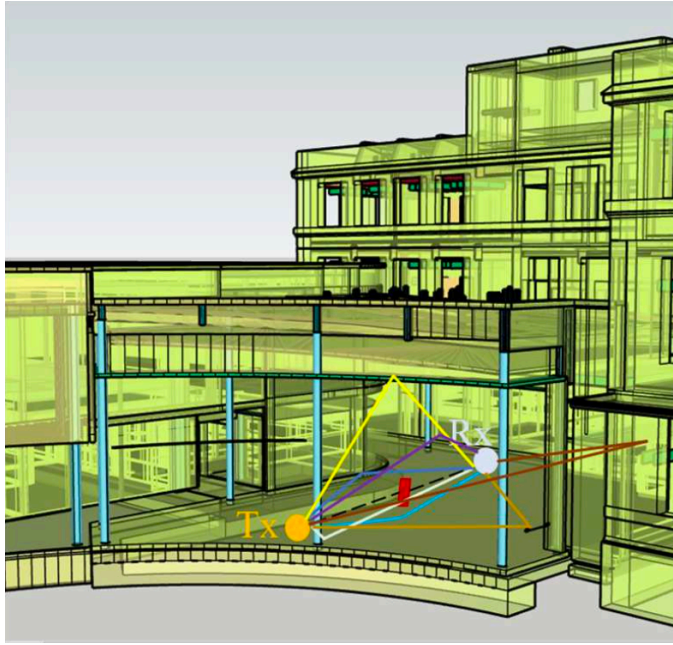
(b)

Figure 97: (a) Ray-tracing simulated 3D path-with horn antenna, including Tx and Rx antennas and Path 1 (black) and Path 2(cyan) overlaid (b) Ray-tracing simulated results

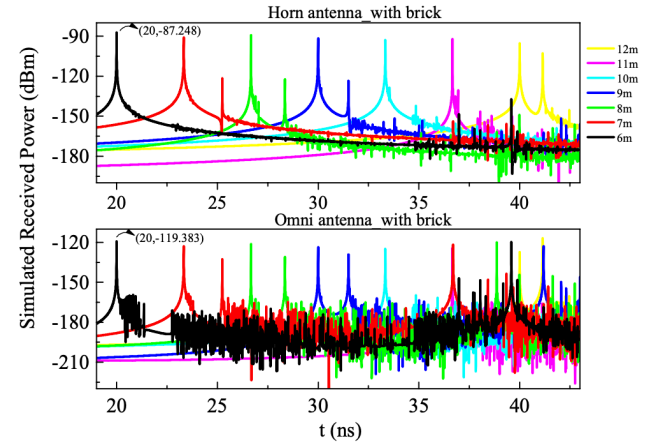
Subsequent simulations address longer-range indoor atrium scenarios, with Tx-Rx separations extending to 12 meters. The dimensions of the building and antenna positions is shown in Figure 97a. The RT simulations captured the progressive attenuation of the LOS path and the emergence of reflection paths with increasing distance, as presented in Figure 97b. The magnitude of the primary reflection (Path 2) grew in significance relative to the LOS path, particularly as antenna separation increased, consistent with experimental observations. The comparative results validate the model's ability to represent multipath dynamics under realistic conditions, for the first order reflection case.

The RT scenario was then repeated with the introduction a 1 m × 1 m brick obstruction midway between the Tx and Rx antennas to emulate a NLOS environment. The scenario shown in Figure 98a, tests the presence of the obstruction which alters the dominant propagation mechanism from direct transmission to one governed by material penetration, reflection, and scattering. Simulation results, in figure 98b indicate an increased attenuation in the main received peak (approximately 15 dB relative to LOS) and the introduction of a larger number of multipath components. These findings were supported by empirical data, confirming the model's accuracy in representing obstructed propagation conditions at sub-THz frequencies.

The RT tools are able to provide a path-resolved analysis to identify the type of received multipath components in the obstructed environment. Figure 99 presents both top and front views of the modelled building, along with annotated first-order and second-order reflection paths, as well as prominent scattering paths. Path delay spectra and amplitude levels are shown in Figure 99e and 99f with first-order reflection paths denoted by Arabic numerals, while the second-order reflection paths are denoted by Roman numerals I,II, III. Lowercase letters represent scattering



(a)



(b)

Figure 98: (a) Ray-tracing simulated 3D path-with omni-directional antenna (b) Ray-tracing simulated results

paths (Note that for convenience, scattering paths have been simplified to a single path instead of multiple paths; typically, they form a dense beam scattered on the wall).

To allow for comparison between the measured results and the simulated results for an identical measurement scenario the Atrium environment has been selected. The results presented in 2.6.1.2, 56, are overlaid the the matched RT simulation results in red. The first analysis focuses on the LOS path; for all the measurement locations the simulated results matches the measured results in both time and magnitude. The LOS case is the most simple for the simulation tool as there are limited material properties and environmental effects to include. The significant effect on the LOS simulation comes from the accuracy of locating the antennas within the 3D simulation model. Next, for measurements with an distinct 1st order reflection peak in the measured CIR (e.g. figure 56b) these are also usually well modelled by the simulation tool, with peaks aligned in magnitude and time. Also simulated are the 2nd order and diffraction effects, however these have little correlation with the measured results. These two propagation methods are the smallest contributor the the measured CIR results and as such are acceptable to be omitted for this analysis.

In conclusion, the simulation results exhibit strong agreement with empirical measurements across both LOS and NLOS indoor scenarios. The RT platform was shown to reliably predict key propagation characteristics, including LOS peak alignment, attenuation trends, and some multipath behaviour. This validation confirms the efficacy of the simulation approach and reinforces its suitability for characterizing sub-THz channels in complex indoor environments.

4.6 Conclusion

In this chapter, deterministic RT modeling of the THz channel model is proposed and performed. High propagation loss, sparsity, NF and spatial non-stationarity have been reviewed and properly considered in the channel modeling. A RT-based channel modeling methodology is suggested, and its performance is investigated by comparing

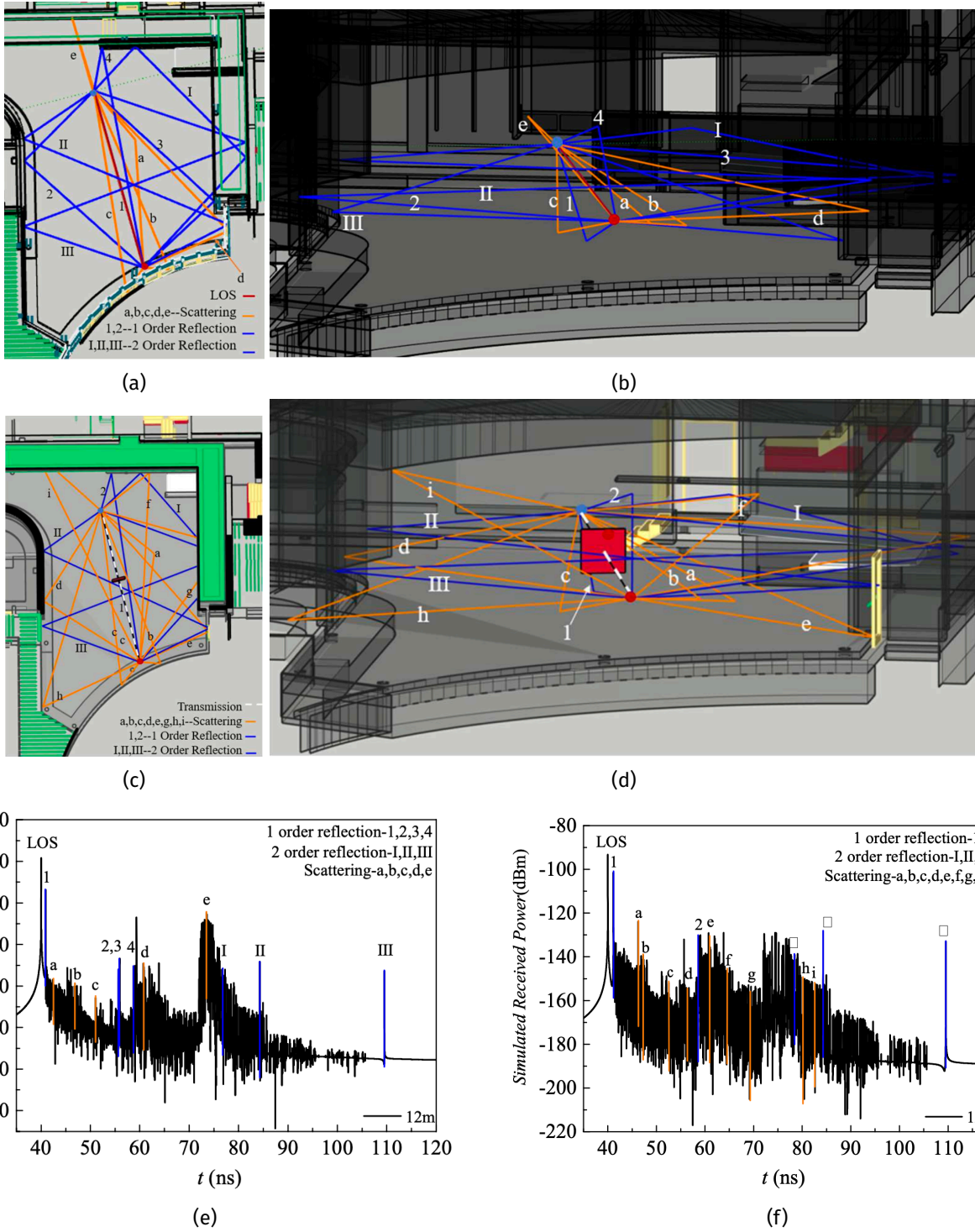



Figure 99: Simulated Rays plotted within the model of the Atrium scenario for the LOS (a, b) and NLOS (c, d) cases. The simulated CIR with the paths overlaid for the (e) LOS and (f) NLOS scenarios.



measurements and simulations in two indoor typical scenarios, i.e., the empty room and the spacious hall. A good agreement is achieved between the measurements and RT simulations for both investigated scenarios. Future work may include more accurate measurement-calibrated RT channel model, more measurements to calibrate the EM properties of materials more precisely in RT simulation and more various measurement (simulation) scenarios.

5. Conclusion

The first key contributions in Chapter 2 are the development of novel channel sounder designs for sub-THz frequency bands, which are critical for B5G and toward 6G wireless communication systems. Traditional channel sounders face significant limitations at these high frequencies, necessitating innovative designs that offer improved resolution, dynamic range, and real-time processing capabilities. Firstly, channel sounder architectures covering respectively the (75 and 110) GHz and (220-330) GHz are proposed. Their analysis includes link budget estimations and information on system calibration. Further, a RoF technique and a novel phase compensation scheme for a channel sounder at (220-330) GHz have been proposed and their effectivenesses were analyzed.

The second important aspect in Chapter 2 are the conducted measurement campaigns across different deployment scenarios at 100 GHz and 300 GHz by deploying VAA, DSS and DDSS schemes and the presented respective measurement results. By providing key insights into the propagation characteristics at sub-THz frequencies, these measurements are crucial for understanding the feasibility of high-frequency wireless communication and optimizing antenna and beamforming techniques for B5G and toward 6G networks. The results indicate that Omni-VAA provides a broad, but less directive channel characterization, making it useful for initial large-scale propagation studies. However, its lack of directional selectivity results in higher PL and increased multipath interference, which may limit its effectiveness in highly dynamic environments. On the other hand, Dir-VAA enhances measurement precision by focusing on specific propagation paths, reducing interference and improving signal clarity. This method is proved particularly to be effective in urban and indoor environments, where LOS and NLOS conditions vary significantly.

Lastly, Chapter 2 contains DDSS sub-THz channel measurements at 300 GHz in a large hall scenario providing valuable insights into the channel characteristics in both LoS and NLoS conditions. The measurements reveal that the LoS path exhibits a strong concentration of power around the LoS direction, with a decrease in power observed as the measurement distance increases. This decrease is associated with an increase in the number of MPCs, which become more prominent in the NLoS scenarios due to the blocking of the LoS path. These results show that the multipaths are sparse and specular in nature, with the angular spreads in the NLoS cases being significantly larger than in the LoS cases. The empirical PL data, which shows a good agreement with the theoretical FSPL model, highlights the accuracy of the measurement setup. The delay spreads in the LoS cases are found to increase with the Tx-Rx distance, suggesting that the decrease in LoS power leads to the closer power levels of the MPCs, making them more comparable. In the NLoS cases, the angular spread and delay spread are more pronounced, as the LoS path is blocked and the contribution of the MPCs becomes dominant. Additionally, the PAS comparisons across different Rx locations show that the MPCs contribute significantly to the angular spread in NLoS scenarios, while in LoS scenarios, the power is more focused, leading to smaller angular spreads. The measurements also confirm the sparse and specular nature of the channel, particularly at the high-frequency 300 GHz band. These findings underscore the importance of conducting further long-range 300 GHz channel measurements to enhance the understanding of propagation characteristics at sub-THz frequencies, especially in scenarios that involve both LoS and NLoS conditions. The measurement results provide a solid foundation for future research in the field, with implications for the design and optimization of communication systems operating in the 300 GHz band.

Chapter 3 explores the challenges and advancements in enabling high-fidelity UWB radio channel emulation, particularly focusing on band-stitching and DP techniques. The need for effective radio CEs is highlighted, especially as wireless communication technologies evolve to support wider bandwidths, such as the 400 MHz bandwidth used

in 5G NR systems. Existing commercial CEs, which can typically support emulation bandwidths of up to 160 MHz, face limitations when attempting to emulate broader bandwidths. To address this, the band-stitching technique is proposed, wherein multiple digital channels are combined to simulate a wider bandwidth. This process requires careful calibration to ensure phase and amplitude coherence between the adjacent channels, a task traditionally done through time-consuming trial-and-error methods. However, these conventional calibration techniques have their limitations, including reduced accuracy and time inefficiency. To improve this process, a novel DP scheme is introduced, based on MMSE equalization. This approach enhanced the accuracy of the channel emulation by compensating for the intrinsic distortions of the CE, ensuring that the emulated channel closely matches the target channel's frequency response. The pre-distortion method is found to be particularly beneficial in band-stitching, as it corrects the intrinsic frequency response of the digital channels, making it closer to the ideal raised-cosine shape, which is crucial for achieving high-fidelity emulation. Through examples and numerical simulations, it is demonstrated that the DP improves the performance of band-stitching, leading to more accurate and reliable channel emulation. The results show that pre-distortion significantly reduces deviations in both magnitude and phase compared to traditional calibration methods. Overall, the DP approach offers a promising solution to achieve high-fidelity UWB channel emulation, which is critical for the testing and validation of next-generation wireless devices.

Moreover, Chapter 3 delves into the challenges of wideband vector measurements for the 5G NR signals, especially given the significant increase in bandwidths, i. e. from 20 MHz in 4G LTE to 400 MHz in 5G FR2. As wider bandwidths demand higher analysis bandwidth from measurement instrumentation, many existing commercial instruments become insufficient for these tasks. To address this, methods for extending the measurement bandwidth without hardware modifications have been proposed, particularly focusing on time-interleaved and frequency-interleaved approaches. The concept of band stitching is central for solving this problem. This technique is utilized in various applications like channel sounding, emulation, and signal generation, where it allows multiple sub-bands of a signal to be measured and then stitched together to form a wider effective bandwidth. Band stitching involves several critical steps: spectrum division, sub-band sampling, interpolation and mixing, sub-band impairments calibration, and finally, sub-band stitching. These steps can be organized into two main configurations: sequential and parallel structures, each with its own advantages and challenges, particularly in dealing with impairments like timing, magnitude, and initial phase. Both configurations are explored for VSAs, comparing their effectiveness. It also emphasizes the importance of precise estimation and correction of sub-band impairments, especially timing errors. To improve timing accuracy, a two-step delay estimation method is proposed, which refines the common circular cross-correlation technique. By addressing these challenges, the band stitching method allows wideband signals to be effectively measured and analyzed, making it a crucial tool for the development and testing of modern 5G NR systems.

Lastly, Chapter 3 focuses on the experimental validation and applications of an 8×8 AiP array platform designed for mmWave communications. As 5G communications expand into the mmWave frequency bands (28–73 GHz), they promise significant increases in wireless data transmission speed. However, challenges such as high PL and low SNR at these frequencies limit the effectiveness of these systems. Directional high-gain antennas can be used to overcome these limitations, but they come with the trade-off of reduced coverage area, necessitating beam-tracking for reliable communication in dynamic environments. Phased array systems can be a solution to this challenge, allowing for real-time beam steering to track dominant propagation paths. The AiP technology integrates antennas and control circuits into a single package, offering benefits like small size, low cost, low power consumption, and fast beam-steering capabilities. The presented 8×8 AiP array operates between 26.5 and 29.5 GHz with various features such as 6-

bit phase shifters, attenuators, and power amplifiers for both Tx and Rx modes. The experimental setup includes calibration and beamforming measurements in a CATR. The results show that the AiP array is stable, with temperature playing a significant role in the stability of the array's elements. Calibration methods, including "inverse," "on-off," and "least squares" methods, were evaluated for large arrays. The "inverse" method proved ineffective for large arrays due to the impact of measurement noise, while the "least squares" method was more reliable. Additionally, the AiP was used in mmWave channel sounding experiments to evaluate its ability to detect the LOS propagation path. The channel frequency response was measured using a VNA, and beam-steering control enabled precise channel sounding. The results demonstrated the effectiveness of the AiP-based channel sounder in detecting the dominant propagation components, such as AoA, AoD, and delay.

Chapter 4 discusses the use of RT simulations for modeling THz communication channels, considering special features as high propagation loss, sparsity, NF and spatial non-stationarity. Special attention has been put on the calibration of RT simulations using measurement data to achieve higher accuracy in channel characteristics, such as power, delay, AoA and AoD. The calibration process involves adjusting the EM properties of the materials in the simulation until the results from the RT simulation closely matches the measurement data, minimizing errors in key parameters. The effectiveness of the measurement-calibrated RT simulations is demonstrated for two scenarios - empty room and spacious hall. In the case of an empty room scenario, the measurements are carried out at 100 GHz, with a 6 GHz bandwidth. The Tx uses a vertically polarized omnidirectional antenna, and the Rx uses a virtual UCA with 2400 elements. The distance between Tx and Rx is 6.5 meters. Ray trajectories in the empty room show that the dominant paths come from first-order and second-order reflections. The received power generally decreases as the reflection order increases. A good match between the measured and RT-simulated results is achieved, especially for the dominant propagation paths in terms of power, delay, and angle. The delay differences between the three dominant paths are within 0.1 ns, and the power differences are within ± 0.3 dB. In the case of a spacious hall scenario, the measurements are conducted at 300 GHz, with a 2 GHz bandwidth. Horn antennas are used at both Tx and Rx ends, with Tx and Rx rotations to capture various angle-dependent propagation effects. The dominant paths come from the LOS path and reflections off adjacent columns. The RT simulation results show good agreement with the measurements for both spatial and delay domains. The delay differences for the five dominant paths are within ± 2 ns, and the maximum differences for AoA, AoD, delay, and power gain were all within reasonable bounds (e.g., -1.8° , 0.7 ns, -0.7 dB). Future work will focus on improving the calibration process, obtaining more precise measurements of the EM properties of materials, and applying this method to a wider variety of deployment scenarios. This research paves the way for more accurate THz channel modeling that can aid in the development of advanced communication systems.

6. Appendix

Chapter 3, containing different measurements for channel characterization, uses lots of common equations. Therefore, it is useful to include all used fundamental equations in this section. When a specific equation is used to calculate a channel parameter (or characteristic), then the reader is referred to this section.

The measurements are conducted within the $[f_{min}, f_{max}]$ frequency band, where f_{min} and f_{max} can be specified respectively as the minimum and maximum frequencies. Then, the bandwidth (BW) of the measured signal is:

$$BW = f_{max} - f_{min} \quad (6.1)$$

The delay resolution $\Delta\tau$ (i.e. the interval between the two adjacent delay samples) is:

$$\Delta\tau = \frac{1}{BW} \quad (6.2)$$

The frequency step is related to the chosen number of frequency points by:

$$\Delta f = \frac{BW}{N_f} \quad (6.3)$$

Then, the maximum excess delay is:

$$\tau_{max} = \frac{1}{\Delta f} \quad (6.4)$$

When using directional antennas for both the Tx and Rx on a rotational table, the CIR can be characterized by the delay τ , the AOA θ , and the AOD ϕ . Therefore, the CIR can be written in the form:

$$h(\tau, \theta, \phi) = \sum_{l=1}^L \alpha_l \delta(\tau - \tau_l) \delta(\phi - \phi_l) \delta(\theta - \theta_l) \quad (6.5)$$

A PDP is calculated by maximizing over all angles for each delay:

$$PDP(\tau) = \max_{\phi} \max_{\theta} |h(\tau, \phi, \theta)|^2 \quad (6.6)$$

The PADP is obtained by the maximum the power for each θ Rx rotations over all ϕ Tx rotation:

$$PADP(\tau, \theta) = \max_{\phi} |h(\tau, \phi, \theta)|^2 \quad (6.7)$$

PAS is calculated by summing the delay for each Tx and Rx angles:

$$PAS(\phi, \theta) = \sum_{N_{\tau}} |h(\tau, \phi, \theta)|^2 \quad (6.8)$$

The average delay μ_{DS} of the PDP can be calculated as:

$$\mu_{DS} = \frac{\sum_{\tau} \tau PDP(\tau)}{\sum_{\tau} PDP(\tau)} \quad (6.9)$$

The root mean squared (rms) delay spread σ_{DS} of the PDP is calculated via:

$$\sigma_{DS} = \sqrt{\frac{\sum_{\tau} (\tau - \mu_{DS})^2 PDP(\tau)}{\sum_{\tau} PDP(\tau)}} \quad (6.10)$$

The AoA angular spread is calculated as the second central-moment of the azimuth-power:

$$\sigma_{\theta} = \sqrt{\frac{\sum_{\theta} (\theta - \mu_{\theta})^2 P(\theta)}{\sum_{\theta} P(\theta)}} \quad (6.11)$$

where the mean azimuth μ_{θ} is calculated as,

$$\mu_{\theta} = \frac{\sum_{\theta} P(\theta)}{\sum_{\theta} P(\theta)} \quad (6.12)$$

The Friis equation defines the FSPL as:

$$FSPL = 20 * \log_{10} \left(\frac{4\pi f_c d}{c} \right) \quad (6.13)$$

where f_c is the center frequency of the transmitted signal, c is the speed of light and d represents the link distance between the Tx and Rx.

The PL can be calculated as the power summation of the estimated path power. The calculated PL results can be fitted by the log-distance dependent PL model, i.e., alpha-beta-gamma (ABG) model:

$$PL_{ABG}(d)[dB] = 10 \cdot n_{ABG} \cdot \log_{10} \left(\frac{d}{d_0} \right) + PL(d_0) + \chi_{\sigma}^{ABG} \quad (6.14)$$

where PL_{ABG} denotes the ABG path PL over distance. As in the previous equation, d is the Tx-Rx distance with $d \geq 1$ m and $d_0 = 1$ m; n_{ABG} is the PL coefficient, $PL(d_0)$ is the optimized offset value for PL. χ_{σ}^{ABG} is the large-scale signal fluctuations.

Note that the Fraunhofer distance to distinguish the NF or FF is defined as:

$$d_{far} = 2D^2/\lambda \quad (6.15)$$

where D is the largest dimension of the single antenna. In the case of VAA and most particular UCA, $D=2R$ denotes the array aperture of the VAA. R is the radius of the UCA. λ is the wavelength at the carrier frequency.

The estimated PL from the measurements can be also matched with the floating intercept model, also referred to as the alpha-beta (AB) PL model:

$$PL_{AB}(d) = 10 \cdot \alpha \cdot \log_{10} (d/d_0) + \beta + \chi_{\sigma}^{AB} \quad (6.16)$$

where $PL_{AB}(d)$ [dB] denotes the AB PL model as a function of distance. The Tx-Rx distance is denoted as d [m], where d is constrained to $d \geq 1$, m, and a reference distance of $d_0 = 1$ m is also used. α and β correspond respectively to the PL exponent and the optimized intercept for the PL curve. χ_{σ}^{AB} is the large-scale signal fluctuations (i.e., shadowing), which is commonly modeled as a zero-mean normal distribution as $\chi_{\sigma}^{AB} \sim \mathcal{N}(0, \sigma_{\chi}^2)$, where σ_{χ} is the standard deviation of the shadowing.

References

- [1] Yejian Lyu, Pekka Kyösti, and Wei Fan. "Sub-THz VNA-based Channel Sounder Structure and Channel Measurements at 100 and 300 GHz". In: *IEEE 32nd Annual International Symposium on Personal, Indoor and Mobile Radio Communications (PIMRC)* (2021).
- [2] Yejian Lyu et al. "Design and Validation of the Phase-Compensated Long-Range Sub-THz VNA-based Channel Sounder". In: *IEEE Antennas and Wireless Propagation Letters* 20.12 (2021), pp. 2461–2465.
- [3] Allan Wainaina Mbugua et al. "Phase-compensated optical fiber-based ultrawideband channel sounder". In: *IEEE Transactions on Microwave Theory and Techniques* 68.2 (2020), pp. 636–647.
- [4] Wei Fan, Allan Wainaina Mbugua, and Kim Olesen. "Accurate channel sounding with a phase stabilizing scheme". In: *XXXIIIrd General Assembly and Scientific Symposium of the International Union of Radio Science* (2020).
- [5] M Mechaik. "Signal attenuation in transmission lines". In: *2nd International Symposium on Quality Electronic Design* (2001), pp. 191–196.
- [6] M Calhoun, S Huang, and R L Tjoelker. "Stable photonic Links for Frequency and Time Transfer in the Deep-Space Network and Antenna Arrays". In: *IEEE Transactions on Microwave Theory and Techniques* 95.10 (2007), pp. 1931–1946.
- [7] Lawrence Carslake, James Skinner, and Tian Hong Loh. "Design and Preliminary Indoor Assessment of a Long-Range sub-THz VNA-based Channel Sounder between 500 GHz and 750 GHz". In: *18th European Conference on Antennas and Propagation (EuCAP 2024)* (2024).
- [8] Yejian Lyu et al. "Virtual Antenna Array Based Channel Sounding at 300 GHz: Implementation and Field Measurements". In: *IEEE Antennas and Wireless Propagation Letters* 23.12 (2024), pp. 4174–4178.
- [9] Mengting Li et al. "Antenna Deembedding in Directional Channel Measurements with Virtual Array Concept and Experimental Validation". In: *IEEE Transactions on Antennas and Propagation* 72.1 (2024), pp. 1063–1068.
- [10] Yejian Lyu et al. "Virtual Antenna Array for W-Band Channel Sounding: Design, Implementation, and Experimental Validation". In: *IEEE Journal of Selected Topics in Signal Processing* 17.4 (2023), pp. 729–744.
- [11] Yejian Lyu et al. "Enabling Long-Range Large-Scale Channel Sounding at Sub-THz Bands: Virtual Array and Radio-Over-Fiber Concepts". In: *IEEE Communications Magazine* 62.2 (2024), pp. 16–22.
- [12] J Noda, K Okamoto, and Y Sasaki. "Polarization-Maintaining Fibers and Their Applications". In: *Journal of Lightwave Technology* 4.8 (1986), pp. 1071–1089.
- [13] V Budinski and D Donlagic. "Fiber-Optic Sensors for Measurements of Torsion, Twist and Rotation: A Review". In: *Sensors* 17.3 (2017).
- [14] Fengchun Zhang and Wei Fan. "Near-Field Ultra-Wideband mmwave Channel Characterization Using Successive Cancellation Beamspace UCA Algorithm". In: *IEEE Transactions on Vehicular Technology* 68.8 (2019), pp. 7248–7259.
- [15] S L H Nguyen et al. "Comparing Radio Propagation Channels between 28 and 140 GHz Bands in a Shopping Mall". In: *12th European Conference on Antennas and Propagation* (2018).
- [16] T Niiho et al. "Multi-Channel Wireless LAN Distributed Antenna System Based on Radio-Over-Fiber Techniques". In: *The 17th Annual Meeting of the IEEE Lasers and Electro-Optics Society* (2004), pp. 57–58.
- [17] R Sambaraju et al. "Impact of Channel Characteristics on the Performance of a 60 GHz Radio Over Fiber (RoF) System". In: *2008 International Topical Meeting on Microwave Photonics* (2011), pp. 157–160.
- [18] I Oppermann, J Talvitie, and D Hunter. "Wide-Band Wireless Local Loop Channel for Urban and Sub-Urban Environments at 2 GHz". In: *IEEE International Conference on Communications* (1997), pp. 61–65.

- [19] L Tarlazzi et al. "Characterization of an Interleaved F-DAS MIMO Indoor Propagation Channel". In: *Loughborough Antennas and Propagation Conference (LAPC)* (2010), pp. 505–508.
- [20] Antenna. "W-band omnidirectional antenna". In: Available: <https://sftp.eravant.com/content/datasheets/SAO-7531140230-10-S1.pdf> (2025).
- [21] Antenna. "Flann standard gain horn antenna 27240-20". In: Available: <https://flann.com/products/antennas/standard-gain-horns-series-240/> (2025).
- [22] N A Abasi et al. "Double Directional Channel Measurements for THz Communications in an Urban Environment". In: *IEEE International Conference on Communications* (2020), pp. 1–6.
- [23] Yejian Lyu et al. "Large Virtual Antenna Array-Based Empirical Channel Characterization for Sub-THz Indoor Hall Scenarios". In: *IEEE Transactions on Antennas and Propagation* (2023).
- [24] N Czink and C Mecklenbrauker. "A Novel Automatic Cluster Tracking Algorithm". In: *IEEE 17th International Symposium on Personal, Indoor and Mobile Radio Communications* (2006), pp. 1–5.
- [25] L Greenstein, D Michelson, and V Erceg. "Moment-Method Estimation of the Ricean k-factor". In: *IEEE Communications Letters* 3.6 (1999), pp. 175–176.
- [26] N A Abbasi et al. "THz Band Channel Measurements and Statistical Modeling for Urban D2D Environments". In: *IEEE Transactions on Wireless Communications* 22.3 (2023), pp. 1466–1479.
- [27] 3GPP. "Study on Channel Model for Frequencies from 0.5 to 100 GHz". In: *3GPP, Technical Report V17.0.0* (2022).
- [28] T S Rappaport and Y Xing et al. "Wireless Communications and Applications Above 100 GHz: Opportunities and Challenges for 6G and Beyond". In: *IEEE Access* 7 (2019), pp. 78 729–78 757.
- [29] Z Ma and B Ai et al. "A Non-Stationary Geometry-Based MIMO Channel Model for Millimeter-Wave UAV Networks". In: *IEEE Journal on Selected Areas in Communications* 39.10 (2021), pp. 2960–2974.
- [30] Z Huang and X Cheng. "A General 3D Space-Time Frequency Non-Stationary Model for 6G Channels". In: *IEEE Transactions on Wireless Communications* 20.1 (2021), pp. 535–548.
- [31] Y Yuan and R He et al. "A 3D Geometry-Based THz Channel Model for 6G Ultra Massive MIMO Systems". In: *IEEE Transactions on Vehicular Technology* 71.3 (2022), pp. 2251–2266.
- [32] A Parssinen and M S Alouini et al. "White Paper On RF Enabling 6G – Opportunities and Challenges from Technology to Spectrum". In: *6G Flagship Ecosystem* <https://www.6gchannel.com/items/6g-white-paper-rf-spectrum/> (2021).
- [33] J Zhang and P Tang et al. "Channel Measurements and Models for 6G: Current Status and Future Outlook". In: *Frontiers of Information Technology and Electronic Engineering* 21.1 (2020), pp. 39–61.
- [34] Mikkel Bengtson, Yejian Lyu, and Wei Fan. "Long-range VNA-based channel sounder: Design and measurement validation at MmWave and sub-THz frequency bands". In: *China Communications* 19.11 (2022), pp. 47–59.
- [35] S Priebe and M Kannicht et al. "Ultra Broadband Indoor Channel Measurements and Calibrated Ray Tracing Propagation Modeling at THz Frequencies". In: *Journal of Communications and Networks* 15.6 (2023), pp. 547–558.
- [36] E M Vitucci and M Zoli et al. "Tri-Band mm-wave Directional Channel Measurements in Indoor Environment". In: *29th Annual International Symposium on Personal, Indoor and Mobile Radio Communications (PIMRC)* (2018), pp. 205–209.
- [37] K Guan and B Peng et al. "Channel Characterization for Intrawagon Communication at 60 and 300 GHz Bands". In: *IEEE Transactions on Vehicular Technology* 68.6 (2019), pp. 5193–5207.
- [38] Heng and S Sangodoyin et al. "THz Cluster-Based Modeling and Propagation Characterization in a Data Center Environment". In: *IEEE Access* 8 (2020), pp. 56 544 –56 558.

- [39] Y Zantah and F Sheikh et al. "Channel Measurements in Lecture Room Environment at 300 GHz". In: *Second International Workshop on Mobile Terahertz Systems (IWMTS)* (2019), pp. 1–5.
- [40] L Pometcu and R D'Errico. "An Indoor Channel Model for High Data-Rate Communications in D-Band". In: *IEEE Access* 8 (2020), pp. 9420–9433.
- [41] N A Abbasi and J Gomez-Ponce et al. "Ultra-Wideband Double Directional Channel Measurements for THz Communications in Urban Environments". In: *IEEE International Conference on Communications* (2021), pp. 1–6.
- [42] Yejian Lyu et al. "Measurement-based channel characterization in a large hall scenario at 300 GHz". In: *China Communications* 20.4 (2023), pp. 118–131.
- [43] Keysight Technology. "Santa Rosa CA USA S8709A, Virtual Drive Test Toolset". In: [Online] Available: <https://www.keysight.com/5g-virtual-drive-test-toolset.html> (2025).
- [44] M Charitos et al. "LTE-A Virtual Drive Testing for Vehicular Environments". In: *IEEE* (2017), pp. 1–5.
- [45] Yilin Ji et al. "Virtual Drive Testing Over-the-Air for Vehicular Communications". In: *IEEE Transactions on Vehicular Technology* 69.2 (2020), pp. 1203–1213.
- [46] M Rumney. "Testing 5G: Time to Throw Away the Cables". In: *Microwave Journal* 59.11 (2016), pp. 10–18.
- [47] T Eichler et al. "Virtual Cable Calibration for OTA Testing of 5G mmWave Devices". In: *Microwave Journal* 64.5 (2021), pp. 1–5.
- [48] Spirent vertex channel emulator Data Sheet Spirent Crawley UK. "Available: https://www.spirent.com/assets/u/spirent_vertex_channel_emulator_data_sheet.pdf". In: *Virtual Cable Calibration for OTA Testing of 5G mmWave Devices* (2025).
- [49] PropSim F8 channel emulator. "Data Sheet". In: *Keysight Technology Santa Rosa CA USA 2016* (2016).
- [50] J J Olmos et al. "Design and Implementation of a Wide-Band Real-Time Mobile Channel Emulator". In: *IEEE Transactions on Vehicular Technology* 48.3 (1999), pp. 746–764.
- [51] N Zhang, G Yang, and J Zhai. "A Low Complexity Emulation Scheme for 5G Millimeter-Wave Massive MIMO Channel". In: *Microwave and Optical Technology Letters* 59.6 (2017), pp. 1300–1305.
- [52] A Schwind et al. "Implementation of a MIMO Channel Emulator for Over-the-Air LTE Testing Using Software Defined Radio". In: *German Microwave Conference* (2018), pp. 307–310.
- [53] M Hofer et al. "Real-Time Geometry-Based Wireless Channel Emulation". In: *IEEE Transactions on Vehicular Technology* 68.2 (2019), pp. 1631–1645.
- [54] NR. "User Equipment (UE) radio transmission and reception". In: *Part 2: Range 2 Standalone, V17.1.0, 3GPP Standard TS 38.101-2* (2021).
- [55] Wei Fan et al. "A Flexible Millimeter-Wave Radio Channel Emulator Design with Experimental Validations". In: *IEEE Transactions on Antennas and Propagation* 66.11 (2018), pp. 6446–6451.
- [56] Yilin Ji, Wei Fan, and Gert Frølund Pedersen. "Wideband Radio Channel Emulation Using Band-Stitching Schemes". In: *14th European Conference on Antennas and Propagation (EuCAP)* (2020), pp. 1–5.
- [57] J Cao, F Tila, and A Nix. "Wideband RF Channel Emulation Platform for 5G mmWave Systems". In: *Middle East North Africa Communications Conference* (2019), pp. 5–9.
- [58] J Cao, F Tila, and A Nix. "Design and Implementation of a Wideband Channel Emulation Platform for 5G mmWave Vehicular Communication". In: *IET Communications* 14.14 (2020), pp. 2369–2376.
- [59] 3GPP. "Study on Channel Model for Frequencies From 0.5 to 100 GHz". In: *3GPP Standard TR 138 901* (2020).
- [60] W Rummeler. "A New Selective Fading Model: Application to Propagation Data". In: *Bell System Technical Journal* 58.5 (1979), pp. 1037–1071.

- [61] Yilin Ji and Wei Fan. “Enabling High-Fidelity Ultra-Wideband Radio Channel Emulation: Band-Stitching and Digital Predistortion Concepts”. In: *IEEE Open Journal of Antennas and Propagation* 3 (2022), pp. 932–939.
- [62] NR. “Base Station (BS) Radio Transmission and Reception”. In: *Version 15.2.0, 3rd Generation Partnership Project* (2019).
- [63] W C Black and D A Hodges. “Time Interleaved Converter Arrays”. In: *IEEE Journal of Solid-State Circuits* SSC-15.6 (1980), pp. 1022–1029.
- [64] M Seo, M J W Rodwell, and U Madhow. “Comprehensive Digital Correction of Mismatch Errors for a 400-Msamples/s 80-dB SFDR Time-Interleaved Analog-to-Digital Converter”. In: *IEEE Transactions on Microwave Theory and Techniques* 53.3 (2005), pp. 1072–1082.
- [65] S L Dark and C N White. “Time Sequenced Spectral Stitching”. In: *WO Patent 2018 045 201 A1* (2018).
- [66] E M Barich. “Method and System for Performing Vector Spectral Measurements of a Radio Frequency (RF) Signal Having a Repetitive Waveform”. In: *US Patent 9 851 383 B1* (2017).
- [67] S L Dark, D J Baker, and J R Ammerman. “Spectral Stitching Method to Increase Instantaneous Bandwidth in Vector Signal Analyzers”. In: *US Patent 9 326 174 B1* (2016).
- [68] G Feldhaus, A Roth, and M Ruengeler. “Test and Measurement Device, Method for Calibrating a Test and Measurement Device as Well as Method for Analyzing a High Bandwidth of a Radio Frequency Signal”. In: *US Patent 10 436 826 B2* (2019).
- [69] D Wisell, D Rönnow, and P Händel. “A Technique to Extend the Bandwidth of An RF Power Amplifier Test Bed”. In: *IEEE Transactions on Instrumentation and Measurement* 56.4 (2007), pp. 1488–1494.
- [70] K A Remley et al. “Measurement Bandwidth Extension Using Multisine Signals: Propagation of Error”. In: *IEEE Transactions on Microwave Theory and Techniques* 58.2 (2010), pp. 458–467.
- [71] Yilin Ji, Jesper Ødum Nielsen, and Wei Fan. “On Band Stitching for Wideband Vector Measurements With Vector Signal Analyzers”. In: *IEEE Transactions on Microwave Theory and Techniques* 71.2 (2023), pp. 710–718.
- [72] C U Bas et al. “Real-Time Ultra-Wideband Channel Sounder Design for 3-18 GHz”. In: *IEEE Transactions on Communications* 67.4 (2019), pp. 2995–3008.
- [73] L Wen et al. “Frequency Quasi-Linear Swept Light Source Based on Multi-Frequency Time-Matched Spectrum Stitching”. In: *IEEE Photonics Journal* 12.6 (2020).
- [74] Rohde and Schwarz. “FSW I/Q Analyzer and I/Q Input Interfaces User Manual”. In: *Rohde and Schwarz* (2020).
- [75] NR. “Base Station (BS) Conformance Testing Part 1: Conducted Conformance Testing”. In: *document 3GPP TS 38.141-1, Version 16.1.0, 3rd Generation Partnership Project* (2019).
- [76] NR. “Physical Channels and Modulation”. In: *document 3GPP TS 38.211, Version 16.6.0, 3rd Generation Partnership Project* (2021).
- [77] P D Welch. “The Use of Fast Fourier Transform for the Estimation of Power Spectra: A Method Based on Time Averaging Over Short, Modified Periodograms”. In: *IEEE Transactions on Audio and Electroacoustics* AU-15.2 (1967), pp. 70–73.
- [78] I A Hemadeh et al. “Millimeter-Wave Communications: Physical Channel Models, Design Considerations, Antenna Constructions, and Link-Budget”. In: *IEEE Communications Surveys and Tutorials* 20 (2018), pp. 870–913.
- [79] K Guan et al. “Towards Realistic High-Speed Train Channels at 5G Millimeter-Wave Band—Part I: Paradigm, Significance Analysis, and Scenario Reconstruction”. In: *IEEE Transactions on Vehicular Technology* 67 (2018), pp. 9112–9128.

-
- [80] M Agiwal, A Roy, and N Saxena. "Next Generation 5G Wireless Networks: A Comprehensive Survey". In: *IEEE Communications Surveys and Tutorials* 18 (2016), pp. 1617–1655.
- [81] A Ghosh et al. "Millimeter-Wave Enhanced Local Area Systems: A High-Data-Rate Approach for Future Wireless Networks". In: *IEEE Journal on Selected Areas in Communications* 32 (2014), pp. 1152–1163.
- [82] S Liao et al. "Differentially Fed Planar Aperture Antenna With High Gain and Wide Bandwidth for Millimeter-Wave Application". In: *IEEE Transactions on Antennas and Propagation* 63 (2015), pp. 966–977.
- [83] Z Briqech, A R Sebak, and T A Denidni. "Wide-Scan MSC-AFTSA Array-Fed Grooved Spherical Lens Antenna for Millimeter-Wave MIMO Applications". In: *IEEE Transactions on Antennas and Propagation* 64 (2016), pp. 2971–2980.
- [84] B Rupakula et al. "63.5–65.5-GHz Transmit/Receive Phased-Array Communication Link With 0.5–2 Gb/s at 100–800 m and $\pm 50^\circ$ Scan Angles". In: *IEEE Transactions on Microwave Theory and Techniques* 66 (2018), pp. 4108–4120.
- [85] J S Herd and M D Conway. "The Evolution to Modern Phased Array Architectures". In: *Proceedings of the IEEE* 104 (2016), pp. 519–529.
- [86] Y P Zhang and D Liu. "Antenna-on-Chip and Antenna-in-Package Solutions to Highly Integrated Millimeter-Wave Devices for Wireless Communications". In: *IEEE Transactions on Antennas and Propagation* 57 (2009), pp. 2830–2841.
- [87] Yifa Li et al. "Experimental Validation and Applications of mm-Wave 8×8 Antenna-in-Package (AiP) Array Platform". In: *Electronics* 11 (2022), pp. 8239–8249.
- [88] H Gao et al. "Design and Experimental Validation of Automated Millimeter-Wave phased Array Antenna-in-Package (AiP) Experimental Platform". In: *IEEE Transactions on Instrumentation and Measurement* 70 (2021), pp. 1–11.
- [89] Fengchun Zhang et al. "Improved Over-the-Air Phased Array Calibration Based on Measured Complex Array Signals". In: *IEEE Antennas and Wireless Propagation Letters* 18 (2019), pp. 1174–1178.
- [90] Y Xing and T S Rappaport. "Propagation Measurements and Path Loss Models for sub-THz in Urban Microcells". In: *IEEE International Conference on Communications* (2021), pp. 1–6.
- [91] Ines Carton et al. "Validation of 5G METIS Map-based Channel Model at mmWave Bands in Indoor Scenarios". In: *European Conference on Antennas and Propagation (EuCAP)* (2016), pp. 1–5.
- [92] Jianhua Zhang et al. "Deterministic Ray Tracing: A Promising Approach to THz Channel Modeling in 6G Deployment Scenarios". In: *IEEE Communications Magazine* 62.2 (2024), pp. 48–54.
- [93] I F Akyildiz, J M Jornet, and C Han. "Terahertz Band: Next Frontier for Wireless Communications". In: *Physical Communication Journal* 12 (2014), pp. 16–32.
- [94] Z Yuan, J Zhang, and Y Ji et al. "Spatial Non-stationary Near-field Channel Modeling and Validation for Massive MIMO Systems". In: *IEEE Transactions on Antennas and Propagation* (2022).
- [95] A W Mbugua et al. "Millimeter Wave Multi-User Performance Evaluation Based on Measured Channels with Virtual Antenna Array Channel Sounder". In: *IEEE Access* 6 (2018), pp. 12318–12326.
- [96] Qi Li et al. "A Preliminary Indoor Assessment of a Sub-THz Channel Characterisations between 500 GHz and 750 GHz". In: *4th URSI Atlantic Radio Science Meeting (AT-RASC 2024)* (2024).